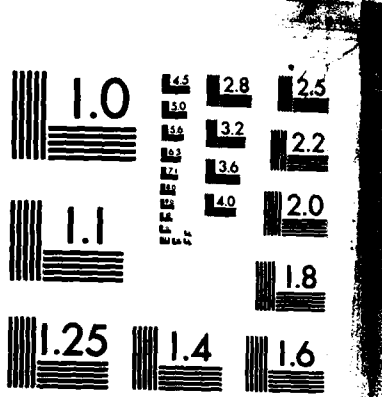


AD-A137 738 THE EFFECTS OF THERMAL/BLAST SYNERGISM ON THE NUCLEAR
VULNERABILITY OF A . (U) ARMY ARMAMENT RESEARCH AND
DEVELOPMENT CENTER ABERDEEN PROVING GROUND

UNCLASSIFIED R J PEARSON ET AL. JAN 84 ARBRL-TR-02540 F/G 15/6 NL





MICROCOPY RESOLUTION TEST CHART
NATIONAL BUREAU OF STANDARDS-1963-A

AD A137730

12
ADF 300379

TECHNICAL REPORT ARBRL-TR-02540

THE EFFECTS OF THERMAL/BLAST SYNERGISM ON
THE NUCLEAR VULNERABILITY OF A GENERIC
AIRCRAFT STRUCTURE

Richard J. Pearson
Henry L. Wisniewski
Paul D. Szabados
Arthur W. Wilson

January 1984



US ARMY ARMAMENT RESEARCH AND DEVELOPMENT CENTER
BALLISTIC RESEARCH LABORATORY
ABERDEEN PROVING GROUND, MARYLAND

Approved for public release; distribution unlimited.

DTIC FILE COPY

DTIC
ELECTED
FEB 6 1984
S D
D

84 02 06 004

**Destroy this report when it is no longer needed.
Do not return it to the originator.**

**Additional copies of this report may be obtained
from the National Technical Information Service,
U. S. Department of Commerce, Springfield, Virginia
22161.**

**The findings in this report are not to be construed as
an official Department of the Army position, unless
so designated by other authorized documents.**

*The use of trade names or manufacturers' names in this report
does not constitute endorsement of any commercial product.*

UNCLASSIFIED

SECURITY CLASSIFICATION OF THIS PAGE (When Data Entered)

REPORT DOCUMENTATION PAGE		READ INSTRUCTIONS BEFORE COMPLETING FORM
1. REPORT NUMBER TECHNICAL REPORT ARBRL-TR-02540	2. GOVT ACCESSION NO. <i>AD-A127 720</i>	3. RECIPIENT'S CATALOG NUMBER
4. TITLE (and Subtitle) THE EFFECTS OF THERMAL/BLAST SYNERGISM ON THE NUCLEAR VULNERABILITY OF A GENERIC AIRCRAFT STRUCTURE		5. TYPE OF REPORT & PERIOD COVERED Final
7. AUTHOR(s) Richard J. Pearson, Henry L. Wisniewski Paul D. Szabados and Arthur W. Wilson		6. PERFORMING ORG. REPORT NUMBER
9. PERFORMING ORGANIZATION NAME AND ADDRESS US Army Ballistic Research Laboratory, ARDC ATTN: DRSMC-BLT(A) Aberdeen Proving Ground, MD 21005		10. PROGRAM ELEMENT, PROJECT, TASK AREA & WORK UNIT NUMBERS DA Project 1L162618AH80 DA Project 1L162120AH25
11. CONTROLLING OFFICE NAME AND ADDRESS US Army AMCCOM, ARDC Ballistic Research Laboratory, ATTN: DRSMC-BLA-S(A) Aberdeen Proving Ground, MD 21005		12. REPORT DATE January 1984
14. MONITORING AGENCY NAME & ADDRESS (if different from Controlling Office)		13. NUMBER OF PAGES 126
		15. SECURITY CLASS. (of this report) UNCLASSIFIED
		15a. DECLASSIFICATION/DOWNGRADING SCHEDULE
16. DISTRIBUTION STATEMENT (of this Report) Approved for public release; distribution unlimited.		
17. DISTRIBUTION STATEMENT (of the abstract entered in Block 20, if different from Report)		
18. SUPPLEMENTARY NOTES		
19. KEY WORDS (Continue on reverse side if necessary and identify by block number) Nuclear Vulnerability Blast Waves Nuclear Thermal/Blast Simulation Thermal/Blast Synergism Air Shock Experiments Blast Loading Thermal Radiation Computer Simulation Thermal Loading Structural Response Thermal Simulation		
20. ABSTRACT (Continue on reverse side if necessary and identify by block number) This report details an experimental program developed to demonstrate that the combined effect of nuclear thermal/blast loading is significantly greater than either of these types of loading acting alone. The report covers the experiments and the preliminary computer simulation used in the design of the experiments.		

(over)

UNCLASSIFIED

SECURITY CLASSIFICATION OF THIS PAGE(When Data Entered)

The experimental program was designed to study the effects of thermal/blast loading on a generic aircraft structure. The structure used was a hollow, circular cylinder with clamped ends representing a bay in a missile body.

The experiments were conducted in the BRL Thermal/Blast Simulator. The nuclear loading simulation produced in this facility consists of a thermal radiation pulse from a controlled aluminum/oxygen burn followed by a shock wave from the shock tube.

During the program instrumented target cylinders were exposed to three types of loading: blast loading, thermal loading and combined thermal/blast loading. By comparing the results of the three types of experiments it was demonstrated that the structural response to the combined loading was different in both magnitude and character from the response to either blast or thermal loading.

UNCLASSIFIED

SECURITY CLASSIFICATION OF THIS PAGE(When Data Entered)

TABLE OF CONTENTS

	Page
LIST OF ILLUSTRATIONS	5
I. INTRODUCTION	9
II. THE EXPERIMENT	9
A. The Structural Targets	9
B. Instrumentation	10
C. The BRL Thermal/Blast Simulator	17
III. THE RESULTS	21
A. Blast Loading Structural Tests	21
B. Thermal Loading Structural Tests	34
C. Thermal/Blast Loading Structural Tests	45
IV. ANALYSIS	74
V. CONCLUSIONS AND RECOMMENDATIONS	84
ACKNOWLEDGEMENTS	86
REFERENCES	87
APPENDICES	89
A. Computer Modeling of Target Response Using PETROS 3.5	89
B. Design of the Test Apparatus	109
DISTRIBUTION LIST	119

Accession For	
NTIS GRA&I <input checked="" type="checkbox"/>	
DTIC TAB <input type="checkbox"/>	
Unannounced <input type="checkbox"/>	
Justification	
By _____	
Distribution/	
Availability Codes	
Dist	Avail and/or Special
A / I	



LIST OF ILLUSTRATIONS

Figure		Page
1.	Instrumentation Schematic	11
2.	Target Cylinder and Instrumentation Installed in the BRL Thermal/Blast Simulator	12
3.	Protective Cap for Pressure Gages in a Thermal/Blast Environment	14
4.	The BRL Thermal/Blast Simulator	18
5.	Flow Chart for Simulator Control Sequence	20
6.	Stagnation Overpressure History in Shot 8-80-7	23
7.	Diffraction Overpressure Histories at 0°, 15°, and 30° in Shot 8-80-7	24
8.	Diffraction Overpressure Histories at 45°, 60° and 75° in Shot 8-80-7	25
9.	Diffraction Overpressure Histories at 90°, 105° and 120° in Shot 8-80-7	26
10.	Diffraction Overpressure Histories at 135°, 150° and 165° in Shot 8-80-7	27
11.	Diffraction Overpressure History at 180° in Shot 8-80-7	28
12.	Blast Wave Diffraction Over a Cylinder	29
13.	Three-Dimensional Plots of Target Deformation in Shot 8-80-7	32
14.	Deformation of Center Cross Section of the Target in Shot 8-80-7	33
15.	Longitudinal and Circumferential Strain Histories at 0° and the Longitudinal Center	35
16.	Longitudinal and Circumferential Strain Histories at 0° and 19.69 cm below the Longitudinal Center	36
17.	Longitudinal Strain History at 0° and 37.47 cm above the Longitudinal Center and Circumferential Strain History at 315° and the Longitudinal Center	37

LIST OF ILLUSTRATIONS (CONTINUED)

Figure	Page
18. Longitudinal and Circumferential Strain Histories at 270° and the Longitudinal Center	38
19. Longitudinal Strain History at 270° and 37.47 cm above the Longitudinal Center and Circumferential Strain History at 135° and the Longitudinal Center	39
20. Flux and Fluence Histories in Shot 8-80-10	40
21. Temperature Histories at 0° and the Longitudinal Center and at 0° and 37.47 cm below the Center	41
22. Temperature Histories at 345° and the Longitudinal Center and at 45° and the Longitudinal Center	42
23. Temperature Histories at 315° and 19.69 cm below the Longitudinal Center and at 60° and the Longitudinal Center.	43
24. Temperature History at 90° and the Longitudinal Center	44
25. Three-Dimensional Plots of Target Deformation in Shot 8-80-10	46
26. Deformation of the Central Cross Section of the Target in Shot 8-80-10	47
27. Deformation of the Cross Section 33 cm above the Target Center in Shot 8-80-10	48
28. Longitudinal and Circumferential Strain Histories at 0° and the Longitudinal Center	49
29. Longitudinal and Circumferential Strain Histories at 0° and 19.69 cm below the Longitudinal Center	50
30. Longitudinal Strain Histories at 0° and 37.47 cm below the Longitudinal Center and at 315° and 19.69 cm above the Longitudinal Center.	51
31. Circumferential Strain History at 315° and 19.69 cm above the Longitudinal Center and Longitudinal Strain History at 270° and the Longitudinal Center	52

LIST OF ILLUSTRATIONS (CONTINUED)

Figure		Page
32.	Circumferential Strain History at 270° and the Longitudinal Center and Longitudinal Strain History at 90° and 37.47 cm below the Longitudinal Center	53
33.	Circumferential Strain History at 225° and the Longitudinal Center	54
34.	Flux and Fluence Histories in Shot 8-81-1	56
35.	Temperature History at 0° and 37.47 cm below the Center	57
36.	Temperature Histories at 45° and the Center and at 315° and 19.69 cm below the Center	58
37.	Temperature Histories at 90° and the Center and at 225° and the Center	59
38.	Stagnation Overpressure History in Shot 8-81-1	60
39.	Diffraction Overpressure History at 0°, 15°, and 30° in Shot 8-81-1	62
40.	Diffraction Overpressure Histories at 45° and 60° in Shot 8-81-1	63
41.	Diffraction Overpressure Histories at 90°, 105° and 120° in Shot 8-81-1	64
42.	Diffraction Overpressure Histories at 135° and 165° in Shot 8-81-1	65
43.	Diffraction Overpressure History at 180° in Shot 8-81-1	66
44.	Three-Dimensional Plots of Target Deformation in Shot 8-81-1	67
45.	Deformation of the Center Cross Section of the Target in Shot 8-81-1	68
46.	Five-Second Longitudinal and Circumferential Strain Histories at 0° and the Longitudinal Center	69
47.	Five-Second Longitudinal and Circumferential Strain Histories at 0° and 19.69 cm below the Longitudinal Center	70
48.	Five-Second Circumferential Strain History at 315° and 19.69 cm above the Longitudinal Center and Longitudinal Strain History at 270° and the Longitudinal Center	71

LIST OF ILLUSTRATIONS (CONT)

Figure	Page
49. Five-Second Longitudinal Strain History at 90° and 37.47 cm below the Longitudinal Center	72
50. Five-Second Circumferential Strain History at 225° and the Longitudinal Center	73
51. Ten-Millisecond Longitudinal Strain Histories at 0° and the Longitudinal Center	75
52. Ten-Millisecond Longitudinal and Circumferential Strain Histories at 0° and 19.69 cm below the Longitudinal Center	76
53. Ten-Millisecond Circumferential Strain History at 315° and 19.69 cm above the Longitudinal Center and Longitudinal Strain History at 270° and the Longitudinal Center	77
54. Ten-Millisecond Longitudinal Strain History at 90° and 37.47 cm below the Longitudinal Center	78
55. Ten-Millisecond Circumferential Strain History at 225° and the Longitudinal Center	79
56. Experimentally Measured and Calculated Overpressure Loading . .	85

I. INTRODUCTION

When a nuclear weapon is detonated in the atmosphere most of the energy released is partitioned between a blast wave and a thermal radiation pulse. Targets damaged by nuclear weapons are loaded first by the thermal pulse and then by the blast wave. The relative importance of the two types of loading is determined by the weapon's yield, height of burst, target range, atmospheric transmittance and structural characteristics of the target. Very often one or the other of the two types of loading can be identified as the predominant damage producing mechanism. There is evidence, however, of some scenarios in which thermal loading of the target significantly enhances the damage produced by the blast wave which follows. In order to accurately assess the vulnerability of some targets the effect of this synergism between nuclear thermal and blast loading must be taken into account.

The development within the past few years of large-scale chemical thermal simulators has made it possible to simulate combined nuclear thermal/blast loading. The objective of this project was to use this new thermal simulation technology to experimentally confirm the existence of synergism between nuclear thermal and blast loading. An additional objective was to provide an experiment for which it would be possible to run matching structural code simulations. By comparing the results of the computer code and the experiment it will be possible to evaluate the codes ability to model structural response caused by thermal/blast loading.

A relatively fast and moderately complex structural response code, PETROS,¹ was used to design the experiment. Simplified models of the thermal and blast loading histories and candidate target designs were input into PETROS. The loading and target design parameters were varied until a design comparable with the BRL simulation and fabrication facilities was arrived at. The pre-test PETROS calculations are covered in Appendix A and the final target and target mount design is covered in Appendix B.

To simplify the analysis of the experiment, three different types of tests were conducted. First, tests with blast loading only were conducted, then tests with thermal loading only and, finally, combined thermal/blast tests. By comparing the results of these three types of experiments, the relative importance of each type of loading was evaluated.

II. THE EXPERIMENT

A. The Structural Targets

The structural targets used in the tests were hollow cylinders formed

¹S. D. Pirotin, B. A. Berg, and E. A. Witmer, "PETROS 3.5: New Developments and Program Manual for the Finite-Difference Calculation of Large Elastic-Plastic Transient Deformations of Multilayer Variable-Thickness Shells," U.S. Army Ballistic Research Laboratories Contract Report No. 211, Feb. 1975 (AD A007215).

from 6061-T6 aluminum. The target cylinders were intended to be representative of a class of thin wall, metallic structures found in aircraft and Command, Control and Communication (C³) equipment which are thought to be susceptible to synergistic thermal/blast loading. The target cylinders might be considered a highly simplified representation of a generic missile body bay.

The target cylinders used had an outside diameter of 30.683 cm (12.06") and a wall thickness 1.016 mm (0.04"). Both ends of the target cylinders were clamped to a heavy target mount to approximate fixed end conditions. The distance between the clamped ends was 80.000 cm. The total length of the target was 86.500 cm. The details of the design are given in Appendices A and B.

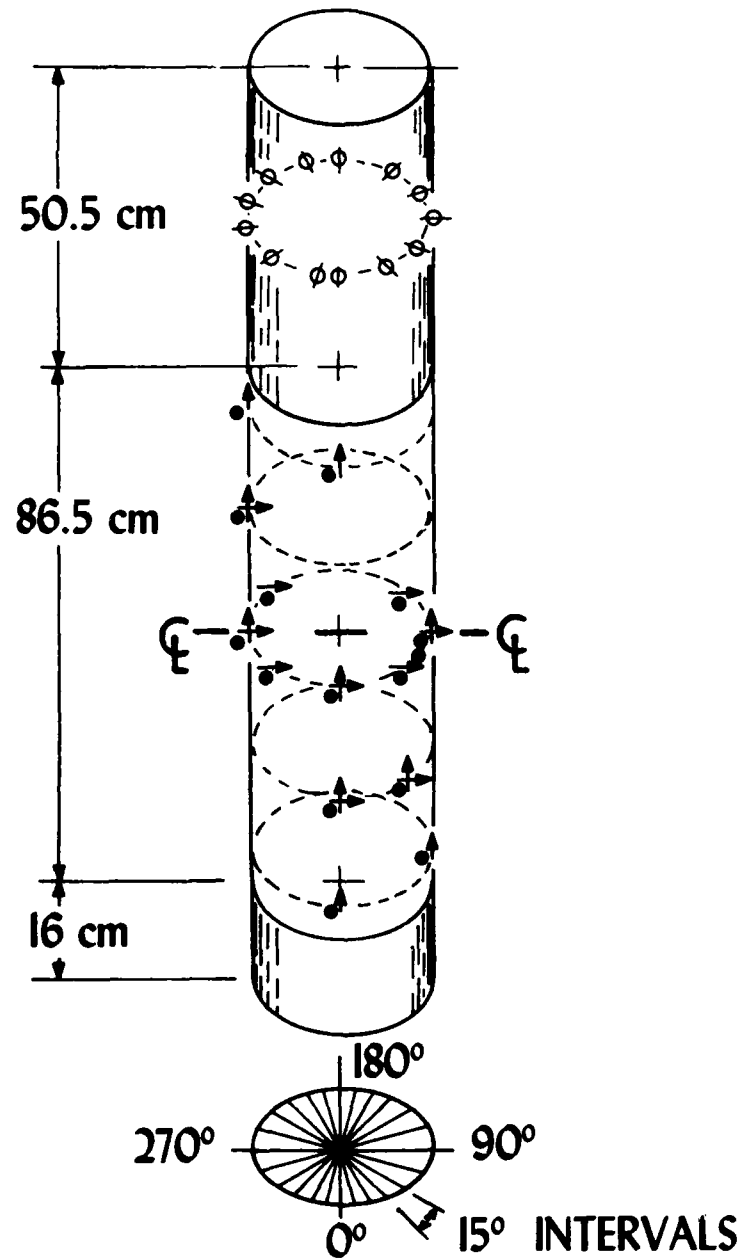
One final feature of the target important to the thermal loading portion of the test was the absorptivity of the target's surface coating. A spectrally flat, high-temperature paint with an absorptivity of 0.92 was used. The paint, Medtherm High Temperature, Optical Black Coating, Type #20164, was the same paint used on the sensitive areas of the flux gages.

B. Instrumentation

Five different types of measurements were made during the test in the BRL simulator. In addition, the tests were photographed with high-speed motion picture cameras to provide a visual check on the functioning of the simulator and a qualitative check on target response. Four of the measurements were made electronically, recorded on analog tape and later digitized for computer based data reduction. Electronic measurements were made of pressure, radiant thermal flux, temperature in the target and strain in the target. Figure 1 shows a comprehensive schematic of all instrumentation location on the several targets used in the program; due to limitation on recording equipment no one target carried all of the instrumentation shown. A photograph of the target cylinder, target mount and instrumentation is shown in Figure 2.

Pressure measurements were made to determine both the blast loading on the target and the incident blast wave values. The pressure history behind the incident blast wave was measured by a pair of Bytrex HFG-15 gages. One gage, mounted through the shock tube wall, was used to measure the incident static overpressure. The other gage was mounted in a probe and used to measure stagnation overpressure. The probe can be seen in the lower right-hand corner of Figure 2. The Bytrex gages had a response time of 0.125 ms and a settling time of 0.3 ms. Both gages were shock mounted and equipped with protective dust caps. The protective caps were designed by BRL to shield the gages from dust and thermal effects while maintaining the response characteristics.

Blast loading on the target cylinder was estimated from the pressure history on the upper bearing mount. The bearing mounts have the same outer diameter as the target cylinder and should have the same loading history. Mounting the gages directly through the wall of the target cylinder would have greatly complicated the structural analysis and was not considered practical.



→ STRAIN GAGE
 φ PRESSURE GAGE
 • THERMOCOUPLE

Figure 1. Instrumentation Schematic.



Figure 2. Target Cylinder and Instrumentation Installed in the BRL Thermal/Blast Simulator.

The locations of the 13 pressure gages on the upper bearing mount are shown in open circles in Figure 1. The gages and their white teflon shock mount can be seen in Figure 2.

The gages used to measure blast loading were Endevco 8510-15's and 8510-5's. The gages were mounted in two different ways. In the blast only tests the gages were deployed in a teflon shock mount and use only the manufacturer's dust cap for protection. In this configuration the response time of the gages was 0.02 ms.

In the second thermal/blast test a second dust cap was added to the gage mount. The results of the first thermal/blast showed that gages on the bearing mount exhibited a large amount of baseline drift between the thermal pulse and shock wave arrival. The baseline drift was characteristic of the effect of high temperature on the gage's sensitive element. A new protective cap similar to the ones used on the Bytrex gages was designed for the Endevco gages. Figure 3 shows the final design. Tests in BRL's 10 by 38 cm shock tube showed that the cavity response of the new cap lowered the performance of the mounted gage. The settling time for oscillations caused by the cavity response was 0.2 ms. The new cap did, however, provide the required protection for the gages. There was little or no baseline drift on any of the Endevco gages during the second thermal/blast test.

A final Endevco 8510-5 gage was mounted inside the target cylinder to monitor internal pressure changes.

Measurements of the output of the thermal source in the thermal/blast simulator were made using a heat flux transducer mounted in the rear of the probe containing the stagnation pressure gage. The transducer used was a Medtherm model 64-100-14 heat flux transducer. The response time of the transducer was 15 ms.

A series of calibration tests was carried out on the thermal source of the thermal/blast simulator. The calibration tests were used to determine the timing sequence needed to obtain the desired flux from the source and to map the flux values in the circular cross section of the simulator at the test station used in the structural tests. In order to obtain the proper flux value on the target during the structural test a scaling factor was developed which related the flux at the center of the test station to the flux at the probe location. In presenting the flux on the target, the flux values recorded at the probe location during the structural test were scaled up to the values at the center of the target.

The strain on the inner surface of the target was measured using foil strain gages. The strains were measured in both the longitudinal and circumferential directions on the target cylinders. The locations of the strain gages are shown in Figure 1 as arrows. The direction of the arrow indicates whether the strain was measured in the longitudinal or circumferential direction. A double arrow indicates that strain was measured in both directions.

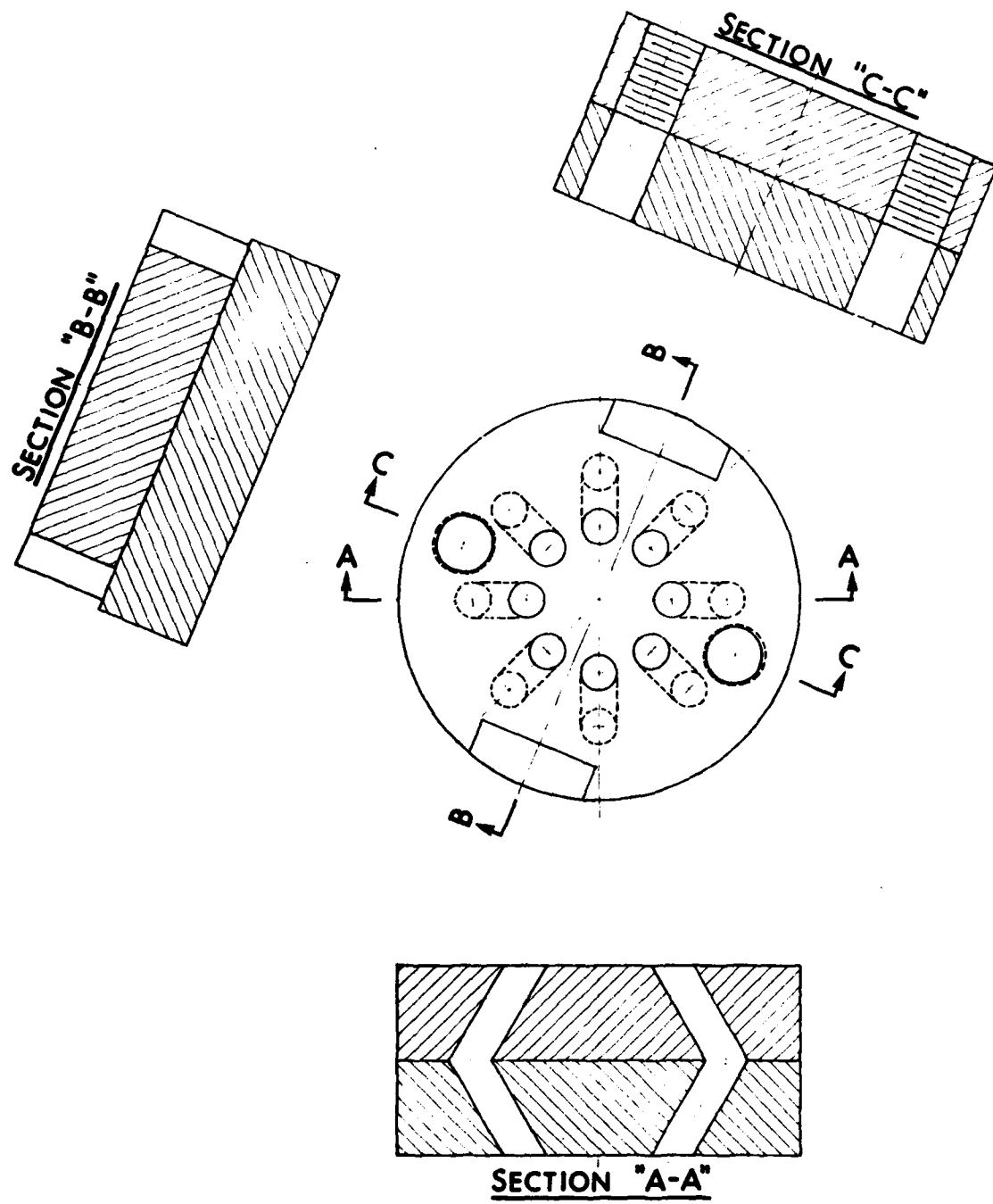


Figure 3. Protective Cap for Pressure Gages in a Thermal/Blast Environment.

The strain gages used to instrument the target were Micro-Measurements WK-13-125TM-350 and WK-13-125AD-350. The TM designation denotes a configuration with a 2-element, 90° "tee" rosette used to measure strain in both the longitudinal and circumferential directions. The AD designation denotes a configuration with a single element gage to measure strain in only one direction.

In the test involving blast loading only, the room temperature curing epoxy M-Bond 200 was used to attach the gages.

In the test involving thermal loading a high-temperature epoxy had to be used. The adhesive used was M-Bond 600 which was cured at 110°C for at least four hours. Higher temperatures would have been desirable but were not used because of the danger of thermal degradation of the targets' material properties before the test. The adhesive was cured by heating the whole target cylinder in a large environmental chamber and applying pressure through the use of specially designed dead weights.

The gages used were designed to be self-temperature-compensating; i. e., they were designed to have the same coefficient of thermal expansion as the material whose strain was to be measured. There were no gages available which matched 6061-T6 Aluminum used in the experiments. In addition, the temperatures reached in the target were beyond the range for which the manufacturer could supply data on thermal effects. In selecting the gages trade-offs had to be made in the areas of max. strain, max. operating temp. and sensitivity. As a result of these necessary compromises special provisions had to be made to compensate for thermal effects of the strain gages.

Tests were conducted in which samples, instrumented with strain gages and a thermocouple in the same way as the target cylinder, were heated in a furnace to the maximum temperature encountered in the structural tests. The "apparent thermal strains" induced in the unloaded samples were recorded at a number of different temperatures. Using a least squares fitting technique a polynomial function relating the "apparent thermal strain" (ϵ_T) record by the strain gages to the temperature record by the thermocouple (T) was developed. The polynomial developed was the following

$$\epsilon_T = -0.113 \times 10^{-1} + (0.479 \times 10^{-3})T - (0.182 \times 10^{-5})T^2 + (0.150 \times 10^{-8})T^3 \quad (1)$$

In Equation 1, ϵ_T is given in percent strain and T is given in degree centigrade. In the computer based data reduction of the recorded strain histories a thermally corrected strain history was calculated. The corrected strain histories were calculated by subtracting the calculated "apparent thermal strain" from the recorded strain. The temperatures used in the calculation were obtained in one of two ways. When the targets were instrumented a thermocouple was located near every strain gage location. For most strain gages the temperature-history recorded by these nearby gages was used as the temperature in the calculation of the "apparent thermal strain." In a few cases the nearest thermocouple was lost during the structural test; in these cases the temperature history was estimated from the flux history using the technique described in Appendix B.

The temperature on the inner surface of the target cylinder was recorded by K-type thermocouple junctions. The junctions were bonded to the surface with epoxy adhesives. Bonded thermocouples were used because it proved impractical to form reliable welds between the thermocouple alloys and the Aluminum 6061-T6 of the target. The locations of the thermocouples are shown as solid circles in Figure 1.

Two different types of bonded thermocouple installations were used during the structural tests. The first type of installation was developed from material on hand for the first tests. The installation was formed by spotwelding the two 0.254 mm thermocouple wires to a square of 0.127 mm thick brass foil to form an intrinsic junction. The foil with the junction was bonded to the target with M-Bond 600 adhesive.

The second type of installation used a commercial bondable thermocouple gage. The gages used were Omega Engineering, Style I, "cement-on" thermocouples. The commercial gages were bonded using Omegabond 200, a highly thermally conductive epoxy. Omegabond is a heat curing epoxy adhesive. In this program it was cured at 110 C for 8 hours. As with the strain gage epoxy, higher curing temperatures were recommended by the manufacturer but could not be used because they would have degraded material properties of the target. The time constant of the gage given by the manufacturer was 20 ms.

During the thermal source calibration tests a sample of the target material instrumented with three K-type thermocouples was exposed. One junction was formed by spotwelding the two thermocouple wires directly to the target to form an intrinsic junction. The other two were bonded to the target using the techniques applied in the structural test. Both bonded junctions proved slower than the spotwelded junction, but their readings were only 5% lower at the end of the thermal source burn. During the burn the brass foil installation's reading was never more than 10% below the reading of the commercial gage.

In addition to the electronically recorded measurements made during the structural test, manual measurements of the target shape were also made. The measurements were made both before and after the structural test. The measurements were performed using a machinist dial gage. The dial gage rode on an optical rail which was in turn mounted rigidly to a heavy aluminum beam. The beam was bolted to the floor and ceiling of the simulator. Alignment pins were used to insure that the beam was properly positioned.

The beam had to be removed to allow target installation and during the actual structural test. At the start of each set of measurements readings were taken on index marks on the target mount to determine if the beam was properly aligned. Once the beam was properly aligned, the gage was positioned along the length of the target using the marking on the optical rail. A series of horizontal cross sections on the target was determined by revolving the target beneath the head of the dial gage. The angular position on the target was determined by reference to indexing marks machined into the reinforcing rings on the target mount bulkheads.

During the blast only tests eleven target cross sections were measured. A

cross section was taken of the center line of target and every 7.94 cm on either side of the center line. During the final thermal and thermal/blast structural tests cross sections were added at 35.72 and 35.72 cm to better define the maximum deflection caused by thermal loading. For the cross section within 31.75 cm of the center line measurements were taken every 10° around the circumference. For cross sections beyond 31.75 cm the measurements between 170° and 210° could not be taken because of interference between the target mount and the dial gage.

The accuracy of the measurements made with the dial gage was determined by errors in rail alignment and gage positioning on the target rather than the accuracy of the gage itself. The dial gage is capable of measuring to ± 0.0127 mm. Test of repeatability of the measurements showed that they were accurate to ± 0.254 mm.

It should be noted that these measurements refer to a Eulerian reference frame fixed in space. The measurements give the radial distance of the outer surface of the target from the rotation axis for a given angle and given longitudinal distance. The pre-test and post-test measurements do not necessarily refer to the same element of target material.

As an adjunct to the measurement on the target and as a check on the functioning of the thermal source high-speed cameras were used to record the thermal portion of the structural test. The films were used to get qualitative pictures of target deformation during thermal loading. In addition, the films provided a check against gross experimental errors, such as thermal source timer malfunction, or burning and bubbling of the thermal coating or contamination of the target or flux meter by pieces of the thermal source's plastic diaphragm. These errors are difficult to diagnose from the electronic test data alone, but can be easily detected on film.

C. The BRL Thermal/Blast Simulator

The BRL thermal/blast simulator consists of a shock tube with a chemical thermal source mounted in its expansion section. The simulator is shown schematically in Figure 4.

The shock tube used in the simulator was a cold gas driven tube with a constant circular cross section 2.44 m in diameter. The compression section was 83.08 m long and the expansion section was 70.77 m long. The diaphragm between the two sections was formed from 1.56 mm steel sheet and opened by a radial pattern of line charges.

The center of the target rotator drive shaft was located 22.86 m from the open end of the shock tube.

The thermal source consists of a pair of plastic diaphragms which section off of the simulator² and a set of 12 nozzles, each with its own fluidizer and pyrotechnic igniter. The upstream diaphragm was located 1.52 m downstream

²G. D. Teel and F. H. Oertel, "Testing to Combined Blast and Thermal Effects at the BRL," Proceedings of the 7th International Symposium on Military Applications of Blast Simulation, Medicine Hat, Alberta, Canada, 13-17 July 1981.

BRL THERMAL/BLAST SIMULATOR

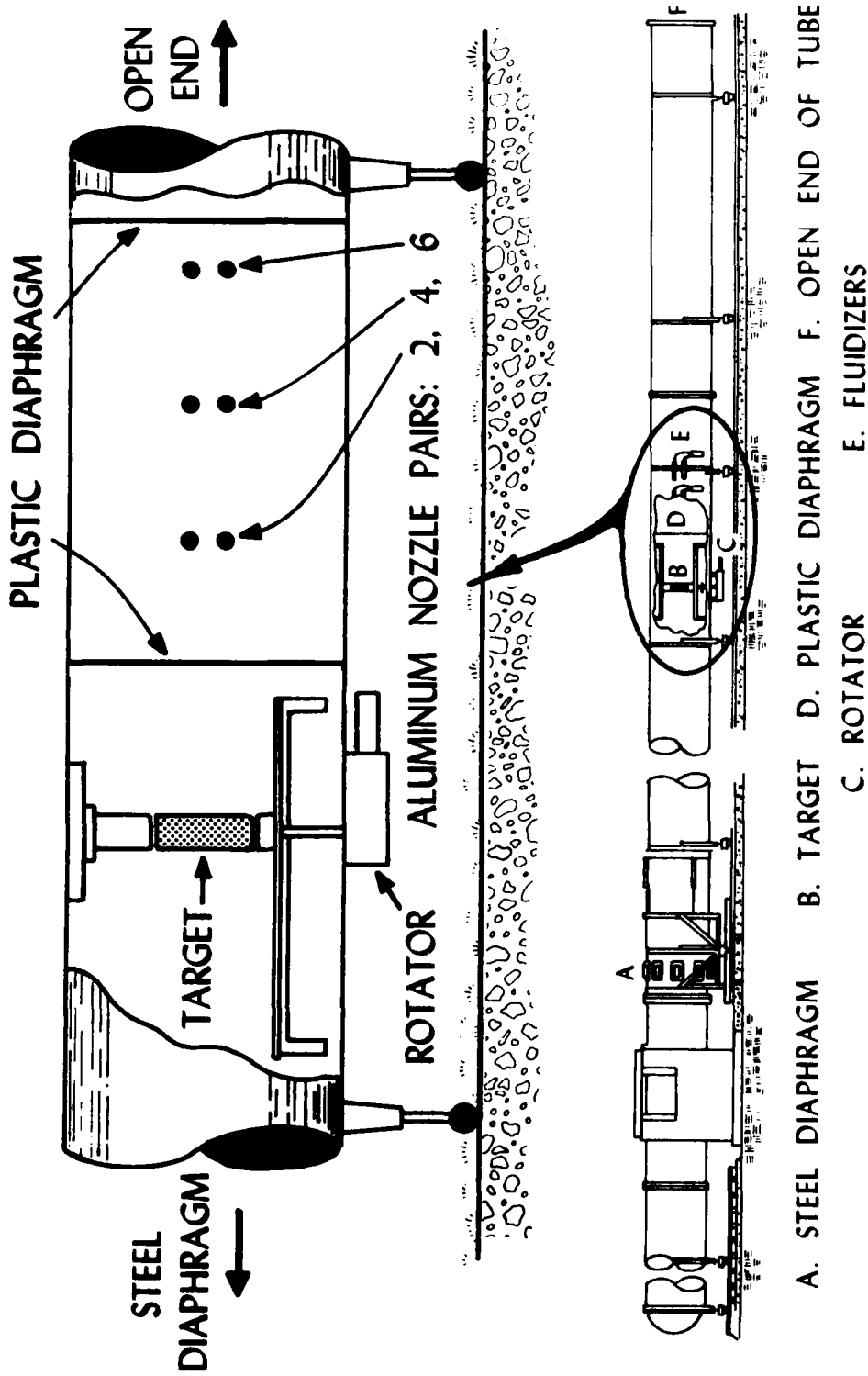


Figure 4. The BRL Thermal/Blast Simulator.

from the rotator axis and the downstream diaphragm was located 4.27 m downstream. The nozzles and their associated fluidizer and pyrotechnic igniters were mounted in pairs one above the other on either side of the vertical center line of the simulator. The pair closest to the rotator was 1.98 m downstream. The nozzle pairs were spaced every 0.48 m along the simulator on alternating sides of the axis of the circular cross section.

A flow chart of the control sequence used in the final combined thermal/blast structural test is shown in Figure 5. The flow chart shows the sequence in which the electronic timer triggered the various simulator functions necessary to conduct the structural test. The flow chart also shows the two malfunction conditions which would cause the test to be aborted.

During the tests the timer first started the analog tape machine used to record the output of the electronic instrumentation. The timer then triggered the circuits that produced the calibration steps and time zero marks used in later data reduction. The timer started the high-speed cameras next.

The timer started the thermal source function by electrically initiating the pyrotechnic igniters. Each igniter had a burn through link built into it. When all the igniters functioned properly the links opened and the sequence continued. If any of the links failed to open before the first nozzle was actuated, the test was aborted.

When the nozzles were actuated, a solenoid valve was opened, allowing high-pressure nitrogen to enter the fluidizer. The high-pressure gas fluidized the aluminum dust in the fluidizers and forced it through the nozzle into the oxygen atmosphere contained between the two plastic diaphragms. As the aluminum dust entered the simulator, it passed through the flame of an igniter. The heated aluminum dust burned in the oxygen atmosphere, producing a cloud of aluminum oxide with a color temperature of approximately 3300 K^o. The cloud transferred heat to the front of the target, radially simulating nuclear thermal loading. The heat also melted the plastic diaphragms opening the shock tube.

Because the clouds of aluminum oxide were highly self-absorptive, the nozzle had to be sequenced with the nozzle pair furthest from the target burning first. The delay between nozzle actuation gave some control of the shape of the thermal pulse.

After the completion of the thermal source burn the timer actuated the target rotator. The rotator moved the heated face of the target through 180° to face upstream toward the shock tube diaphragm. A switch on the rotator was closed when the target was properly repositioned. If the switch failed to close before the time set for shock tube firing the test was again aborted.

When the shock tube was fired the line charge opened the steel diaphragm, allowing the high-pressure air in the compression chamber to escape. The high-pressure gas formed a shock which moved down the simulator and engulfed the target. The shock wave which engulfed the target provided the nuclear blast simulation. Several seconds after the shock wave reached the target, the

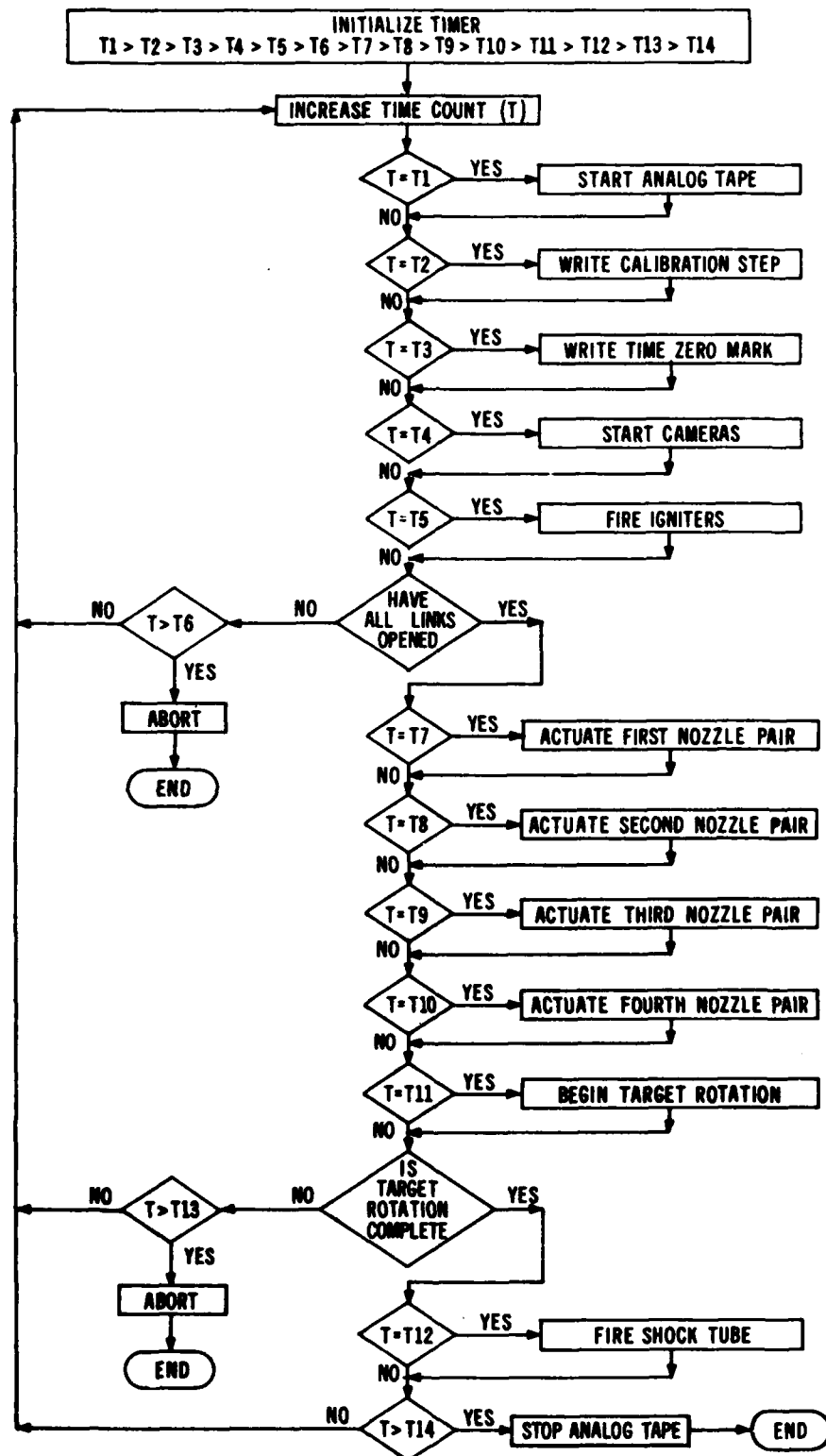


Figure 5. Flow Chart for Simulator Control Sequence.

timer shut down the tape machines, and the simulation was complete.

The complete simulator control sequence took less than 35 seconds. The time between the activation of the first nozzle and the completion of the blast loading was less than 5 seconds.

In tests involving only blast or thermal loading, only part of the control sequence was used. For tests with only thermal loading neither the rotator nor shock tube was actuated. For tests with only blast loading, the ignitors, the nozzles, and the rotator were not actuated.

III. THE RESULTS

A. Blast Loading Structural Tests

The first type of structural test conducted involved only blast loading of the target cylinders. Because thermal loading was absent the pressure gages used to measure target loading were installed with only the manufacturer's dust cap for protection. The absence of thermal loading also meant the room temperature curing epoxy could be used to install the strain gages on the target cylinder. Two structural tests involving blast loading only were conducted.

In the first test (Shot 8-80-6), the cylinder was loaded by a shock wave with an incident static overpressure of approximately 33 kPa and a stagnation overpressure of approximately 39 kPa. The target suffered only very small permanent deformation. The largest deformation measured was 0.381 mm, which is only slightly above the error in the measurement. The strain history showed a regular sinusoidal pattern that would be expected in elastic response. The incident overpressure level used in this test is probably very close to the threshold for permanent damage to the target cylinder.

The details of the test results from shot 8-80-6 will not be presented because a number of malfunctions during the tests makes their interpretation difficult. The most important malfunction was due to a failure of experimental design. The strain gage leads were too massive. The high acceleration of the deforming target wall caused the majority of the joints between the leads and the strain gages to fail. Substitution of lighter wire insulated with high-temperature lacquer for the heavier, polyethylene insulated wires used in this test reduced the problem on subsequent tests.

Two other malfunctions affected the blast loading of the target. The diaphragm used in the test failed to open properly, resulting in a shock that was not completely formed up when it reached the target. The pressure histories showed small "precursor" shock that preceded the main shock. The "precursor" probably did not significantly change the response but it did make interpretation more difficult. The final problem was leakage of the high-pressure gas into the target interior. The internal gage recorded a pressure increase which reduced the differential pressure across the target wall. The increase was less than 2.5 kPa during the structurally significant first 6.0 ms of the diffraction phase. The interior pressure did eventually reach 12 kPa after 150 ms. This

problem was also reduced on later tests by sealing around the bolts and shafts that penetrated the aluminum bulkheads at the ends of the target cylinder.

The second structural test involving blast loading only was shot 8-80-7. In shot 8-80-7 the target was loaded by a shock wave with incident static overpressure of 43.7 kPa and a stagnation overpressure of 54.4 kPa. A plot of the stagnation overpressure history in the test section is shown in Figure 6. The stagnation overpressure is given because it is more representative of the target loading.

The absolute pressure in the compression section of the simulator used to create the shock wave was 236.29 kPa. The absolute pressure in the expansion section was 101.84 kPa. The temperature in both sections of the simulator was 22.22 C°.

The pressure history shown in Figure 6 is typical of a cold gas driven shock tube. The history shows the initial sharp pressure increase at shock arrival. The rise time of the pressure across a fully formed shock is too fast to be measured by the gages used, but it is calculated to be of the order of a few nanoseconds. Following the shock front is a period of constant overpressure which lasts until the arrival of the first rarefaction wave from the opened end of the simulator. The pressure decrease through rarefaction waves is much slower than the increase through the shock, lasting over 100 ms. Following the first rarefaction there is another period of constant overpressure lasting until the arrival of the contact surface. The denser gas behind the contact surface causes the slow increase in the stagnation overpressure. The arrival of the second rarefaction wave from the closed end of the compression section causes the overpressure to become negative, dropping below ambient pressure. A compression wave from the open end of the expansion section increases the pressure back to ambient and ends the loading cycle.

The fundamental frequency of the targets response is in the range of 10^2 to 10^3 Hz³. Most of the significant target response will probably occur within the first few cycles. Therefore, it is necessary to look in detail at only the first few milliseconds after shock arrival, although the whole blast loading cycle lasted approximately a second. Figures 7 through 11 show the first 10 ms of the loading record by the gages on the upper bearing mount. The time in Figures 7 through 10 begins 0.02 ms before shock arrival at the 0° station. The distance between origin and the beginning of the loading history is representative of the transit time of the shock from the 0° station to the station plotted.

The blast loading histories can be more easily interpreted by reference to Figure 12. Figure 12 shows a series of isobars plots and matching shadowgraphs taken at different times in the blast loading history. The plots are from a matching calculation performed by Dr. A. Mark⁴ and are similar to the

³

F. H. Gregory, private communication, Ballistic Research Laboratory, Jan. 82.

⁴ A. Mark, "Shock Diffraction Computations Over Complex Structures," Technical Report ARBRL-TR-02455, US ARRADCOM, Ballistic Research Laboratory, Aberdeen Proving Ground, MD, Dec. 1982 (AD B070013L).

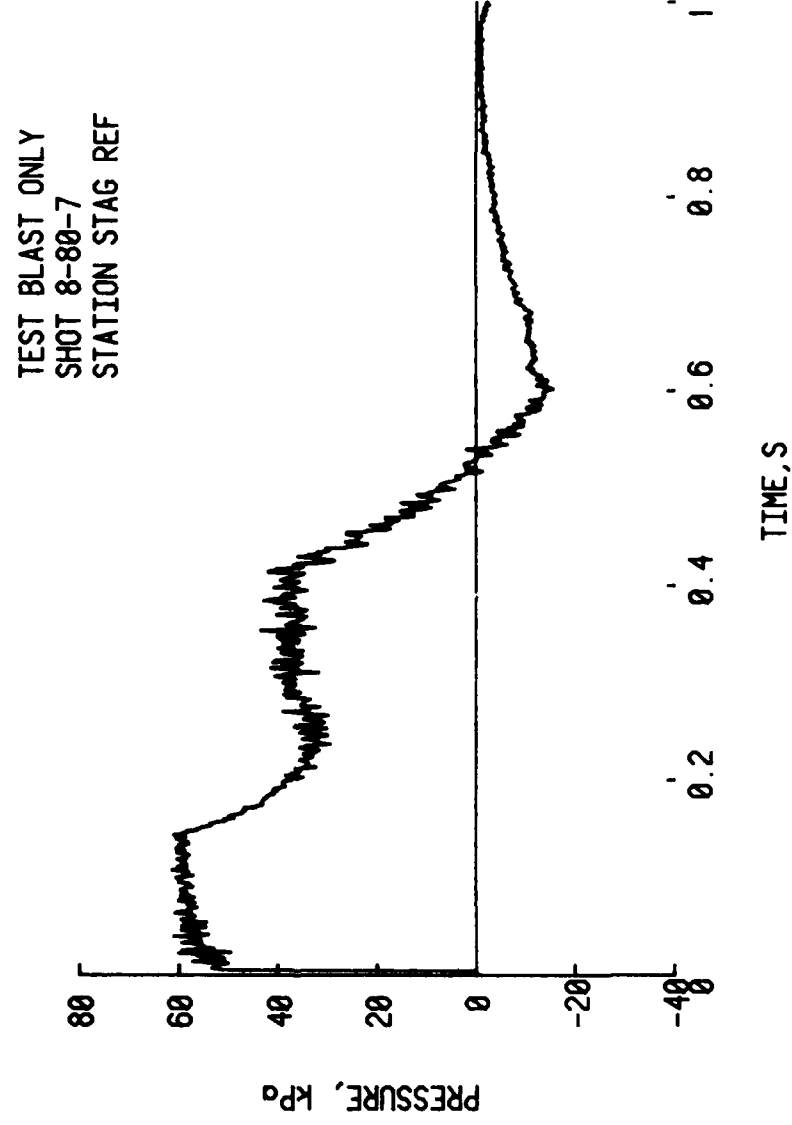


Figure 6. Stagnation Overpressure History in Shot 8-80-7.

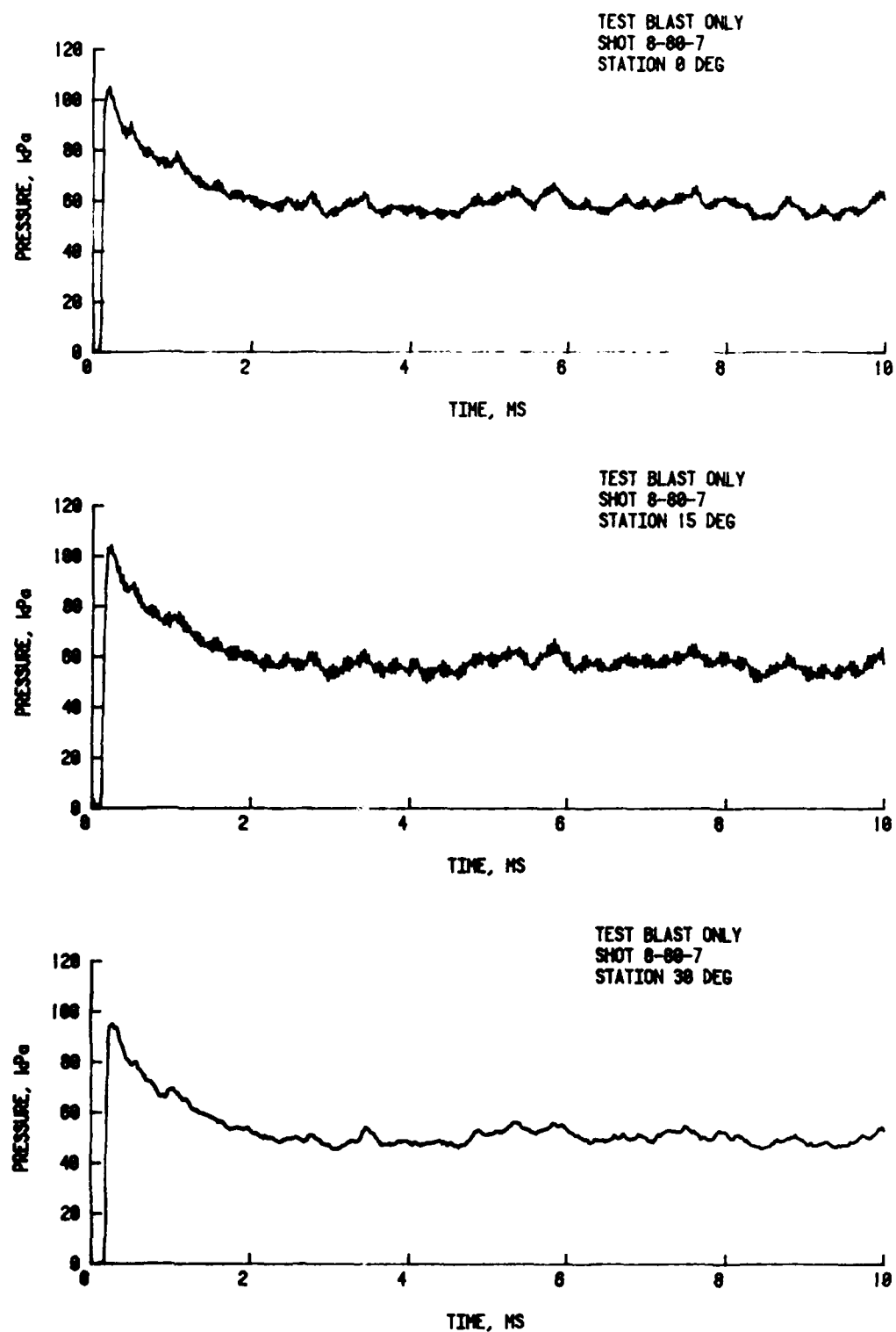


Figure 7. Diffraction Overpressure Histories at 0° , 15° , and 30° in Shot 8-80-7.

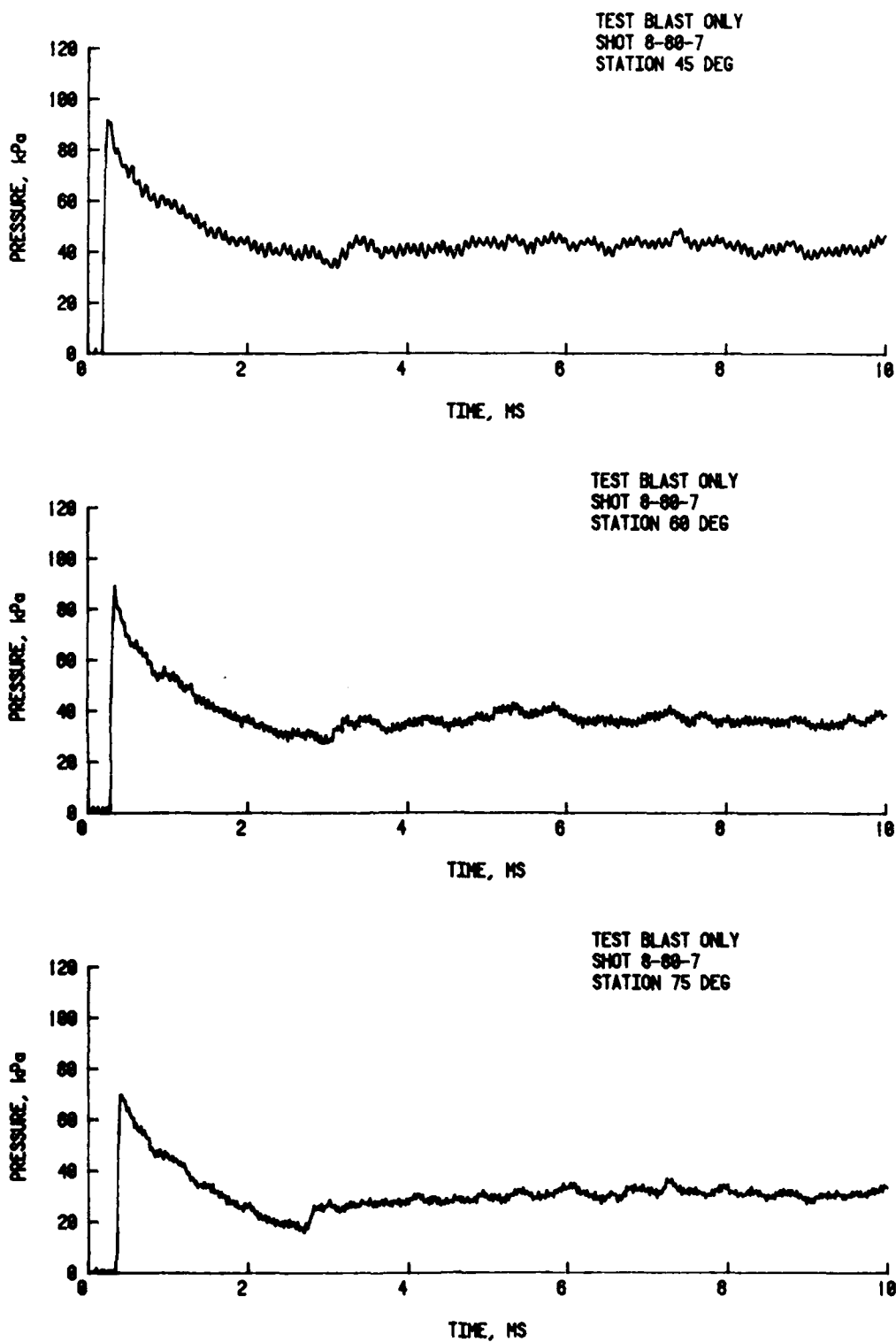


Figure 8. Diffraction Overpressure Histories at 45° , 60° and 75° in Shot 8-80-7.

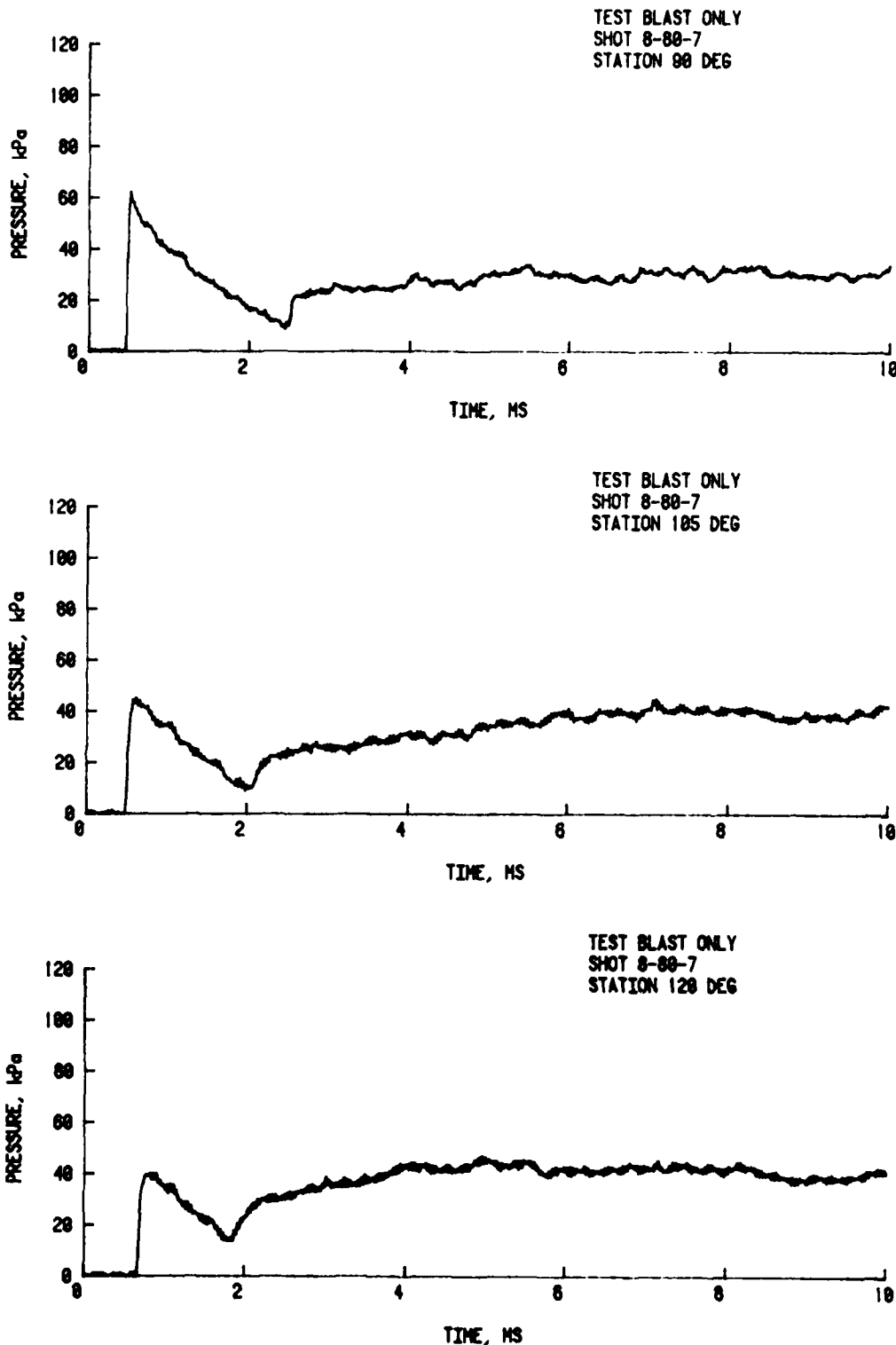


Figure 9. Diffraction Overpressure Histories at 90° , 105° and 120° in Shot 8-80-7.

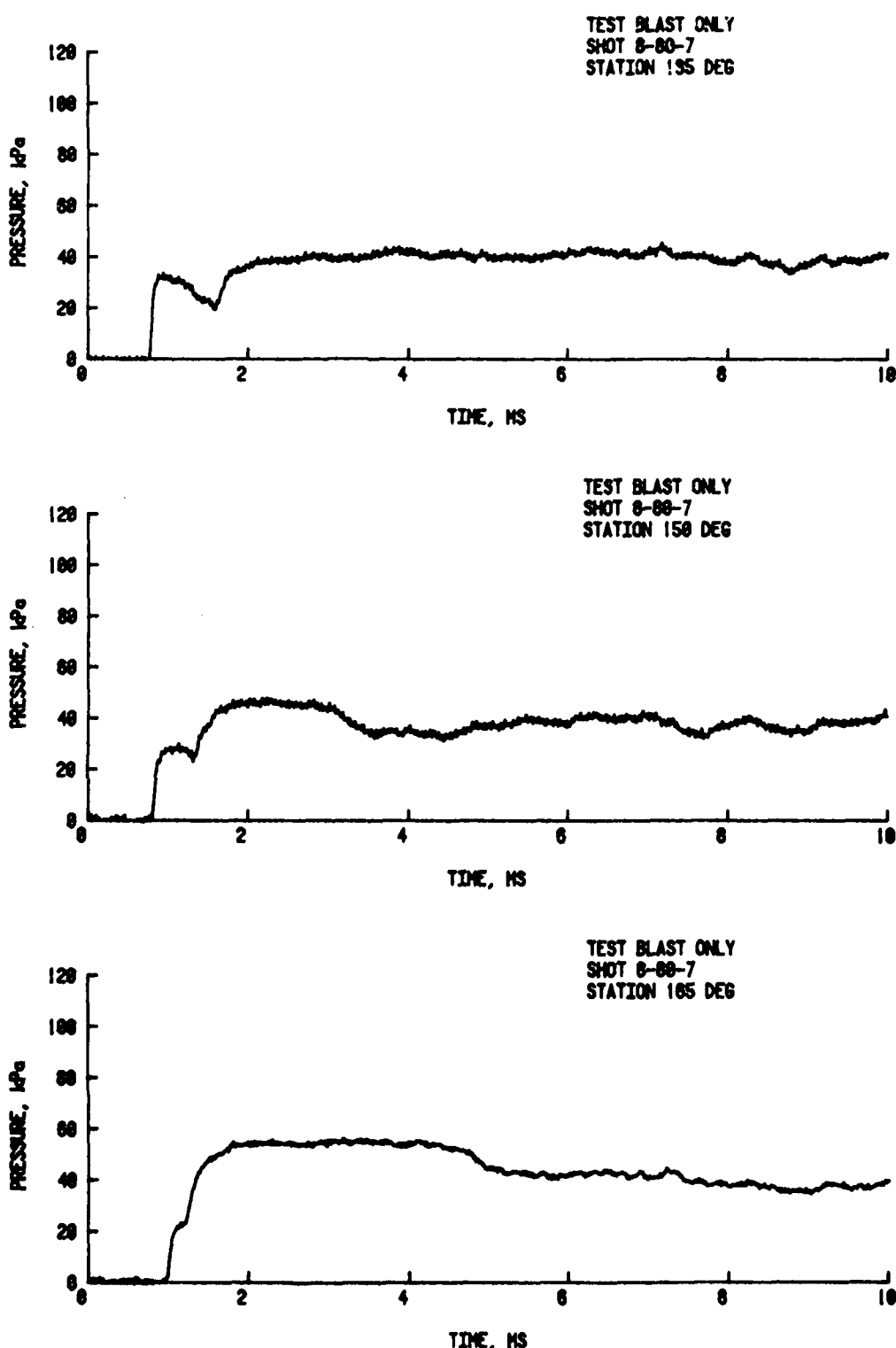


Figure 10. Diffraction Overpressure Histories at 135° , 150° and 165° in Shot 8-80-7.

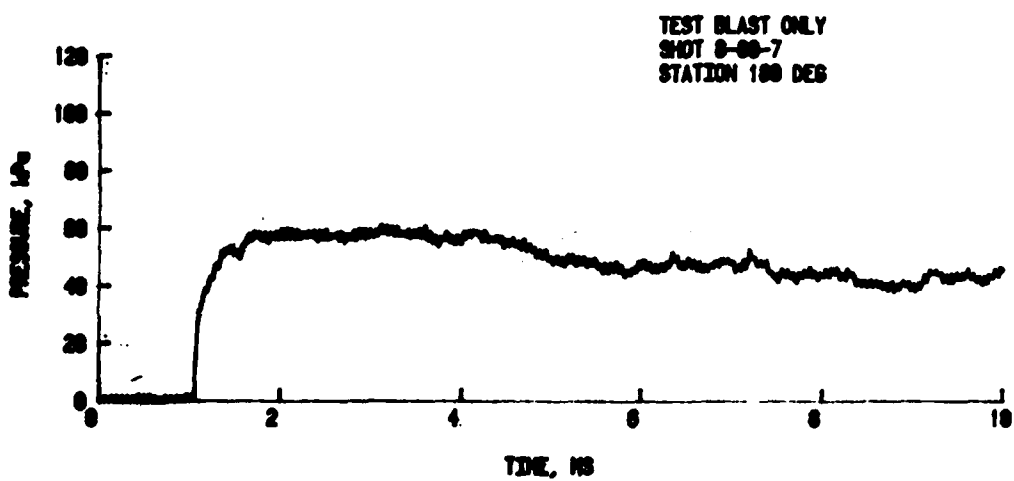


Figure 11. Diffraction Overpressure History at 180° in Shot 8-80-7.

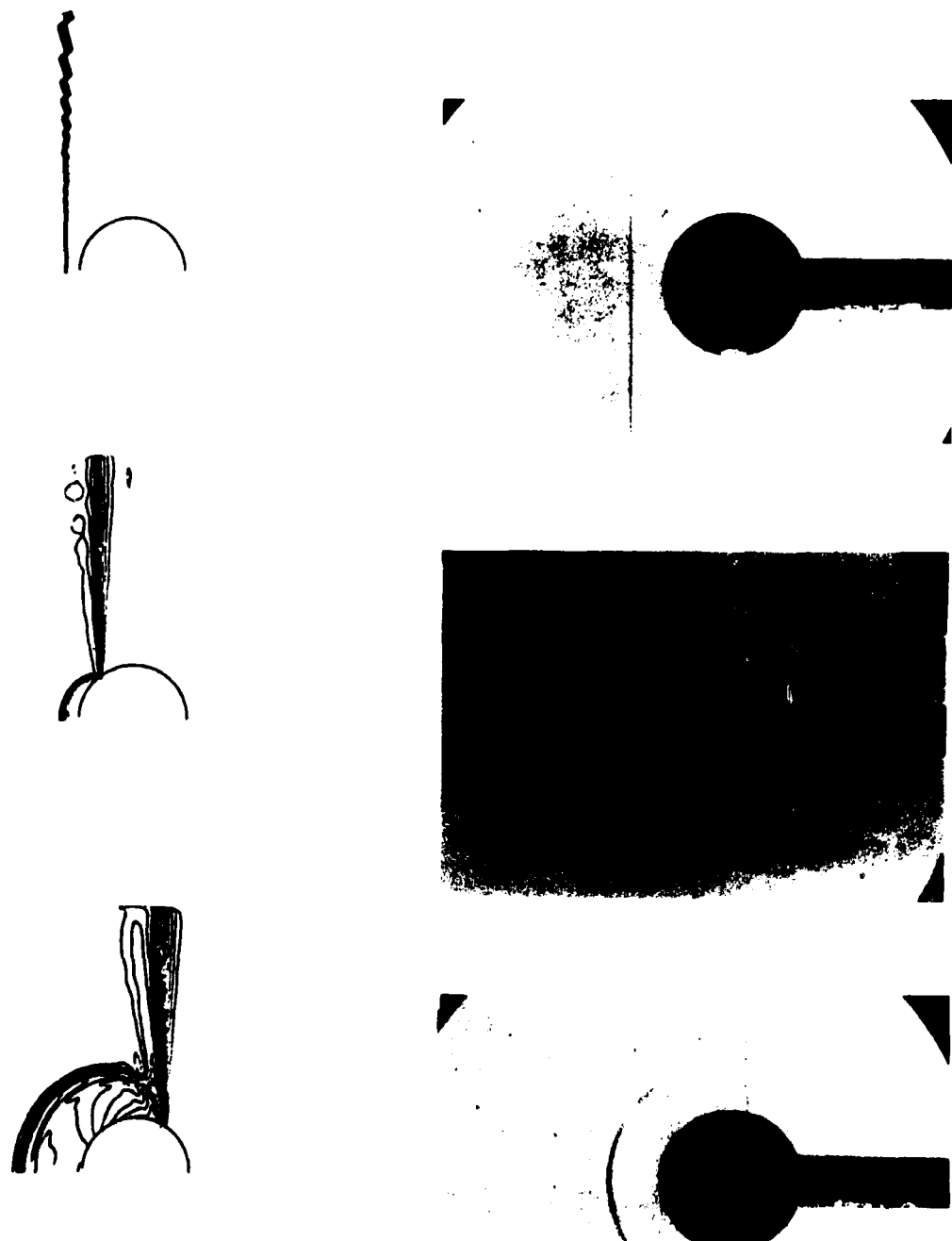


Figure 12. Blast Wave Diffraction Over a Cylinder.

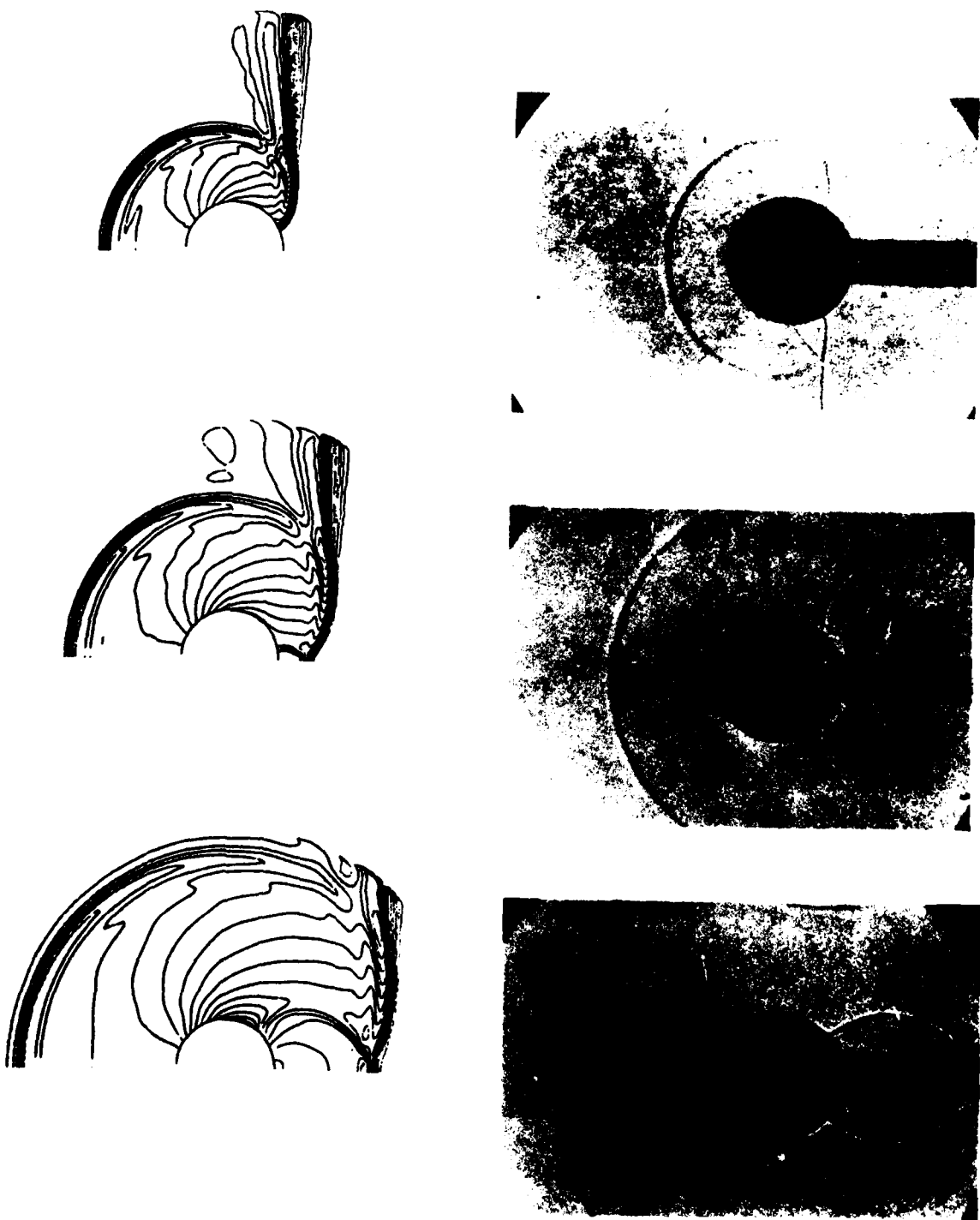


Figure 12. (continued) Blast Wave Diffraction Over a Cylinder

shadowgraphs reproduced from Reference 5.

The shock diffracted around both sides of the cylinder. Figure 12 shows the shock moving from the regular reflection region into the mach reflection region with the development of the mach stem. The figure also shows the expansion of the reflected wave which accounts for the decay of the pressure at stations at 0° through 135° . The reflection of the two halves of the shock at the 180° station is shown in the last few plots. The shock reflected at the rear of the cylinder is responsible for the second pressure jump at the station at 75° through 165° .

It takes 0.96 ms for the shock to envelop the cylinder. It takes approximately another 5 ms for the pressure to settle to its drag phase level. The pressure loading remains approximately constant for 140 ms until the arrival of the first rarefaction wave.

The target deformation resulting from the blast loading is shown in Figure 13. The figure contains three isometric projection plots of one half of the target cylinder and three matching center cross sections. The loading direction during the structural test is given by the arrow at the top of the figure. In all plots deviations from the designed radius of 15.34 cm have been magnified by a factor of five to make them more visible.

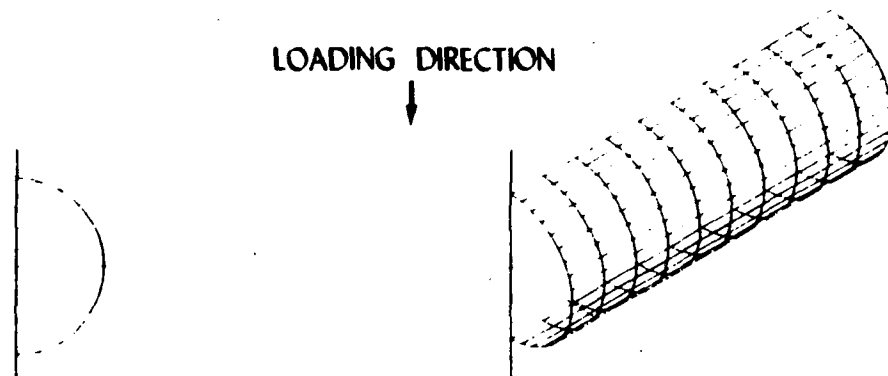
The uppermost pair of plots in Figure 13 shows the right half of the target cylinder before the structural test. Only one half is plotted because the differences in the two halves were very small. The lower two pair of plots show the two halves of the target cylinder after the structural test. In the isometric projections the cylinder has been divided down the center of the loaded face and the halves have been rotated to the right and left.

In Figure 13 the amount of deformation was small even at a magnification factor of five. The largest measured deflection was 3.302 mm or 2.17% of the target radius. The deflections were confined to a region around the center of the loaded face. The deflection patterns were somewhat asymmetric about the center of the loaded face.

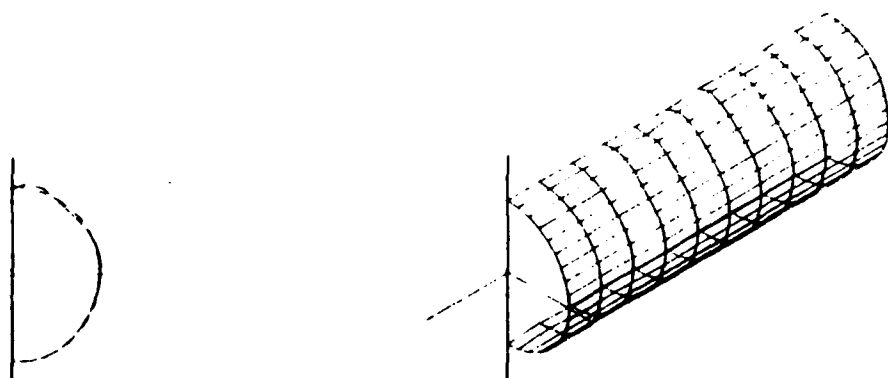
Figure 14 shows an enlarged view of the central cross section of the target cylinder after the structural test. In Figure 14 deviation from the designed radius of 15.34 cm have been magnified by a factor of eight. The front half of the target shows a lobed buckling pattern with a half-wave length of approximately 36° . The asymmetry of the buckling can be seen more clearly in this figure. The post-test buckling pattern shown by the solid line seems to be influenced by the pre-test imperfection shown by the dashed line.

⁵ W. Heilig, "About Shock Wave Transition Phenomena in Non-Stationary Flows," Proceedings of the 7th International Symposium on Military Applications of Blast Simulation, Medicine Hat, Alberta, Canada, 13-17 July 1981.

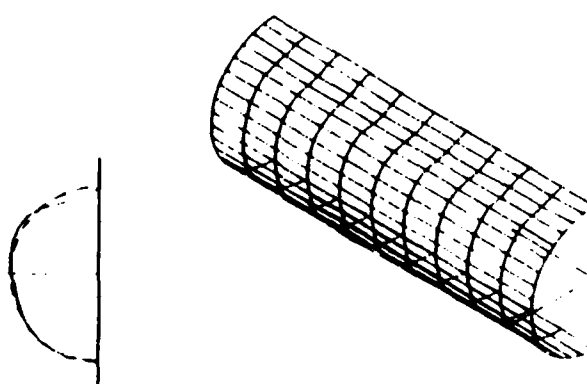
DEFLECTION MAGNIFICATION 5X



PRE-TEST TARGET SHAPE - RIGHT HALF

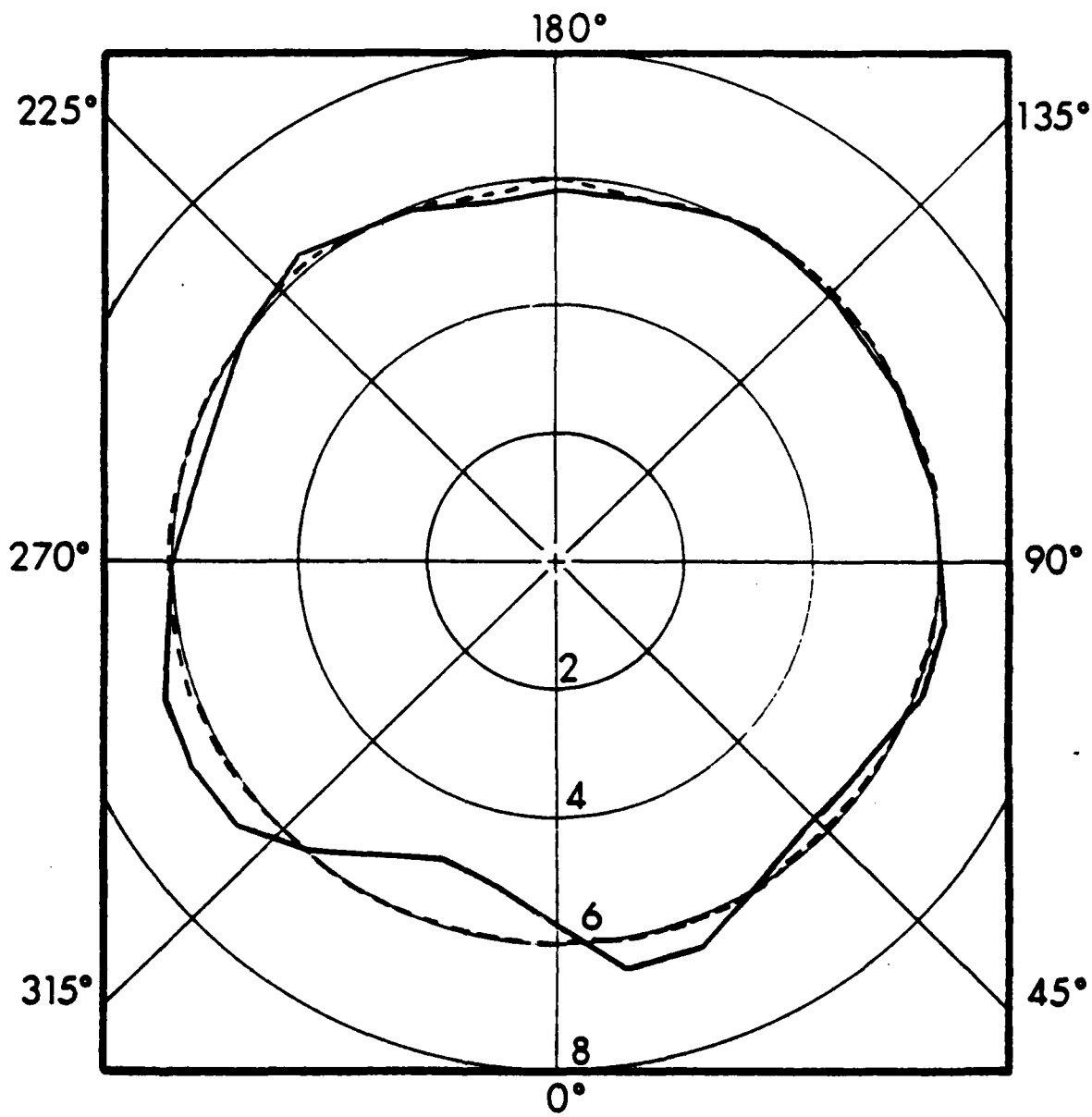


POST-TEST TARGET SHAPE - RIGHT HALF



POST-TEST TARGET SHAPE - LEFT HALF

Figure 13. Three-Dimensional Plots of Target Deformation in Shot 8-80-7.



DEFLECTION X 8
CENTER CROSS SECTION

PRE-SHOT SHAPE -----
POST-SHOT SHAPE ——

Figure 14. Deformation of the Center Cross Section of the Target in Shot 8-8Q-7.

Figures 15 through 19 show the first 10 ms of the strain history on the target cylinder. In these figures the tensile strain is taken as positive and the compressive strain is negative. The first number in the station designation indicates the angular position of the gage. Zero degree is in the center of the loaded face and aligned with the zero degree pressure gage. The second number is related to the distance from the longitudinal center. The final part of the designation indicates whether the strain was measured in the longitudinal or circumferential direction.

Unlike the overpressure histories, the 10 ms strain histories are not easily interpreted. Although the gages were located symmetrically about the center of the loading, they did not produce symmetric results. The asymmetry in the targets response meant that the gages were located at varying distances from the deflection maximums and minimums, making comparison between gages difficult.

One pattern that did occur in the strain history was a response frequency in most of the longitudinal strain histories of approximately 0.59 kHz.

B. Thermal Loading Structural Tests

The second type of structural test conducted involved thermal loading of the target cylinders. Because of the high temperature expected on the front of the target heat curing epoxy had to be used to install the strain gages. In addition, because there was no blast loading involved the pressure gage in the upper bearing mount was not installed. Only one Bytrex gage was used to monitor pressure in the simulator during the thermal source burn.

Two structural tests involving only thermal loading were conducted. In the first test, shot 8-80-8, undetected lightning damage to the simulator's timer caused all the nozzle pairs to fire at the same time. The result was a very sharp thermal pulse with nearly twice the designed flux but less than half the fluence. The rapid burn also caused an unacceptably large pressure pulse in the simulator. The pressure pulse in turn caused molten plastic from the thermal source diaphragm to hit the front of the target. The pressure pulse and molten plastic make the result impossible to analyze in detail; therefore, they are not presented.

The second test involving only thermal loading was shot 8-80-10. In shot 8-80-10 a certain amount of subtle lightning damage to the timer IC's remained causing improper time delays between nozzle firings. The pulse was spread out with a maximum flux lower than the designed level. The fluence level, however, was within 7% of the designed level, so the results were retained.

Figure 20 is a plot of the flux and fluence histories recorded during shot 8-80-10. The fluence curve was obtained by numerical integration of the flux history recorded during the structural test. The temperature in the target at the start of the thermal burn was 27.78 C°.

Figures 21 through 24 show the temperature history at a number of stations on the target cylinder. The first number in the station designation represents

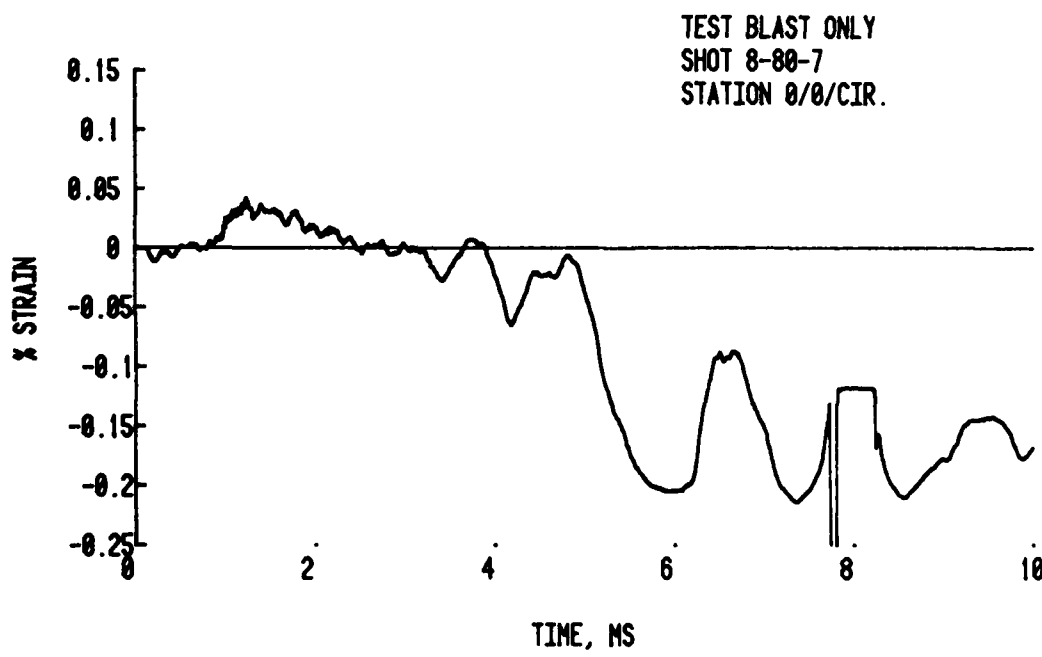
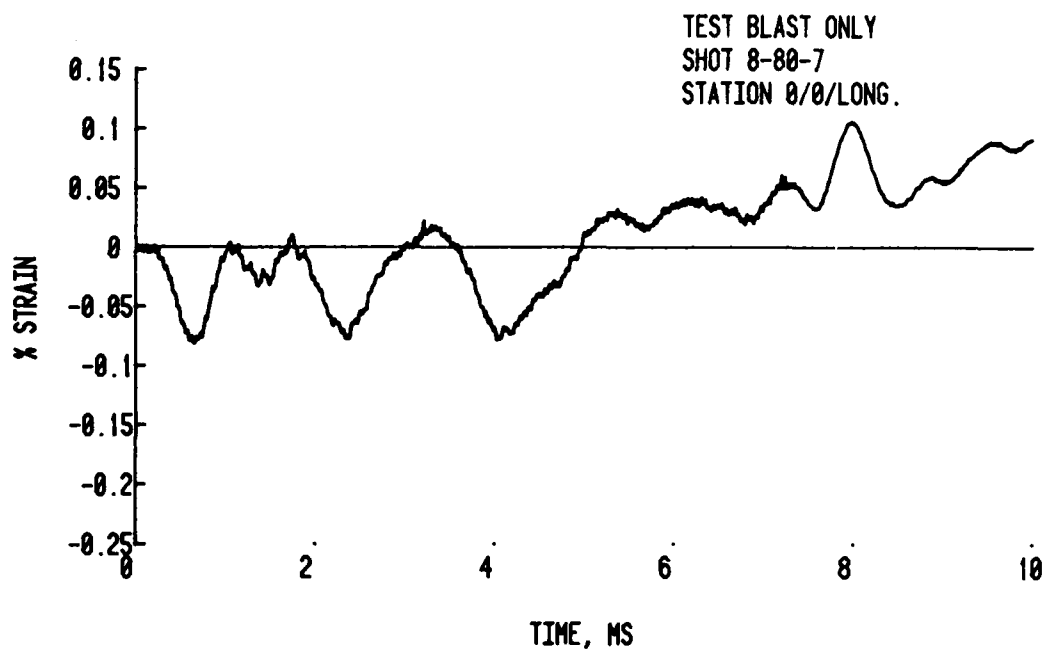


Figure 15. Longitudinal and Circumferential Strain Histories at 0° and the Longitudinal Center.

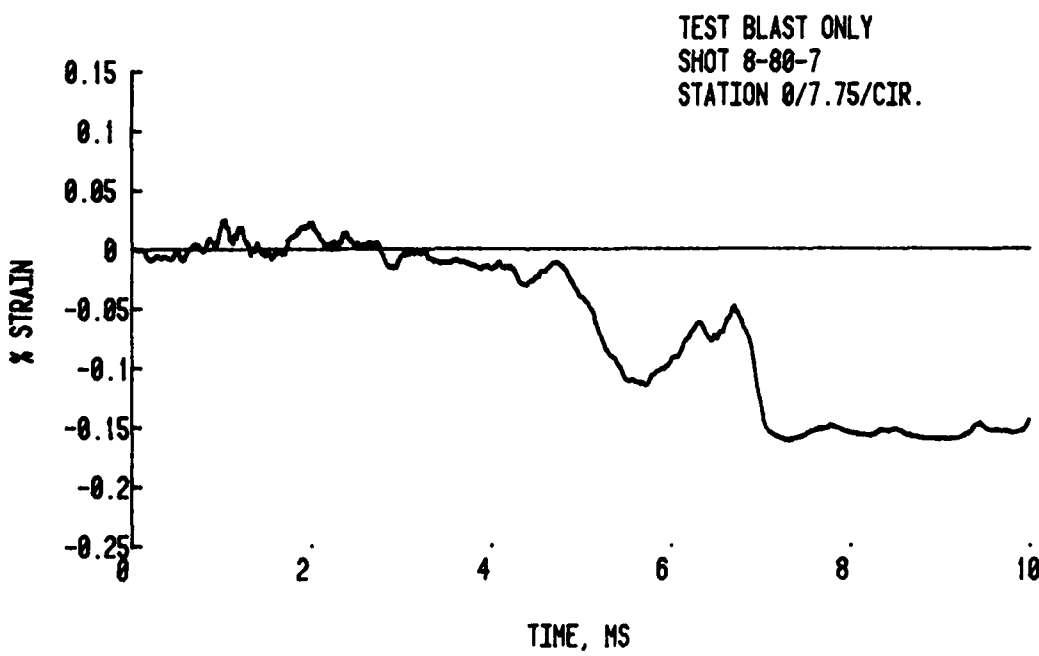
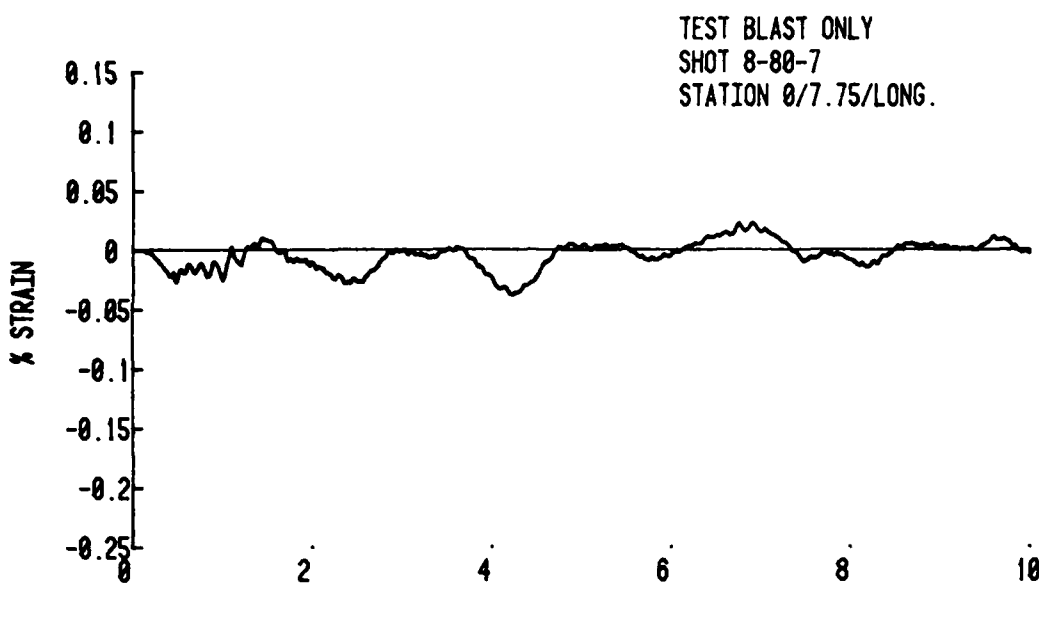


Figure 16. Longitudinal and Circumferential Strain Histories at 0° and 19.69 cm below the Longitudinal Center.

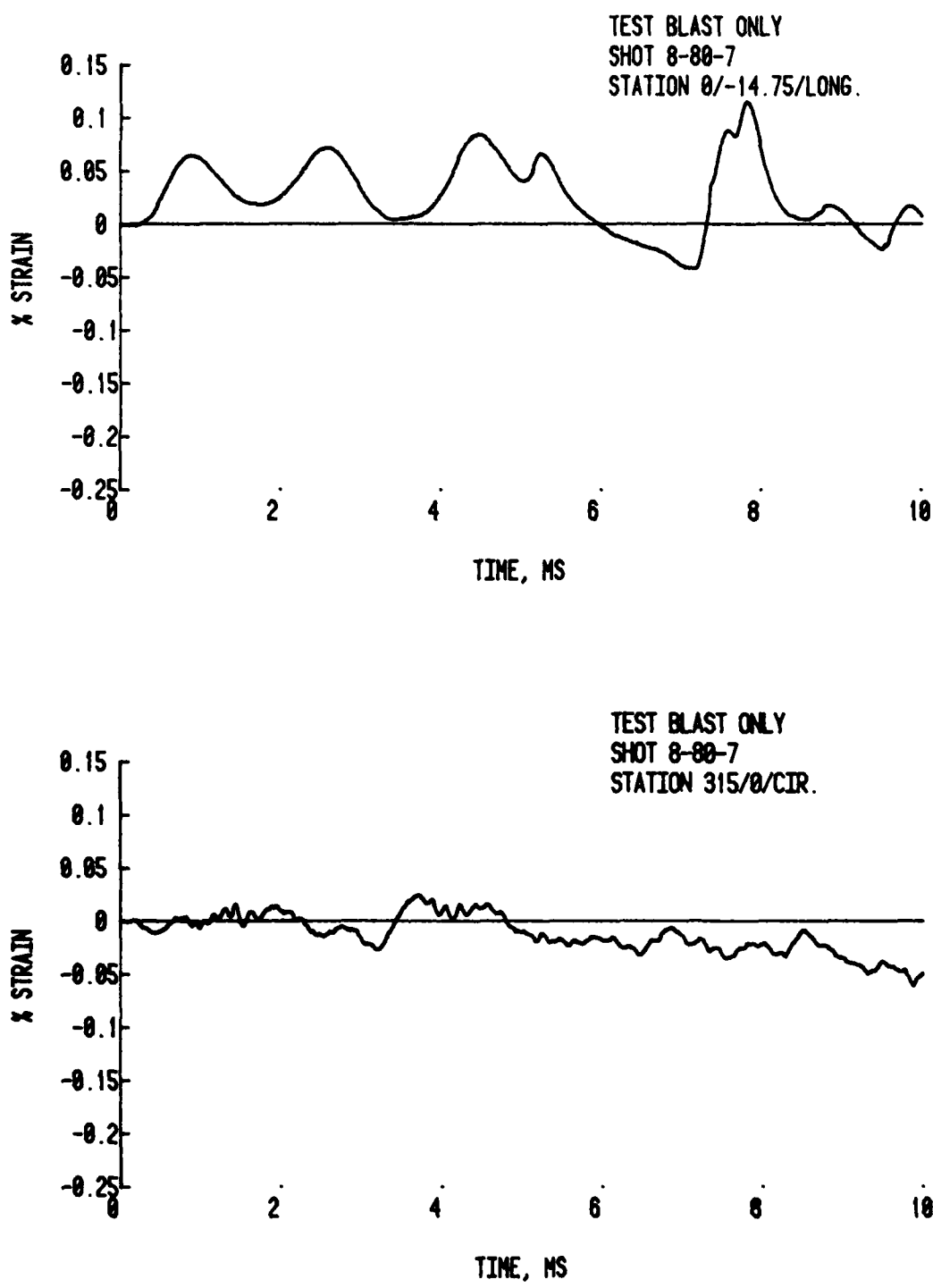


Figure 17. Longitudinal Strain History at 0° and 37.47 cm above the Longitudinal Center and Circumferential Strain History at 315° and the Longitudinal Center.

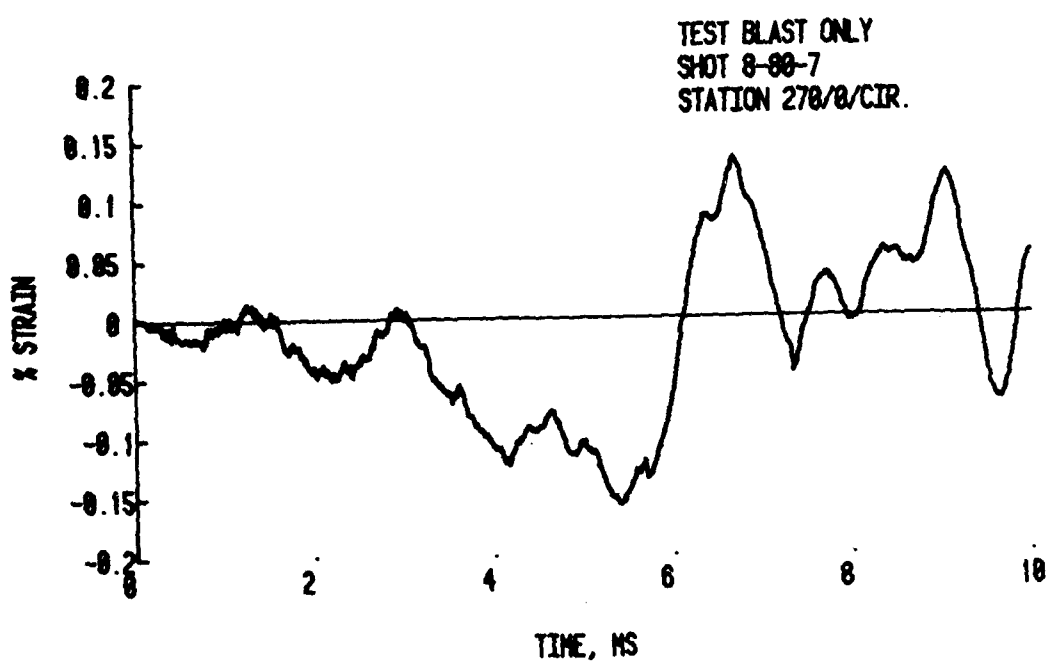
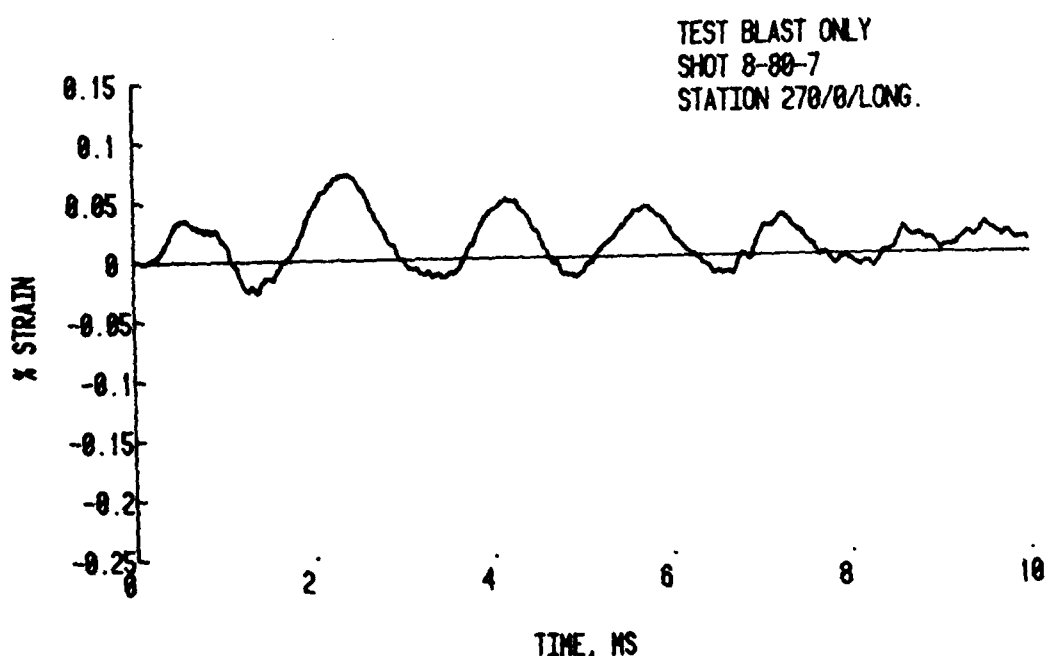


Figure 18. Longitudinal and Circumferential Strain Histories at 270° and the Longitudinal Center.

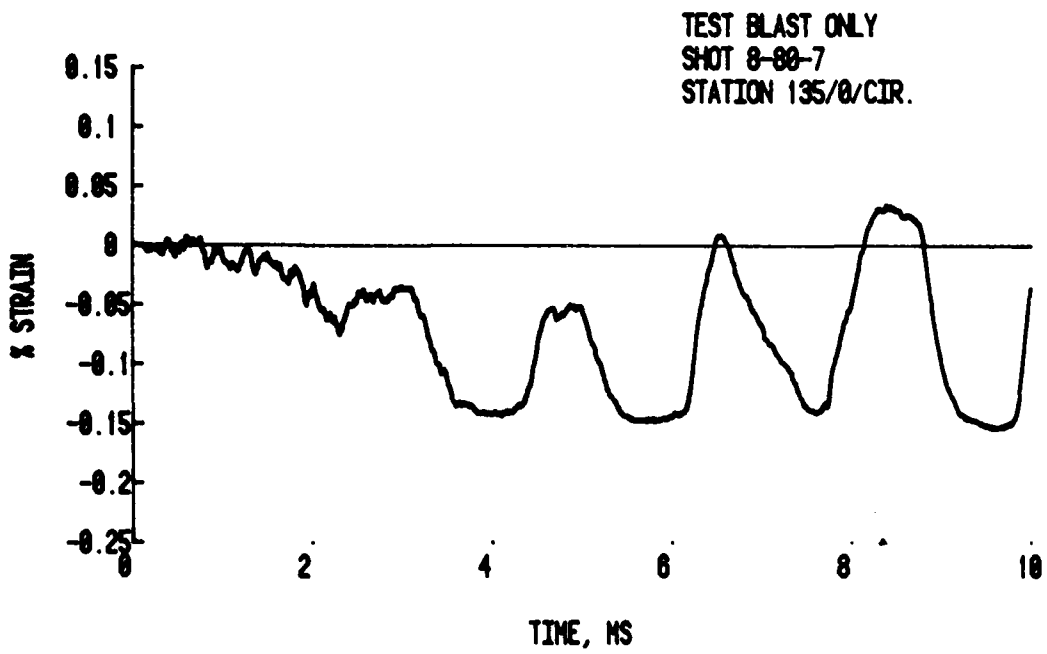
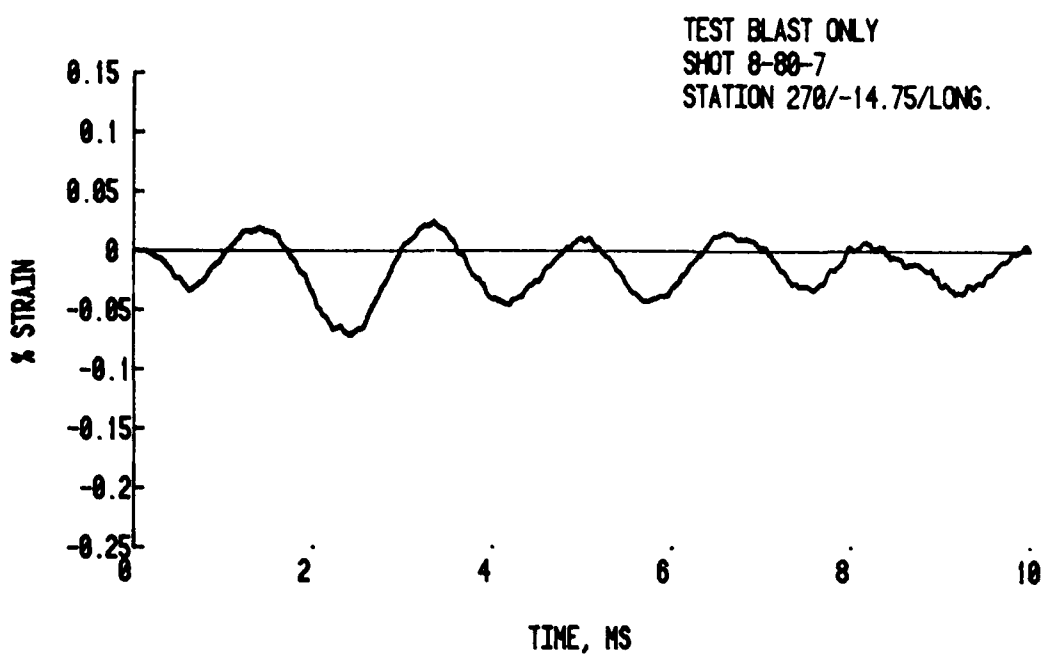


Figure 19. Longitudinal Strain History at 270° and 37.47 cm above the Longitudinal Center and Circumferential Strain History at 135° and the Longitudinal Center.

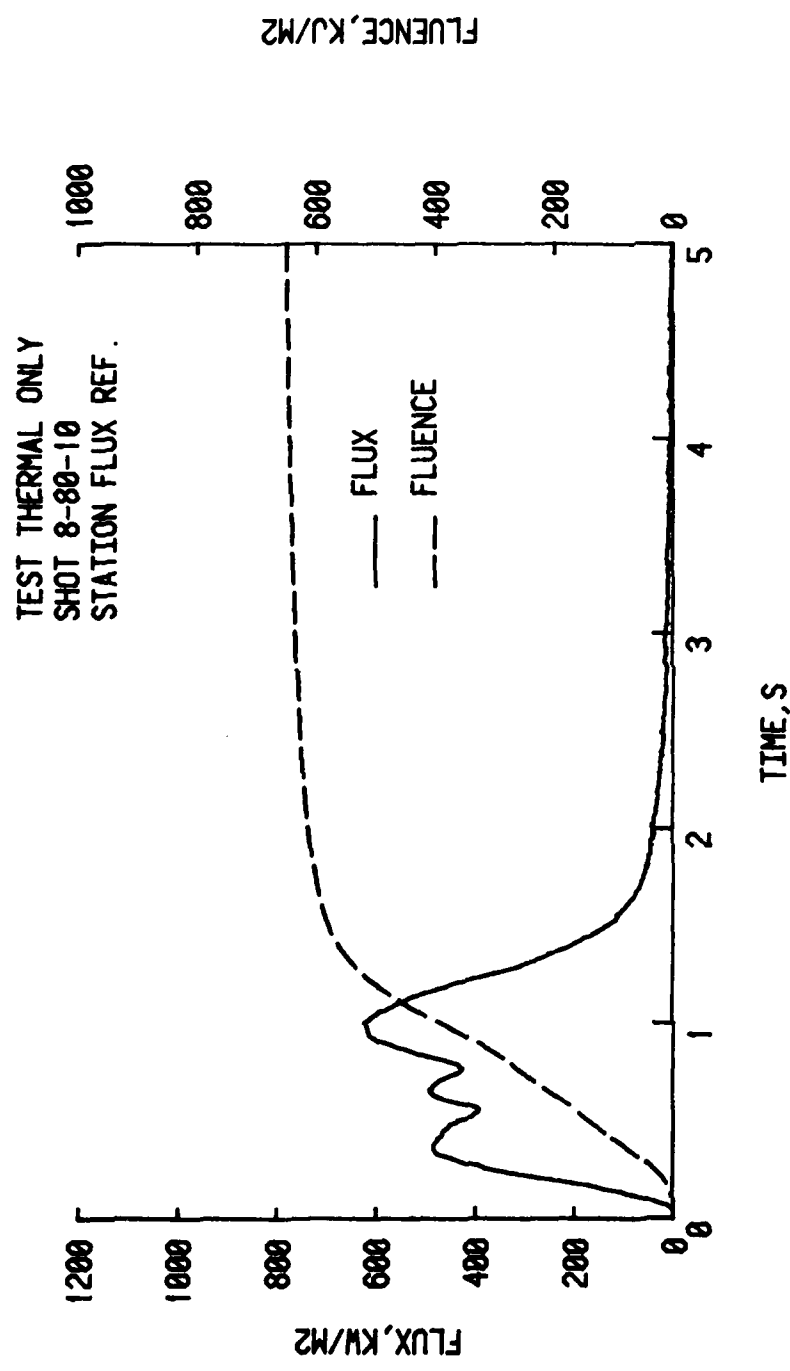


Figure 20. Flux and Fluence Histories in Shot 8-80-10.

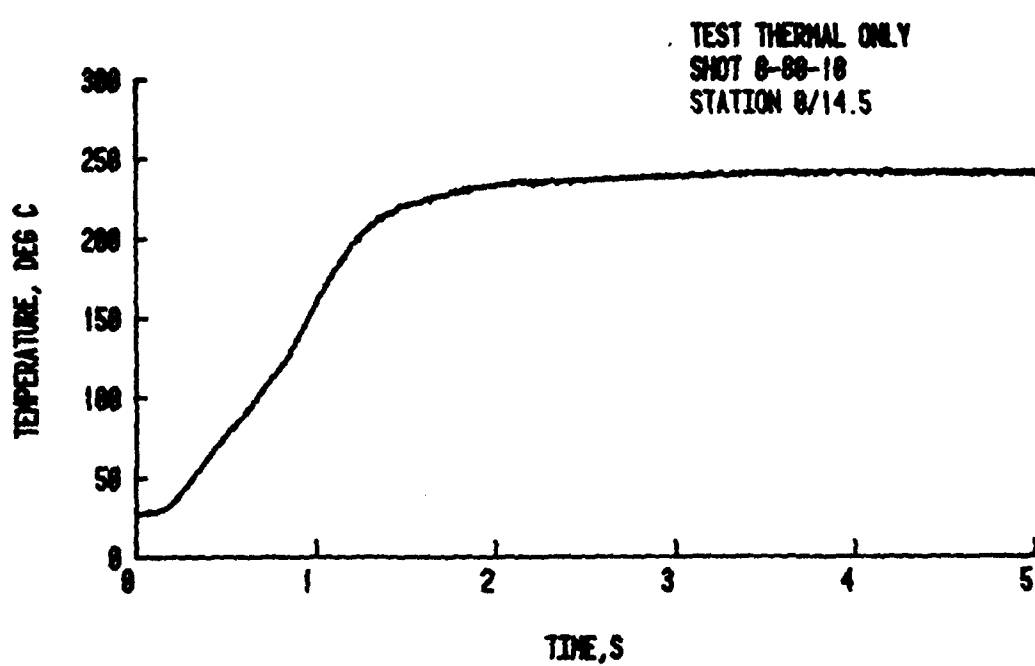
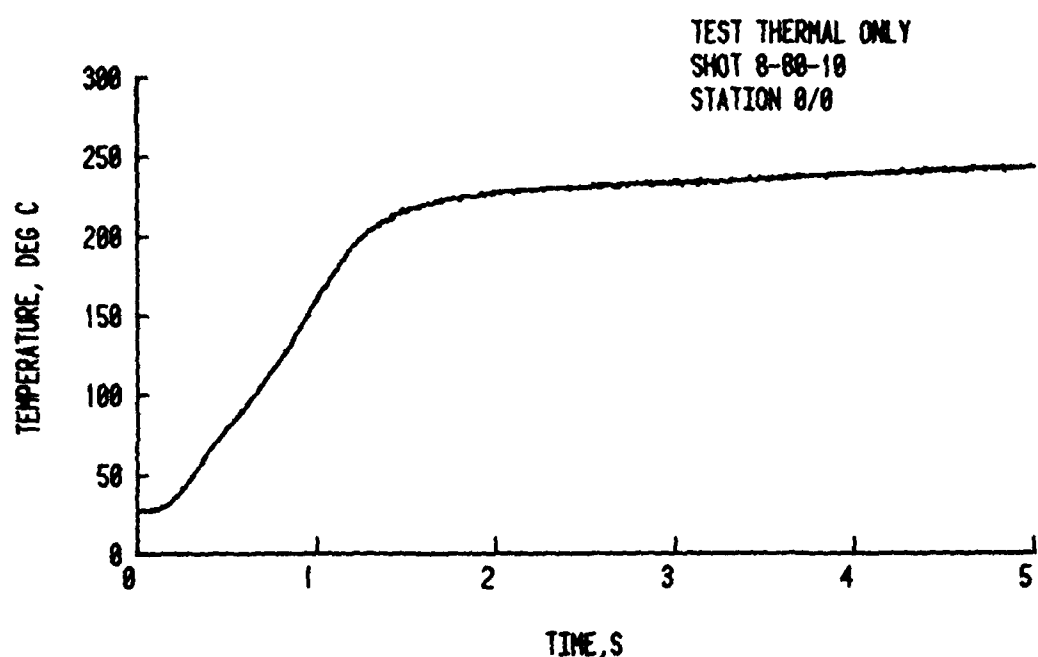


Figure 21. Temperature Histories at 0° and the Longitudinal Center and at 0° and 37.47 cm below the Center.

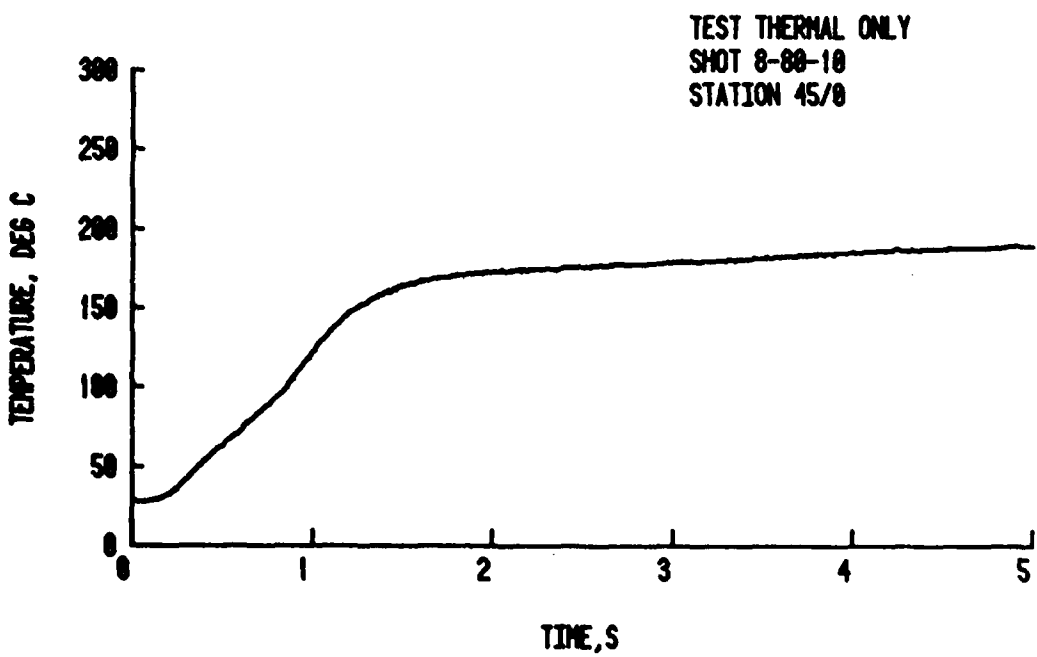
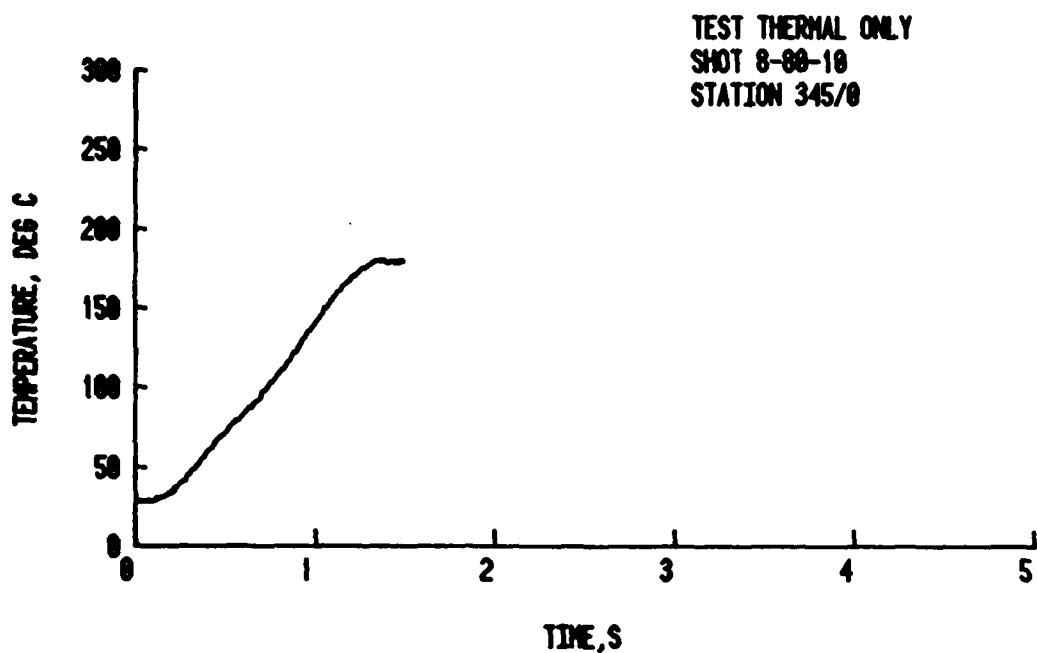


Figure 22. Temperature Histories at 345° and the Longitudinal Center and at 45° and the Longitudinal Center.

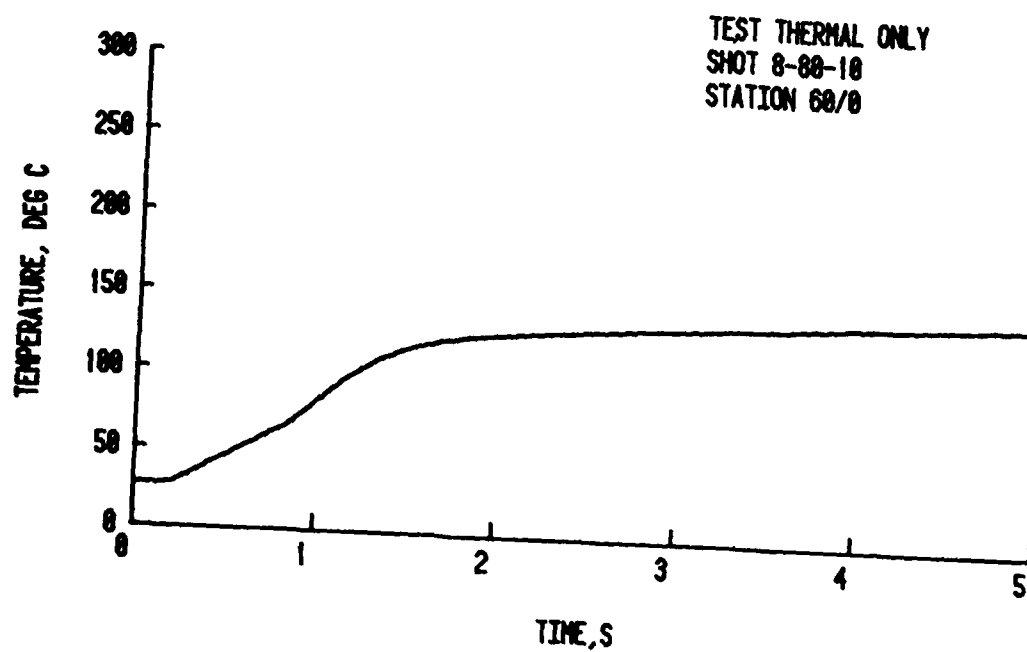
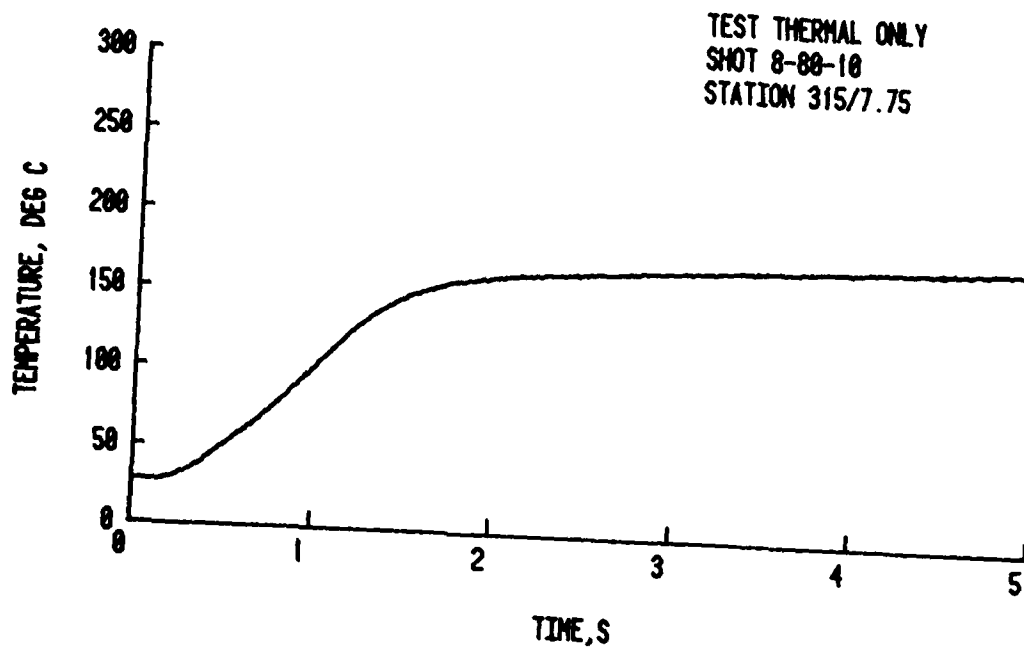


Figure 23. Temperature Histories at 315° and 19.69 cm below the Longitudinal Center and at 60° and the Longitudinal Center.

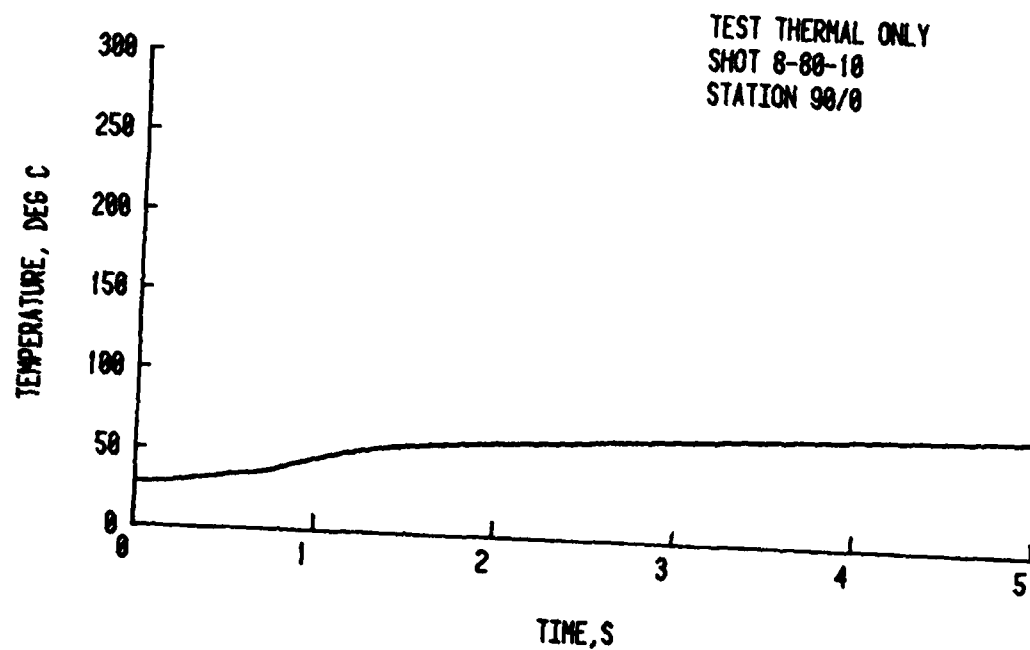


Figure 24. Temperature History at 90° and the Longitudinal Center.

the angular location of the thermocouples used to record the temperature history. The angles used are the same as those used in designating the pressure and strain gage locations. The second number indicates the longitudinal distance along the cylinder.

The history at 345° and the longitudinal center line was lost prematurely. The bond between the thermocouple and the target failed at approximately 1.25 seconds so the plot was truncated.

The shape of all the temperature histories is similar to the fluence history. The maximum temperature reached decreased rapidly with increasing angle but shows only a minor decrease with distance from the longitudinal center. There was little change in the temperature after the end of the thermal source burn indicating that heat loss by reradiation, conduction and convection were small in the time of interest.

Figure 25 shows the target deformation resulting from the thermal loading. The format used is the same as in Figure 13. The plots show that the major part of the deformation was confined to a narrow region on the front, near the clamped ends. The deformation pattern is again asymmetric, but the asymmetry was not as pronounced as in the blast loading test. The maximum measured permanent deformation was 4.013 mm or about 2.62% of the target radius.

Figures 26 and 27 show enlarged cross sections of the target using the same format as Figure 13. Figure 26 shows the central cross section. Figure 26 is shown merely for comparison. There was little change between the central cross section pre-shot and post-shot shapes. Figure 27 shows the cross section 33 cm above the center in the region of maximum deflection. The figure clearly shows the deformation pattern.

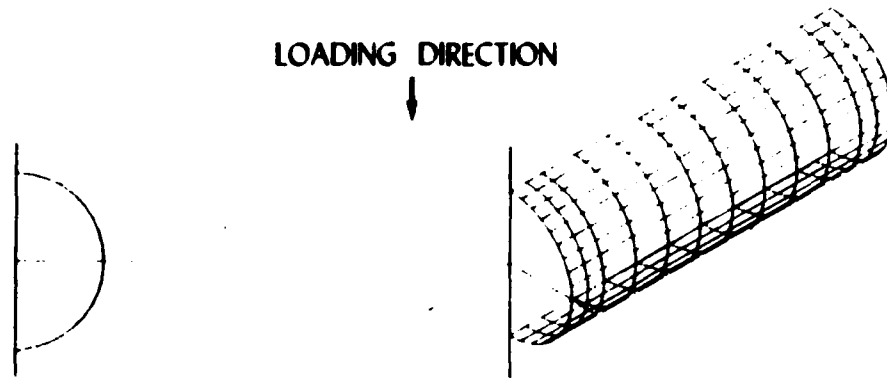
Figures 28 through 33 show the strain histories during the first 5 seconds after the beginning of the thermal burn. The format for the station designation used here is the same as that used in shot 8-80-7. The solid lines shown in the figure are the strain histories recorded during the structural tests. The dashed lines are the strain histories after correction for the thermal effects. The corrections were made using the techniques outlined in Section IIB.

Again, there is no simple method of relating the strain histories taken at different stations due to the asymmetry in the target response. The histories show a sharp change in strain amplitude at approximately 1 second into the thermal source burn. The change at one second is larger on the station on the front of the target but is evident to some degree on all the stations. The time of the change correlates well with the timing of the thermal buckling seen on high-speed films of the test.

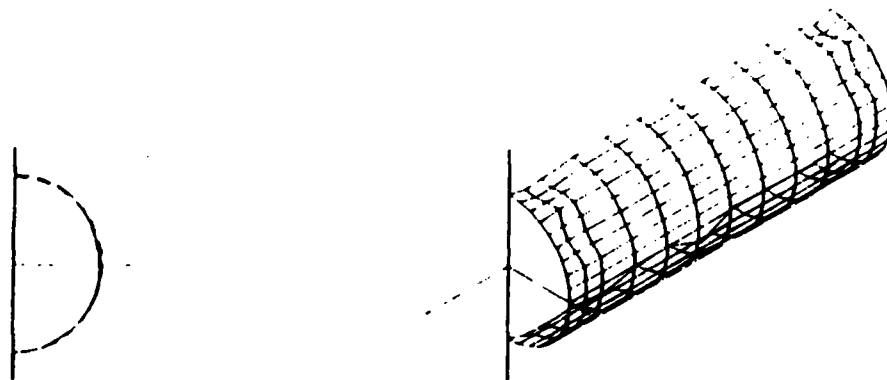
C. Thermal/Blast Loading Structural Tests

The final type of structural test conducted involved both thermal and

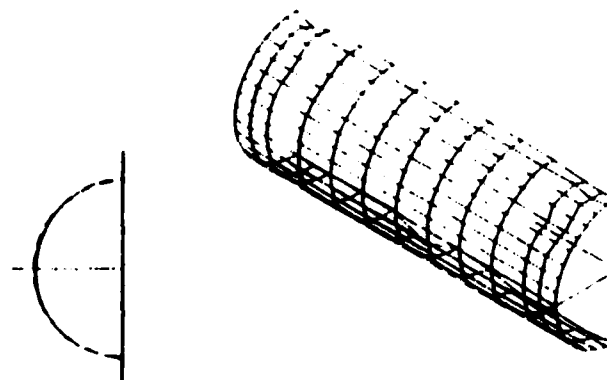
DEFLECTION MAGNIFICATION 5X



PRE-TEST TARGET SHAPE - RIGHT HALF

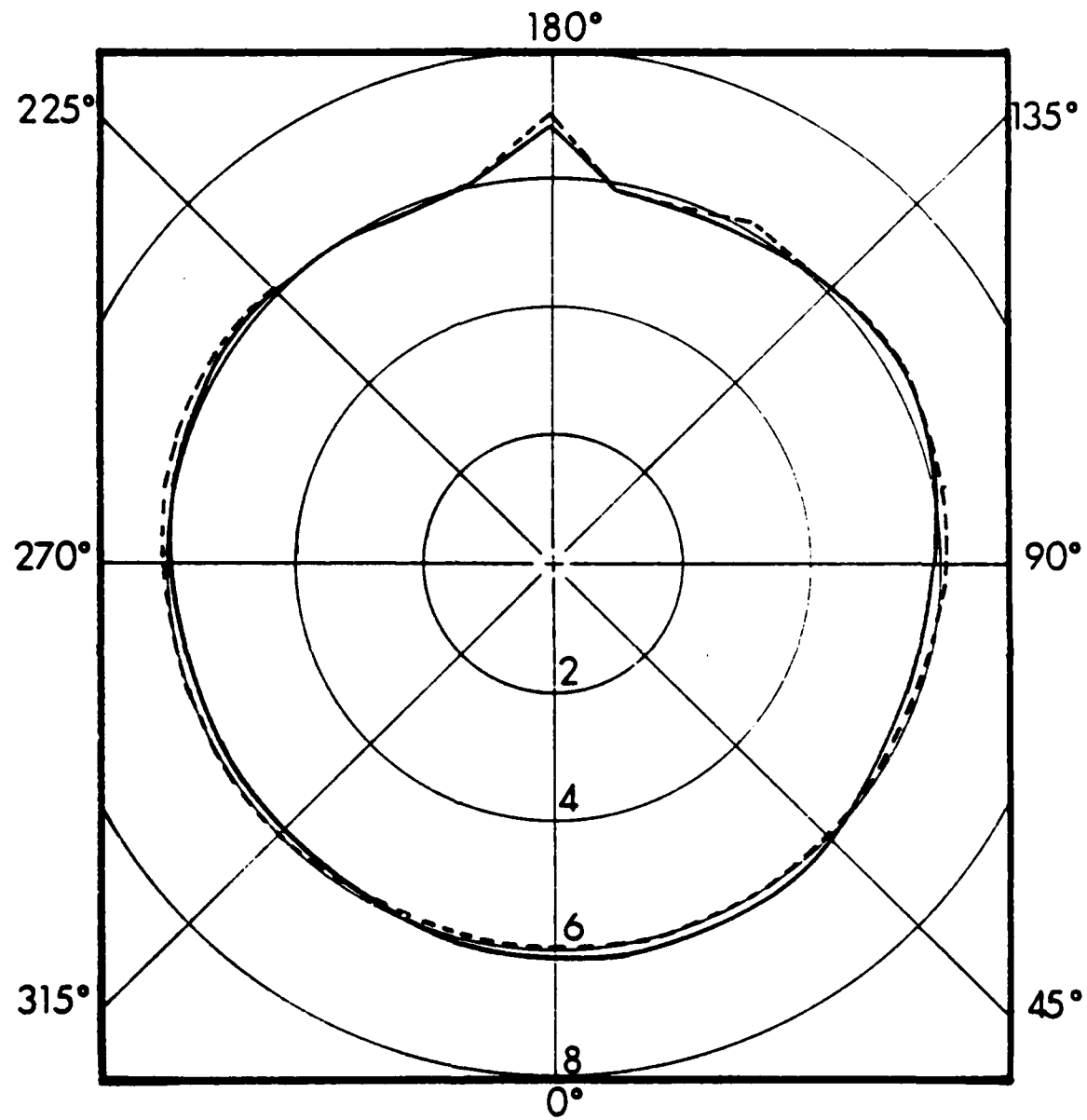


POST-TEST TARGET SHAPE - RIGHT HALF



POST-TEST TARGET SHAPE - LEFT HALF

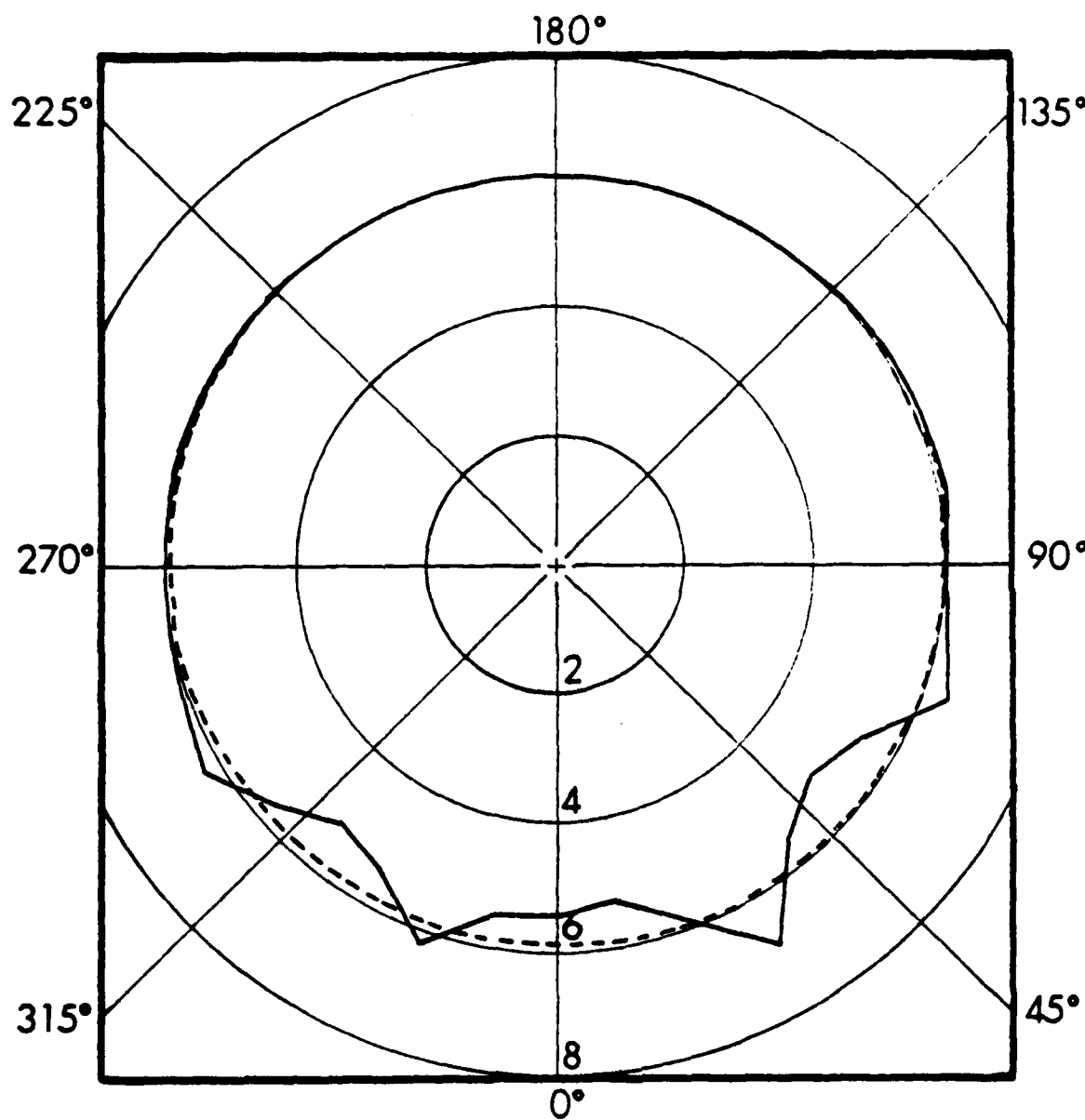
Figure 25. Three-Dimensional Plots of Target Deformation in Shot 8-80-10.



DEFLECTION X 8
CENTER CROSS SECTION

PRE-SHOT SHAPE -----
POST-SHOT SHAPE ——

Figure 26. Deformation of the Central Cross Section of the Target in Shot 8-80-10.



DEFLECTION X 8
CROSS SECTION 33cm
ABOVE CENTER

PRE-SHOT SHAPE -----
POST-SHOT SHAPE ——

Figure 27. Deformation of the Cross Section 33 cm above the Target Center in Shot 8-80-10.

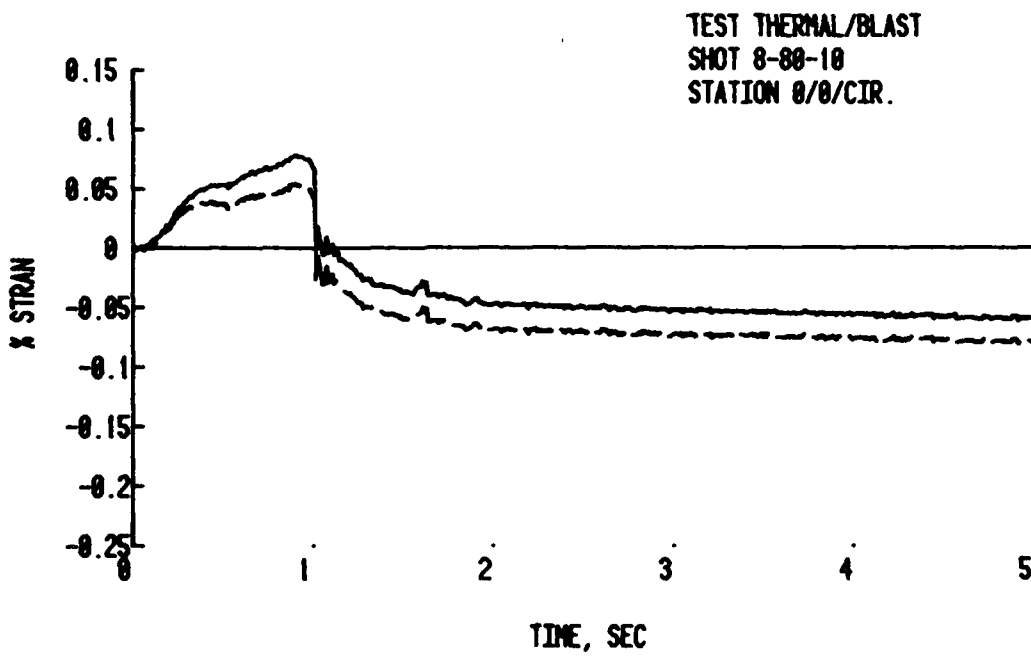
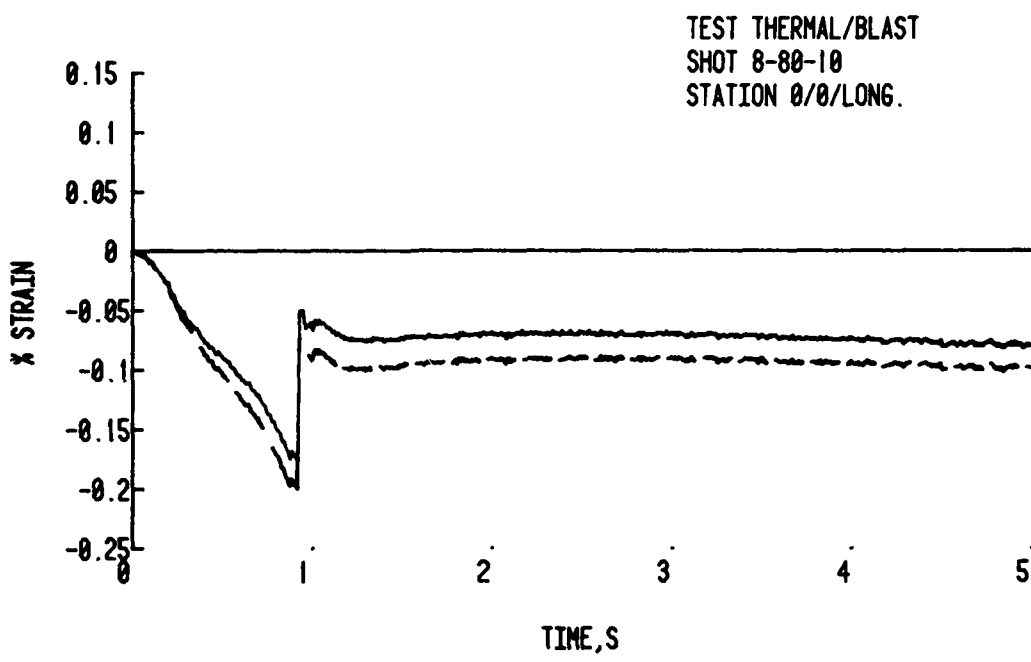


Figure 28. Longitudinal and Circumferential Strain Histories at 0° and the Longitudinal Center.

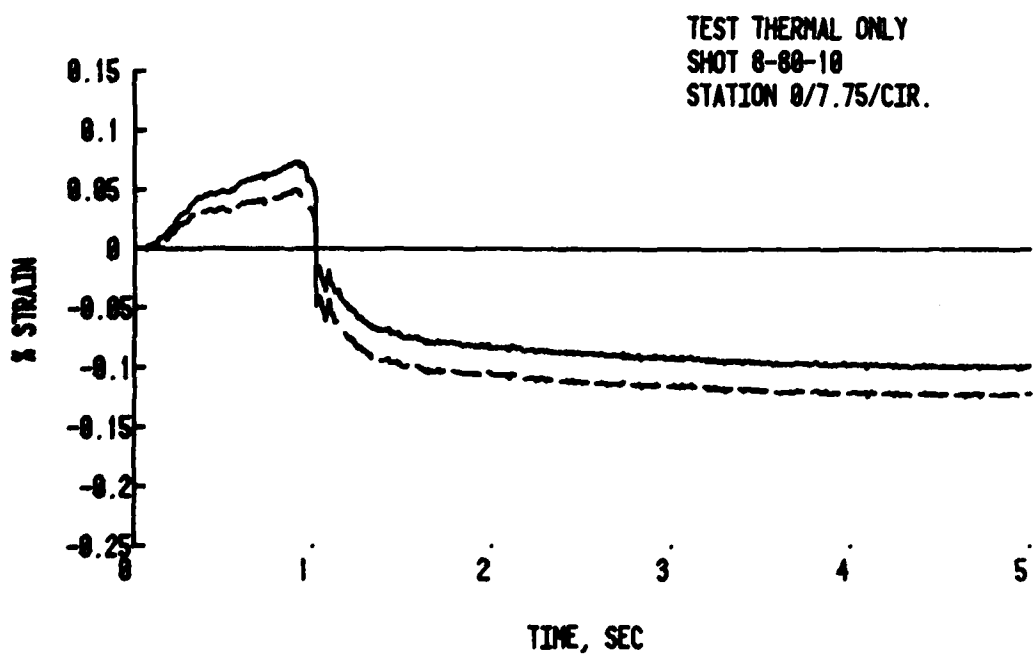
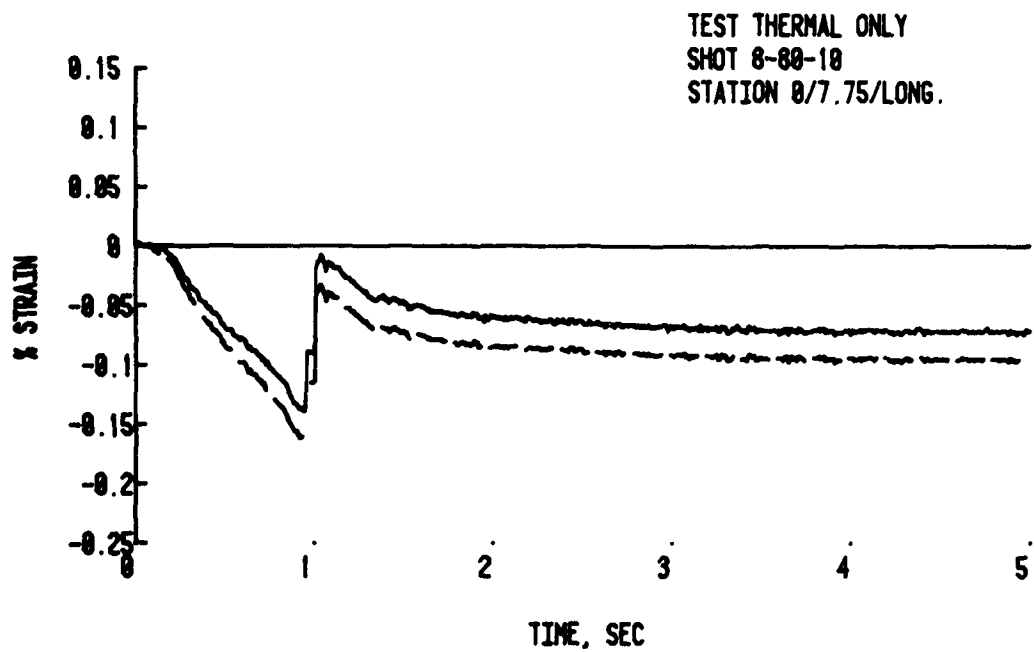


Figure 29. Longitudinal and Circumferential Strain Histories at 0° and 19.69 cm below the Longitudinal Center.

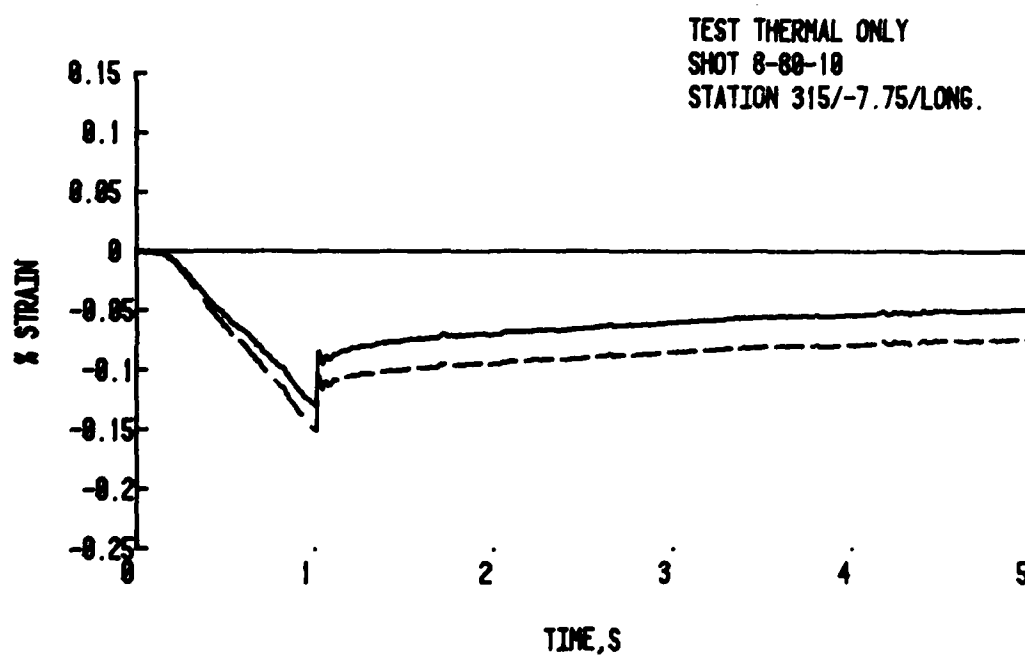
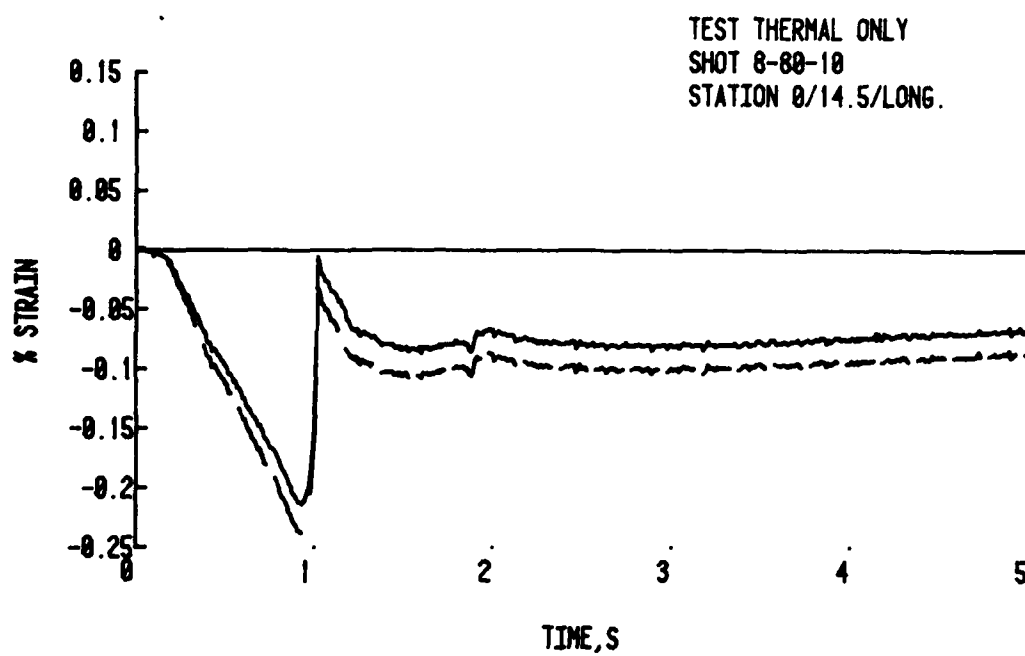


Figure 30. Longitudinal Strain Histories at 0° and 37.47 cm below the Longitudinal Center and at 315° and 19.69 cm above the Longitudinal Center.

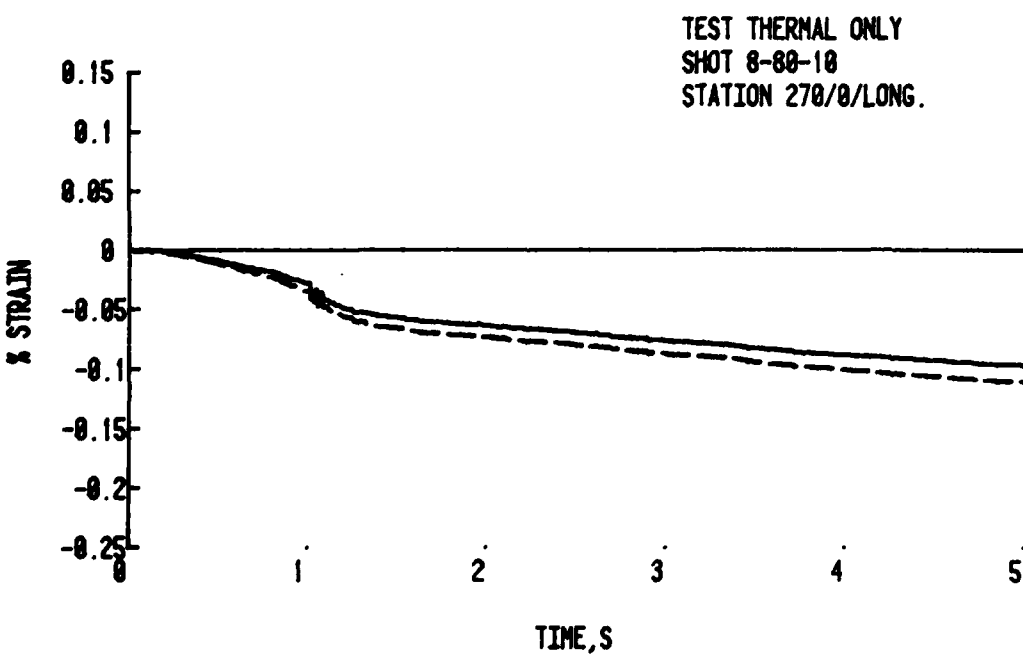
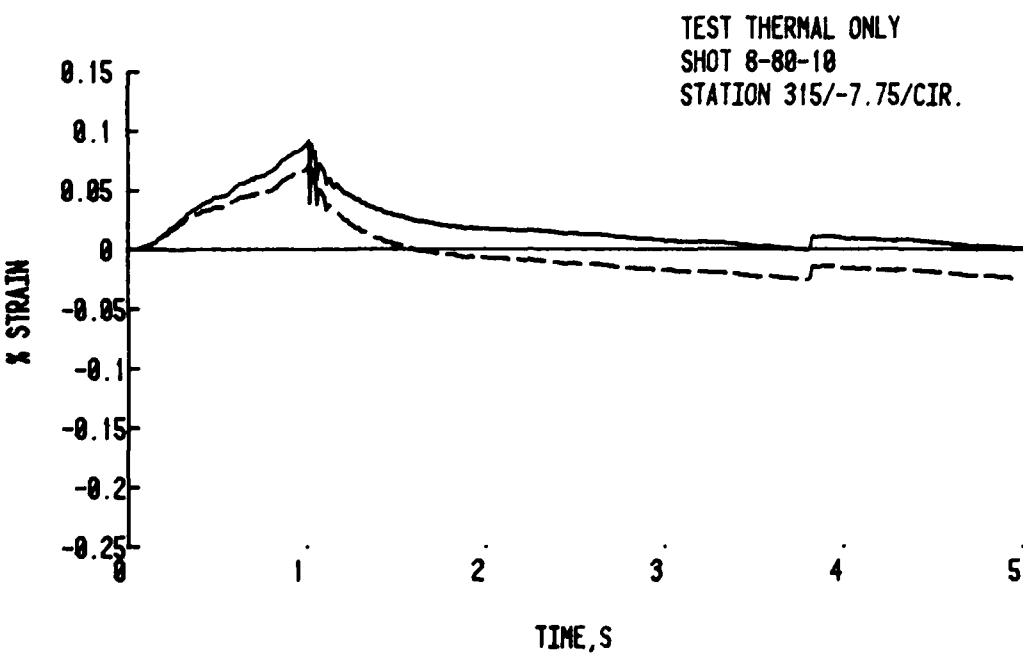


Figure 31. Circumferential Strain History at 315° and 19.69 cm above the Longitudinal Center and Longitudinal Strain History at 270° and the Longitudinal Center.

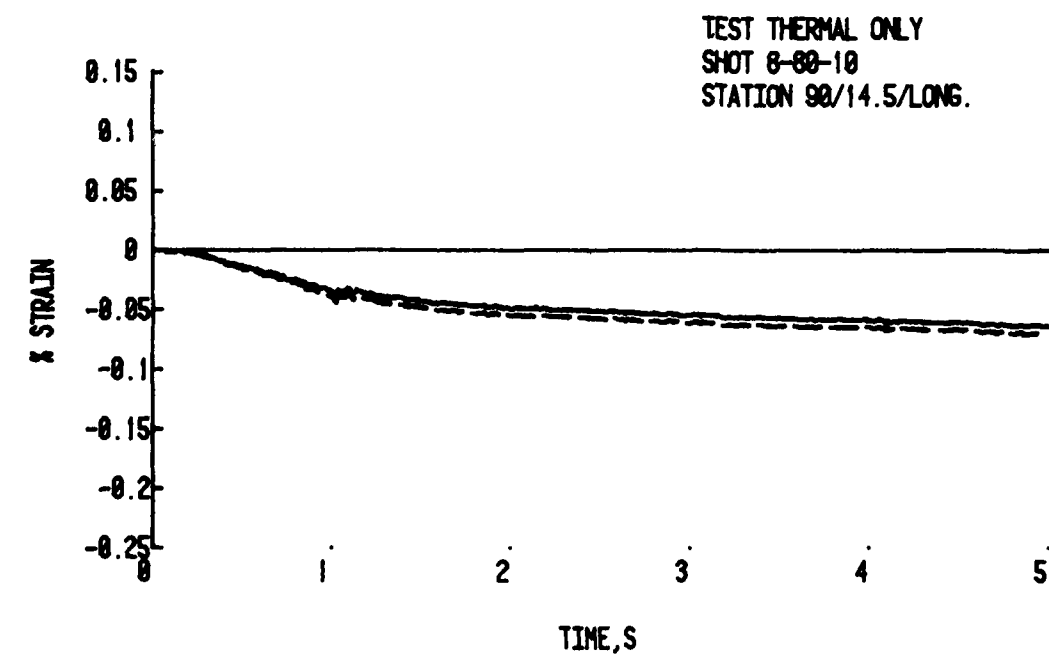
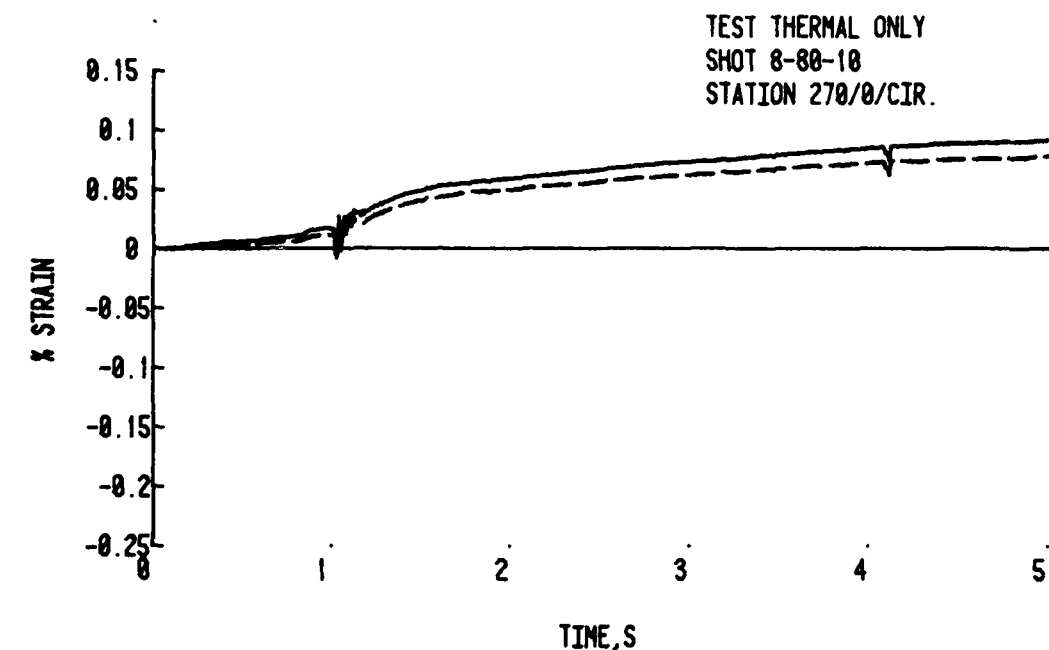


Figure 32. Circumferential Strain History at 270° and the Longitudinal Center and Longitudinal Strain History at 90° and 37.47 cm below the Longitudinal Center.

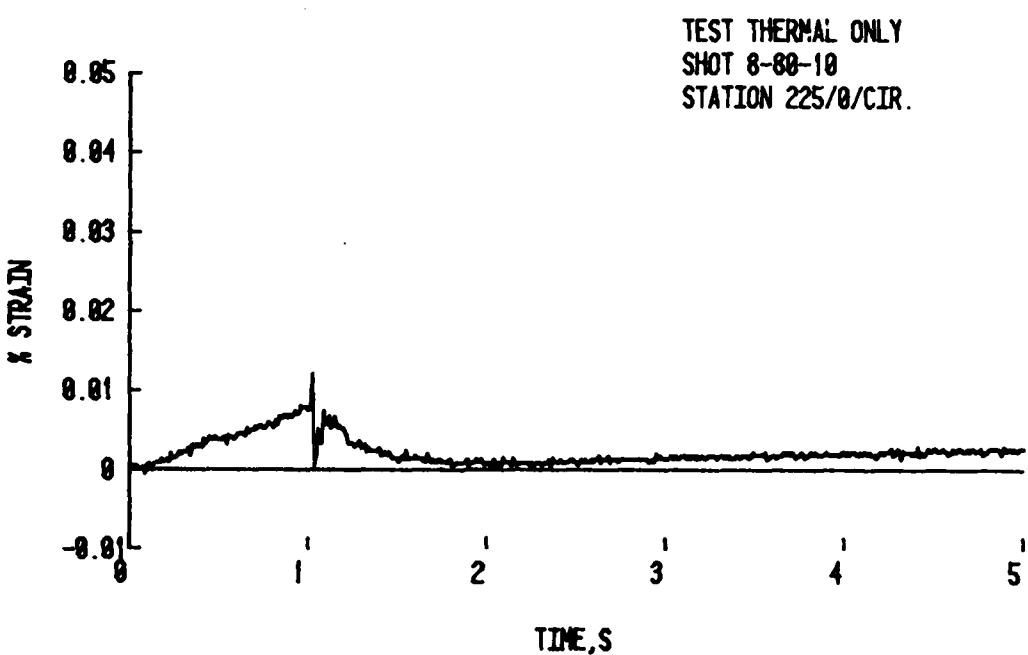


Figure 33. Circumferential Strain History at 225° and the Longitudinal Center.

blast loading in a full simulation as described in Section II C. Heat curing epoxy was again used to install the strain gages. The full complement of instrumentation was used, including pressure gages, thermocouples, strain gages and a flux gage.

Two combined thermal/blast structural tests were conducted. In the first test, shot 8-80-9, severe thermal drift problems with all but the 0° Endevco pressure gage in the upper bearing mount prevented an accurate reading of the blast loading history on the target. The results of this test led to the development of the extra protective cap described in Section II B. In addition, problems with the simulator controller timer again caused the thermal source to produce a pulse similar to the pulse in shot 8-80-10.

The second combined thermal/blast loading test was shot 8-81-1. The repaired simulator control timer produced a thermal pulse shape very near the designed pulse shape. The additional protective caps prevented the thermal drift problem found in the previous test, although gages at 70° and 150° failed due to other causes. The structural response of the target was similar to that found in shot 8-80-9.

Figure 34 shows the flux and fluence histories recorded during shot 8-81-1.

The temperature of the target at the start of the thermal source burn was 8.33 C°.

Figure 35 through 37 show the temperature histories on the target cylinder during the structural test. Because the use of additional pressure gage recording channels were not available for thermocouples at 15° and 60°. The thermocouple at the center of the loaded face debonded from the target early in the thermal burn and is not shown.

Figure 38 shows the stagnation overpressure history of the incident shock wave. The overpressure history shows evidence of the influence of the preceding thermal source burn in the simulator. The effects are similar to those in a number of other combined thermal/blast simulation and are discussed in detail in Reference 6.

Qualitatively, the interaction of the incident shock wave and the hot gas from the thermal source can be outlined. When the shock enters the hot gas region near the thermal source, a weakened shock is transmitted into the hot gas and a rarefaction is reflected back upstream into the cold gas. When the shock exits the hot gas region, a shock is transmitted into the cold gas downstream and a compression wave is transmitted back into the hot gas and eventually passes back into the cold gas upstream.

A second effect is the "smearing" or rounding of the shock front by non-uniformities in temperature and density in the turbulent hot gas region produced by the thermal source. A final effect seen in the records is an

⁶C. W. Kitchens, R. E. Lottero, A. Mark and G. D. Teel, "Blast Wave Modification During Combined Thermal/Blast Simulation Testing," U.S. Army ARRAADCOM, Ballistic Research Laboratory, Aberdeen Proving Ground, MD, Report No. ARBRL-TR-02352, July 1981 (AD B059761L).

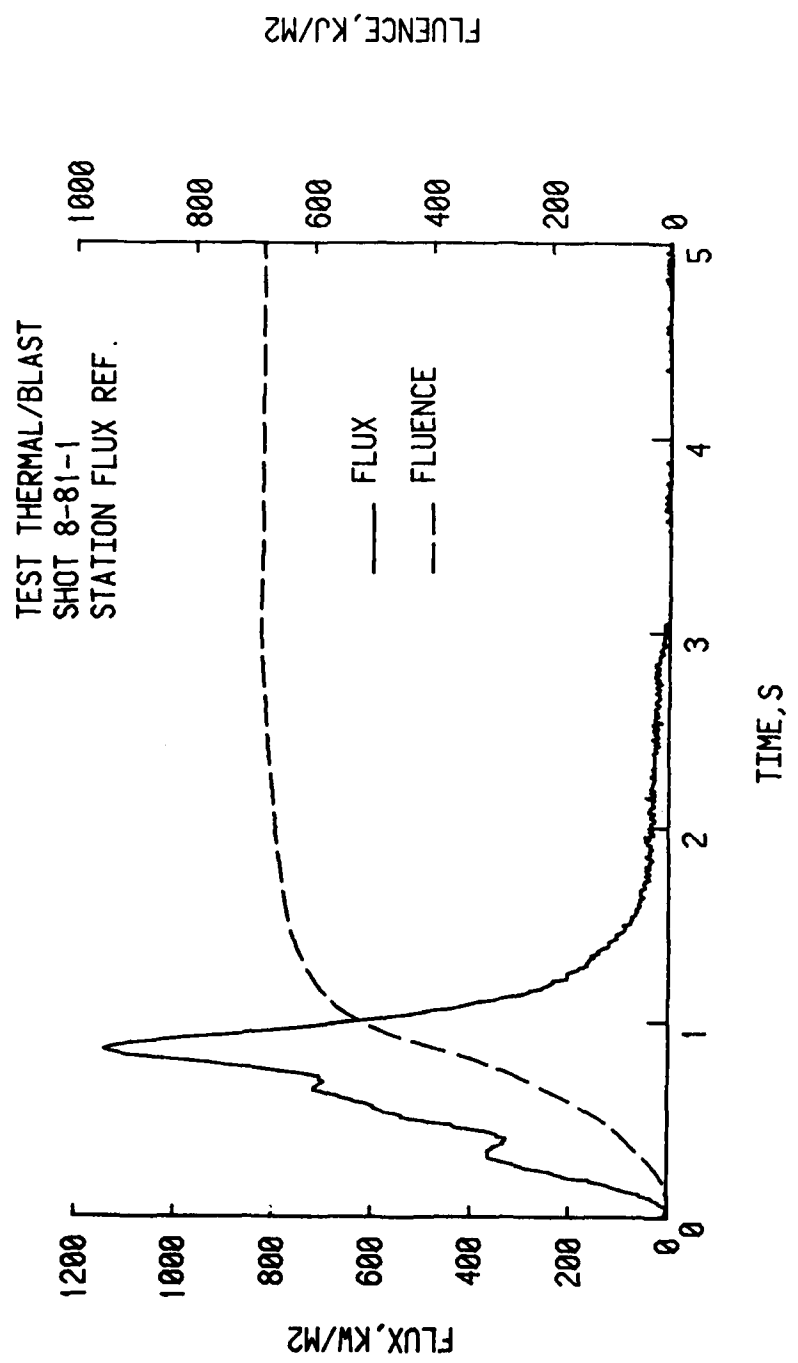


Figure 34. Flux and Fluence Histories in Shot 8-81-1.

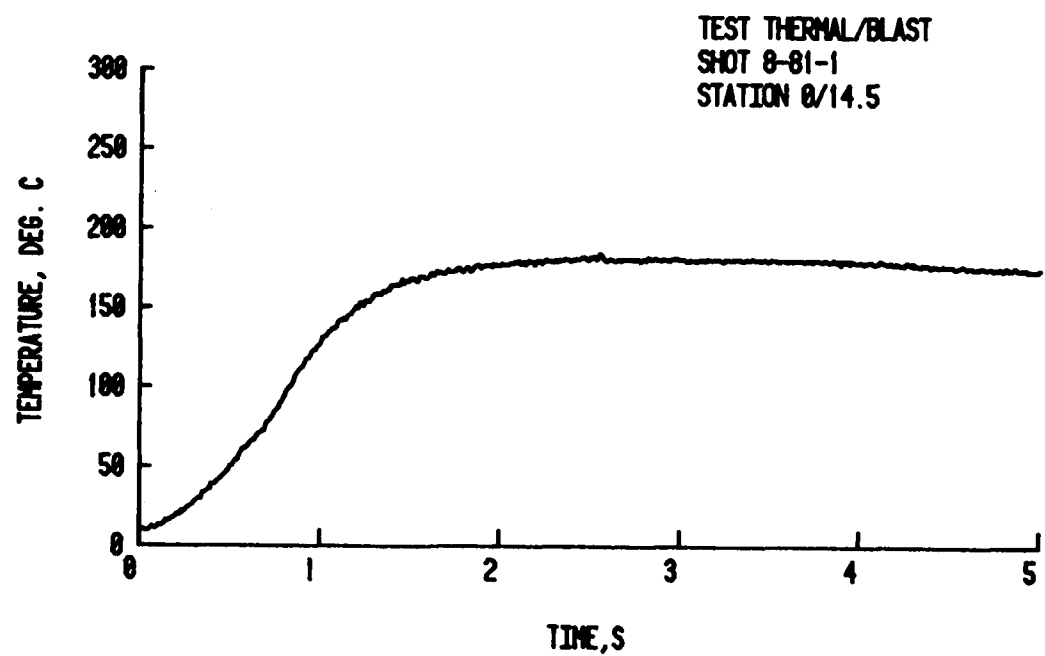


Figure 35. Temperature History at 0° and 37.47 cm below the Center.

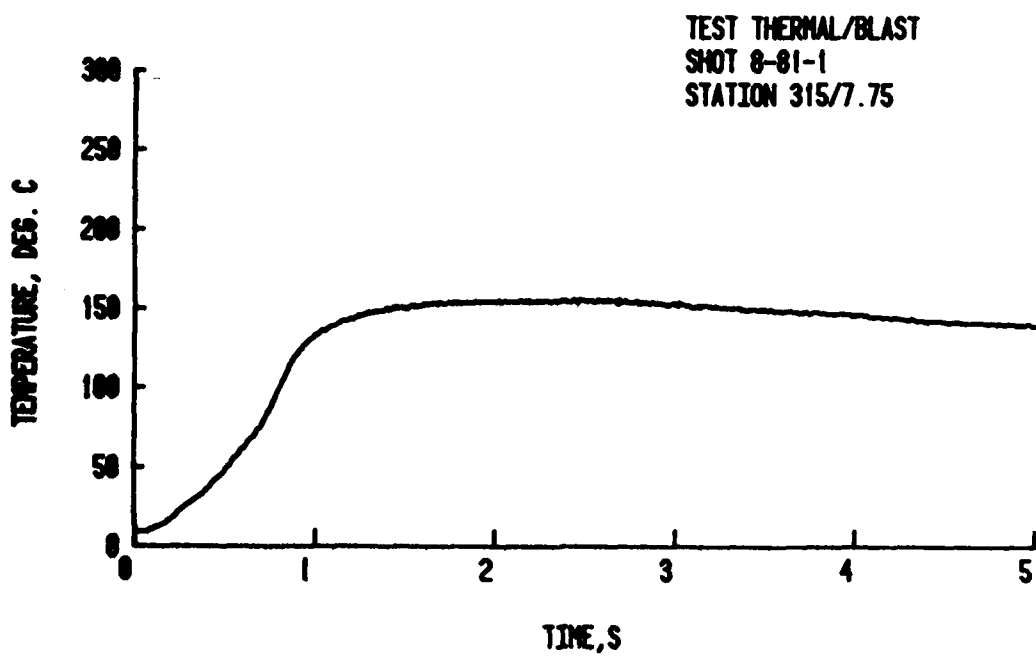
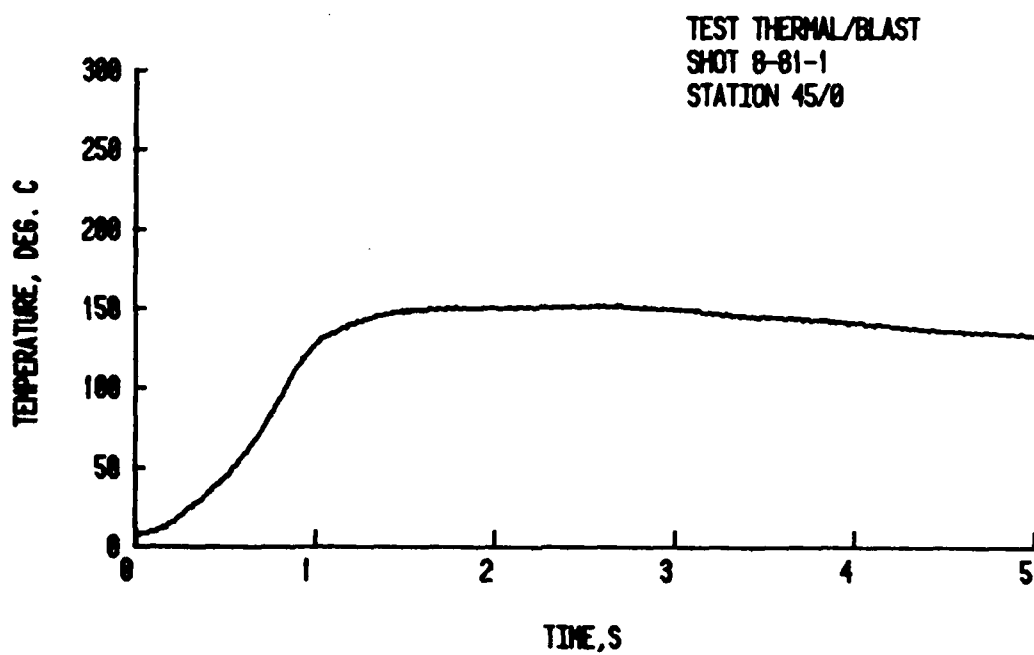


Figure 36. Temperature Histories at 45° and the Center and at 315° and 19.69 cm below the Center.

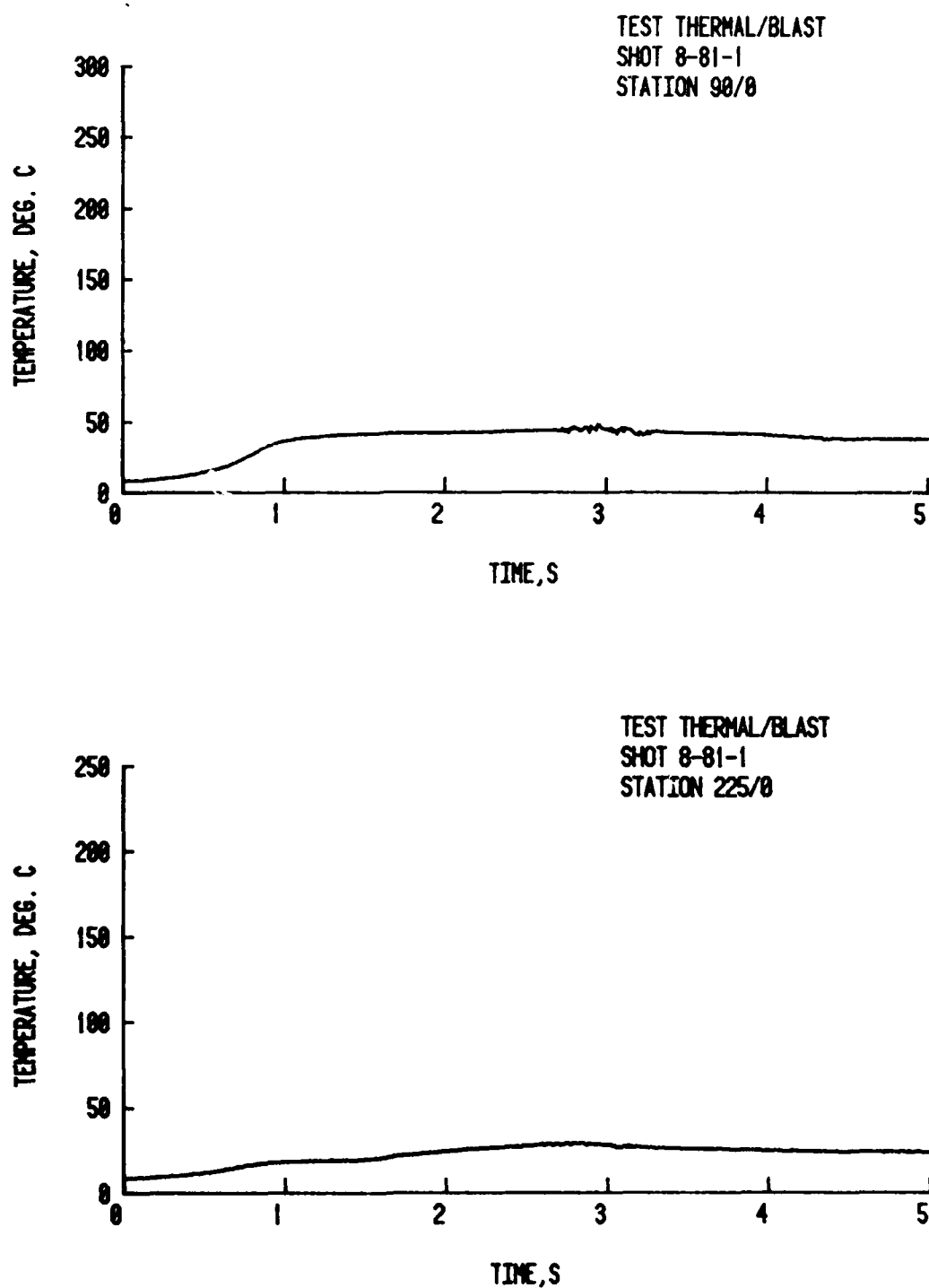


Figure 37. Temperature Histories at 90° and the Center and at 225° and the Center.

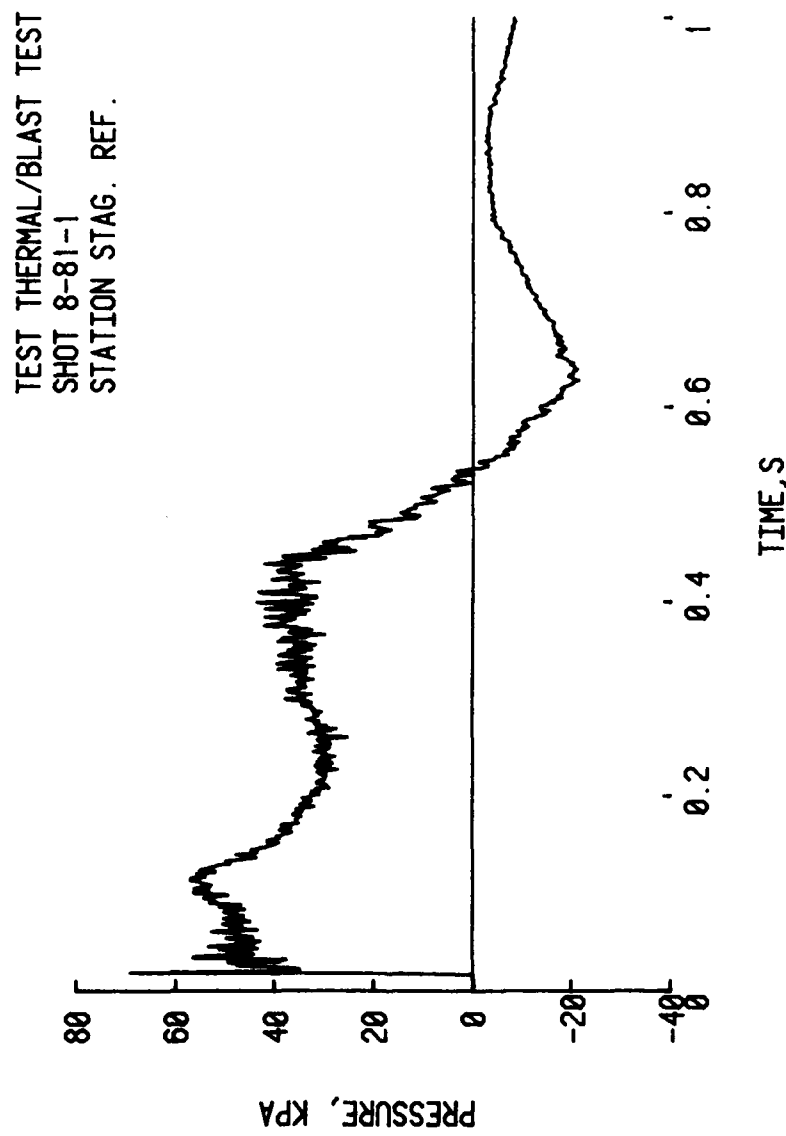


Figure 38. Stagnation Overpressure History in Shot 8-81-1.

anomalous "spike" at shock arrival. The "spike" is of unknown origin but is characteristic of Bytrex "free field" measurement in combined thermal/blast simulations.

The initial "spike" can be seen at the start of the pressure history in Figure 38. The "spike" is approximately 2 ms wide and has a maximum value of 77 kPa. The "spike" is followed by the arrival of the rarefaction wave from the front of the hot gas region. Behind the rarefaction is a period of approximately constant overpressure. The static overpressure behind the rarefaction wave was approximately 30 kPa and the stagnation overpressure was 49 kPa. The arrival of compression wave from the downstream side of the hot gas region began a period of increasing overpressure which lasted until the arrival of the rarefaction from the open end of the simulator. The remainder of the history is similar to the history in shot 8-80-7.

The absolute pressure in the compression section used to produce the shock was 236.29 kPa. The absolute pressure in the expansion section was 101.38 kPa. The temperature in the compression section was 11.9 C°. The temperature in the expansion section was 10.0 C°.

Figures 39 through 43 show the blast loading histories recorded by the gages on the upper bearing mount. The "smearing" of the shock front produced by the uses of the thermal source is very apparent. The pressure rise is very slow and there is no evidence of shock reflection from the target surface. In addition, overpressure levels recorded in shot 8-81-1 were below those in 8-80-7. Approximately the same ratio of compression section pressure to expansion section pressure was used in both shots; therefore, the reduced level must be due to the effects of the thermal source.

Figure 44 shows the target deformation resulting from the combined thermal/blast loading simulation. The format used is the same as that used in Figures 13 and 25. The figures show that the deformation is different in both magnitude and character from either the thermal or blast loading tests. The deflections are larger and extend over a greater area than either the tests involving only thermal or blast loading. The buckling pattern at the ends is similar to that found in the thermal test but the large deformation about the center of the loaded face was not present in either of the other tests. The maximum deflection measured was 7.97 mm or 5.2% of the target radius. The maximum deflection occurred near the center of the loaded face.

Figure 45 shows the deflection at the longitudinal center section. The format is the same as that used in Figures 14, 26 and 27. The deformations were larger than the deformations in either the thermal or blast loading test. The deflections are also larger than a linear combination of the deflection measured in thermal and blast tests. The deflections are asymmetric but less so than the blast loading test, shot 8-80-7.

Figures 46 through 50 show the strain histories in shot 8-81-1 during the first five seconds after the start of the thermal source burn. The format used is the same as that used in Figures 28 through 32. The solid lines are again the recorded strain histories and the dashed lines are the strain histories

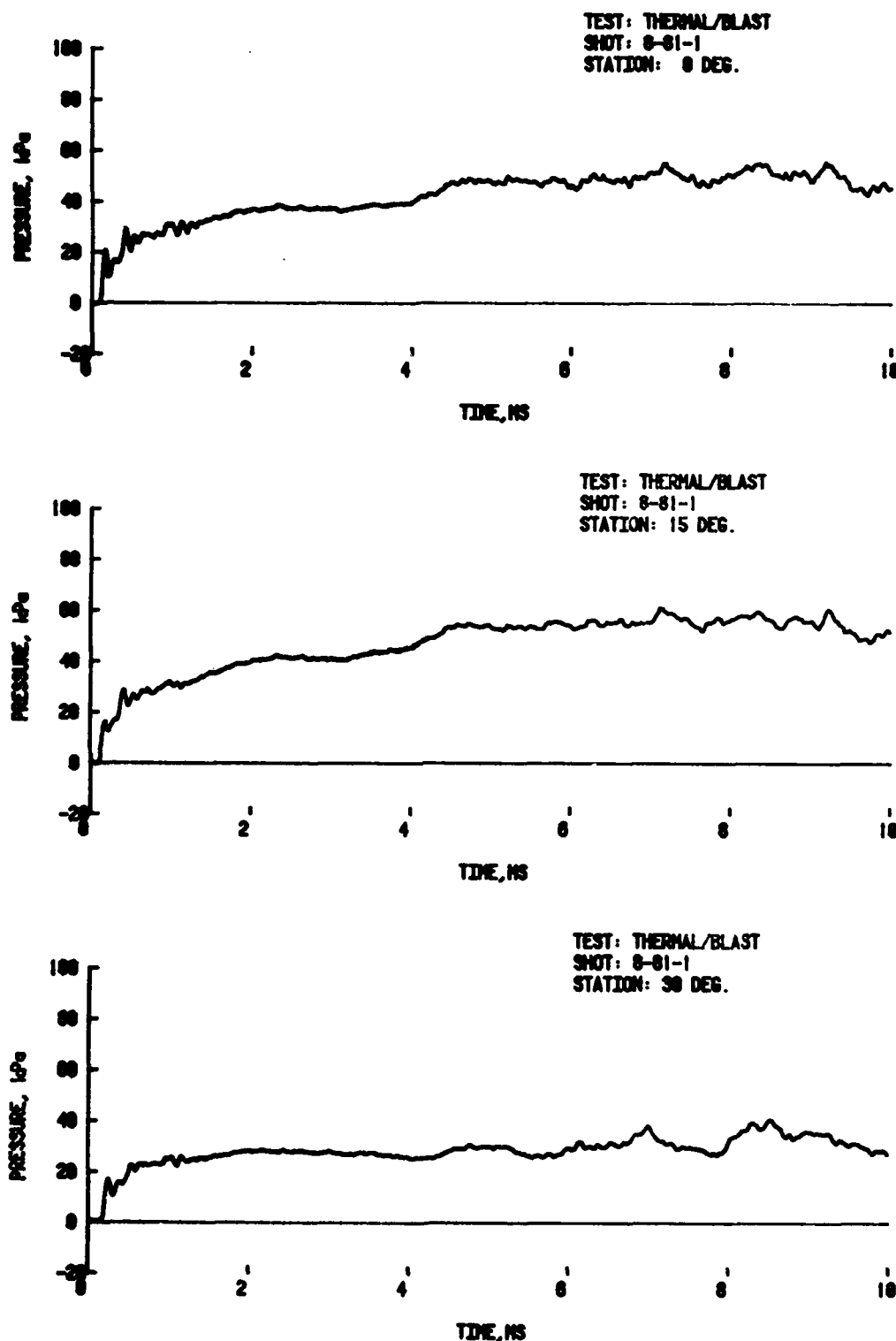


Figure 39. Diffraction Overpressure History at 0° , 15° , and 30° in Shot 8-81-1.

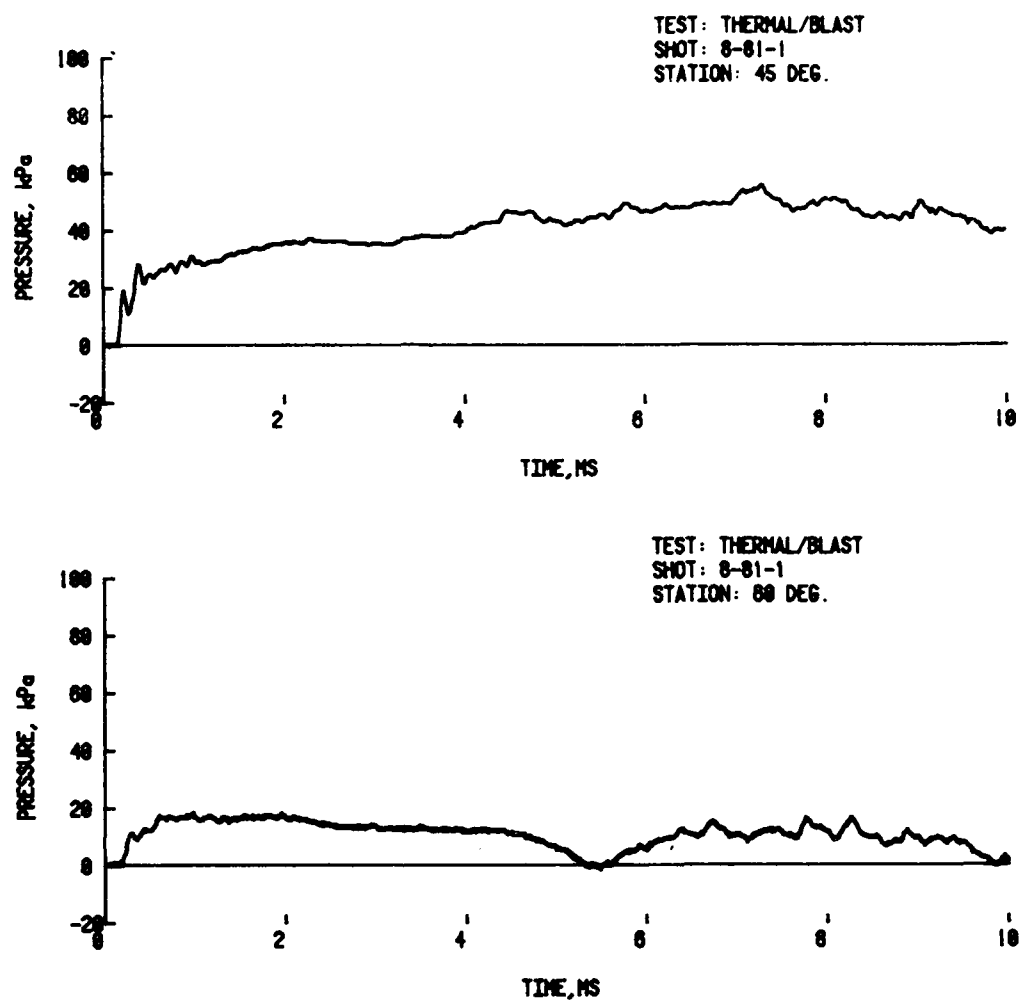


Figure 40. Diffraction Overpressure Histories at 45° and 60° in Shot 8-81-1.

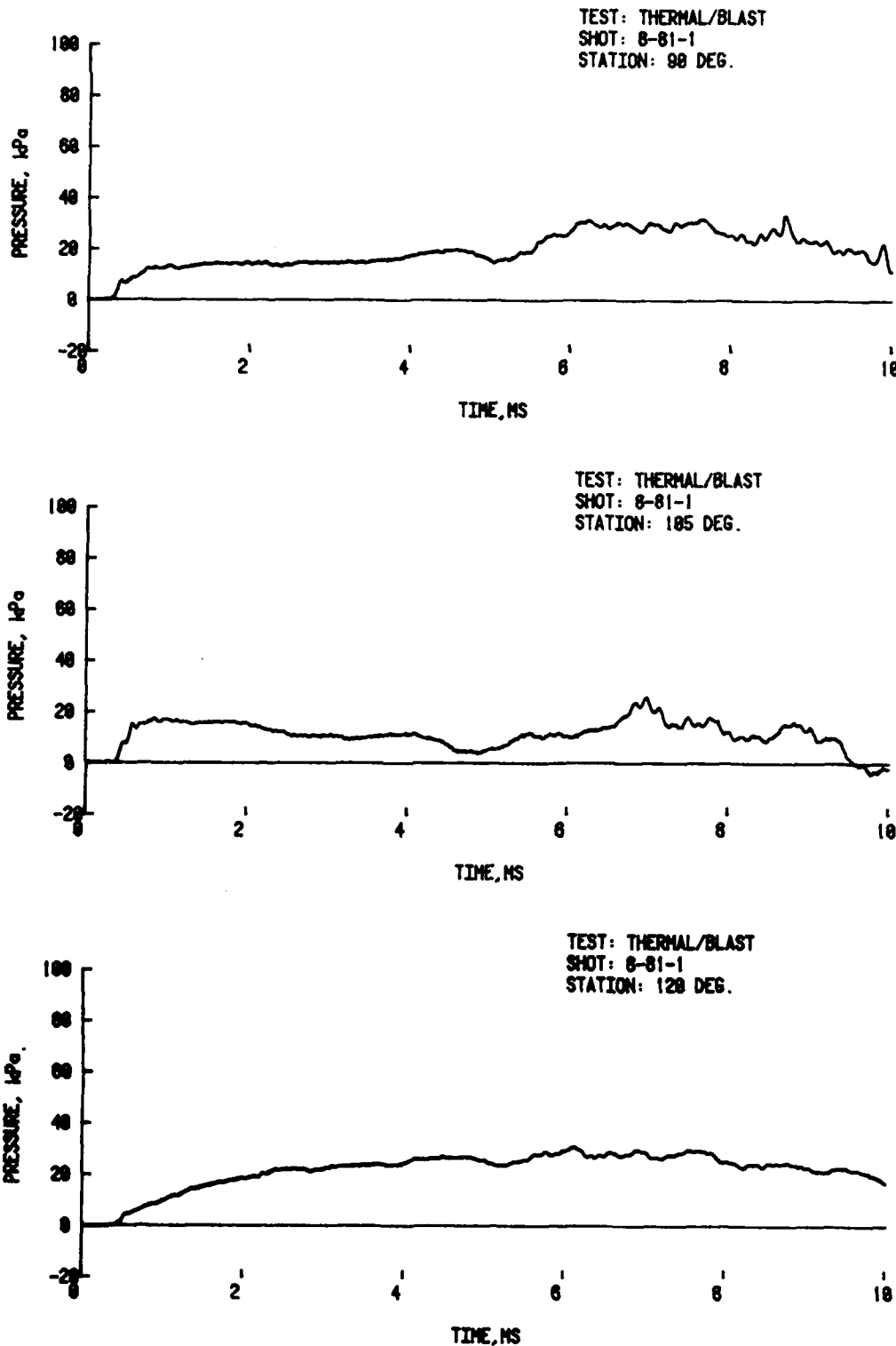


Figure 41. Diffraction Overpressure Histories at 90° , 105° and 120° in Shot 8-81-1.

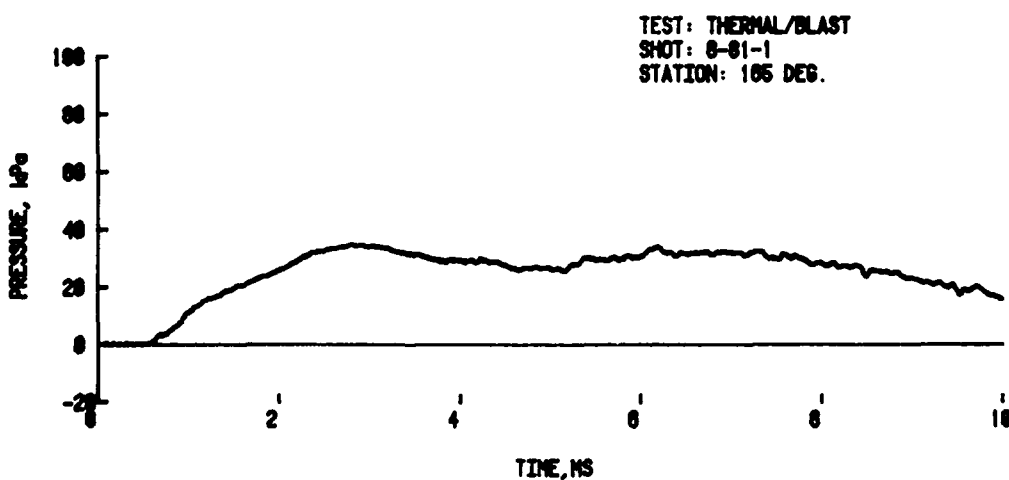
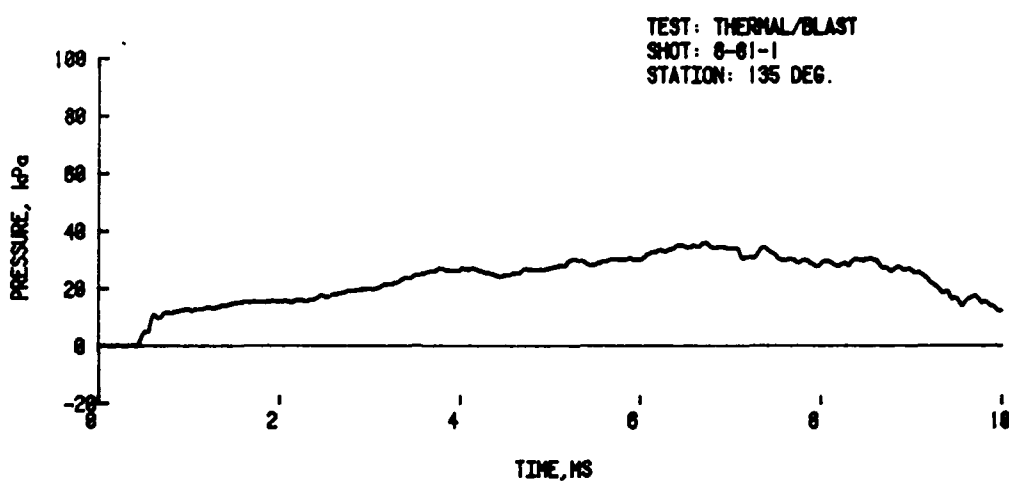


Figure 42. Diffraction Overpressure Histories at 135° and 165° in Shot 8-81-1.

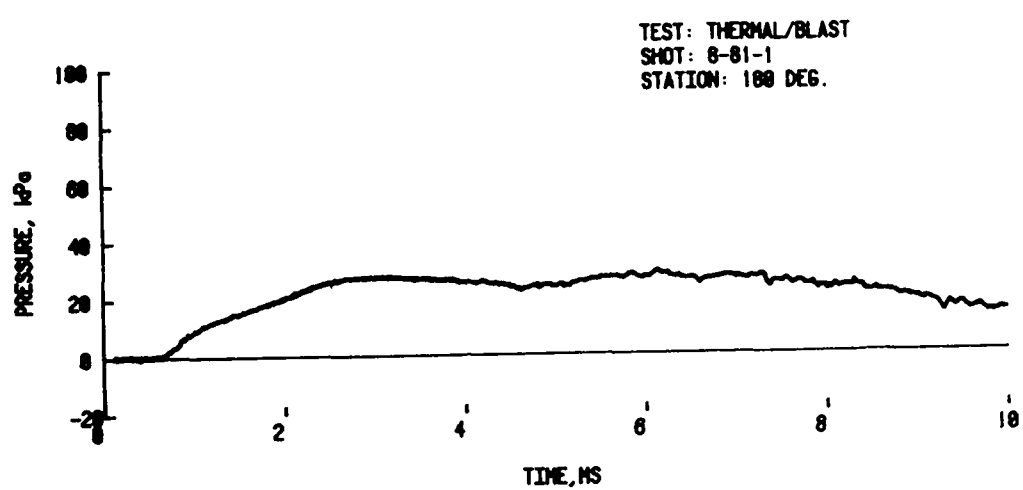
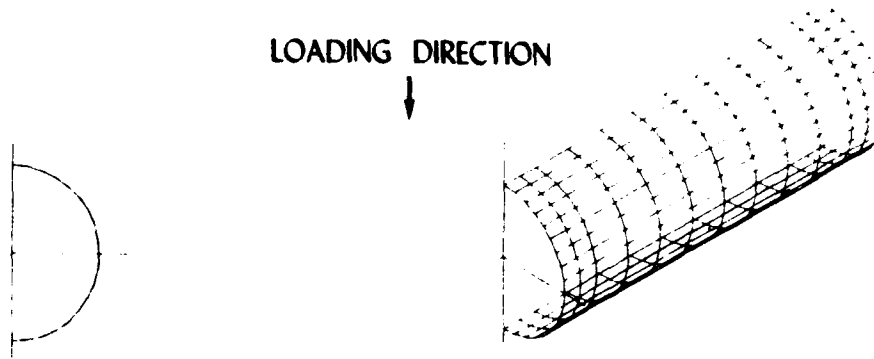
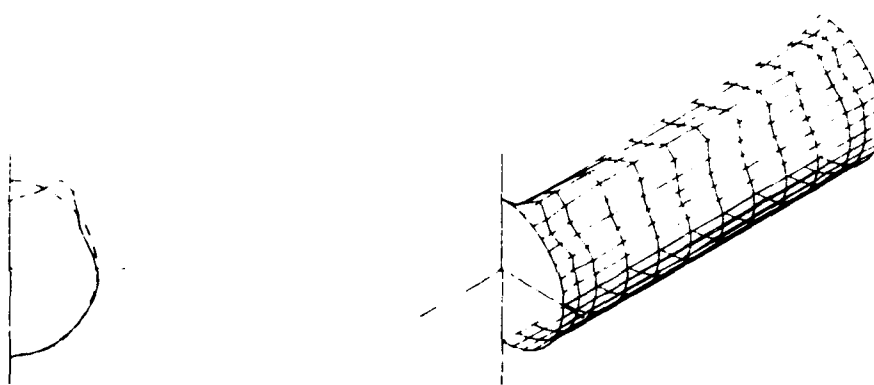


Figure 43. Diffraction Overpressure History at 180° in Shot 8-81-1.

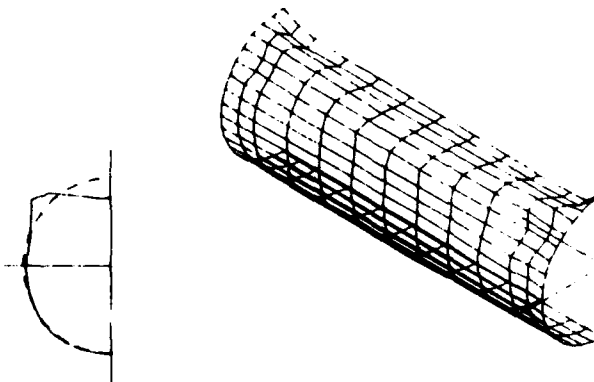
DEFLECTION MAGNIFICATION 5X



PRE-TEST TARGET SHAPE - RIGHT HALF

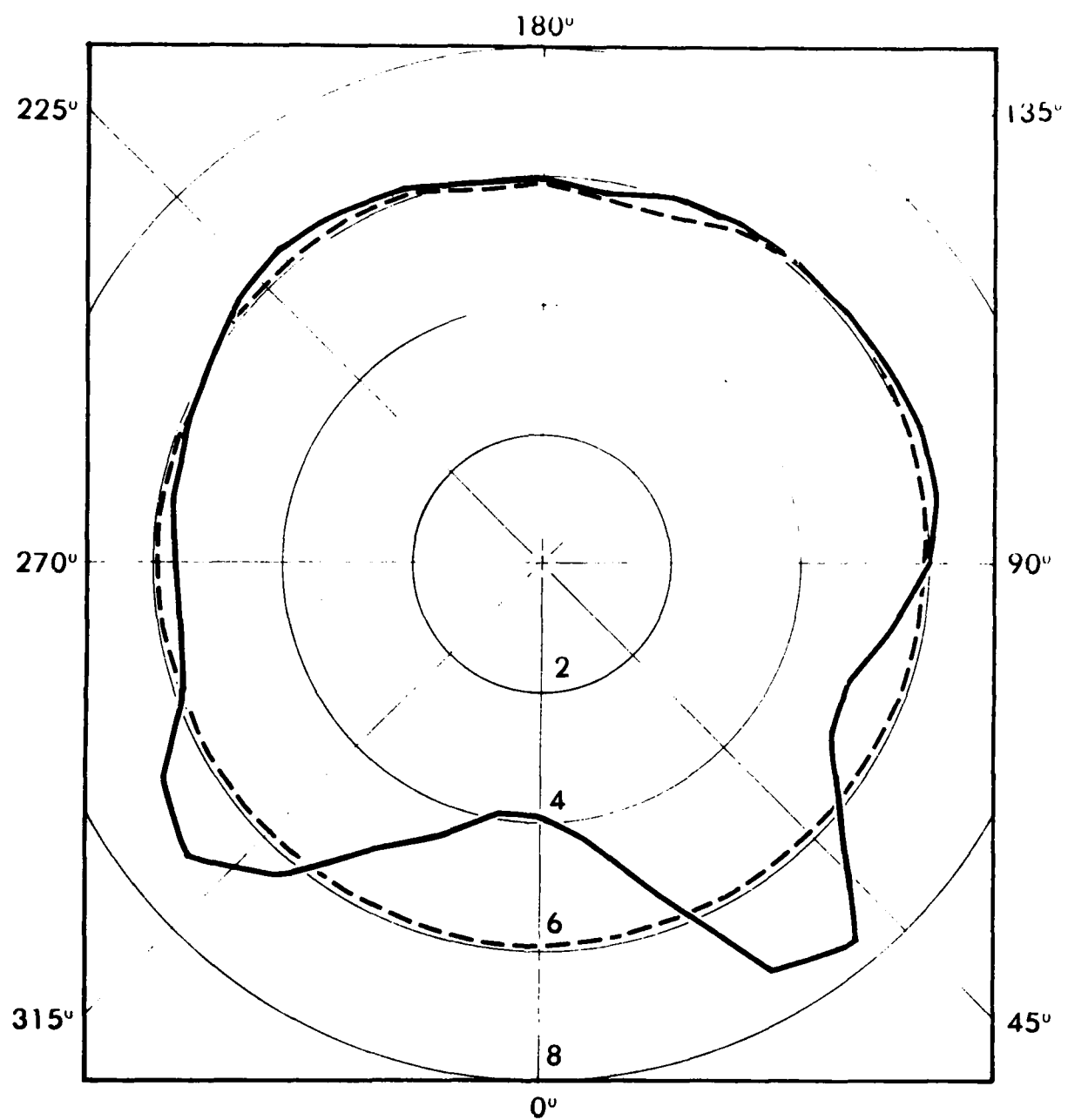


POST-TEST TARGET SHAPE - RIGHT HALF



POST-TEST TARGET SHAPE - LEFT HALF

Figure 44. Three-Dimensional Plots of Target Deformation in Shot 8-81-1.



**DEFLECTION X8
CENTER CROSS SECTION**

----- PRE-SHOT SHAPE
——— POST-SHOT SHAPE

Figure 45. Deformation of the Center Cross Section of the Target in Shot 8-81-1.

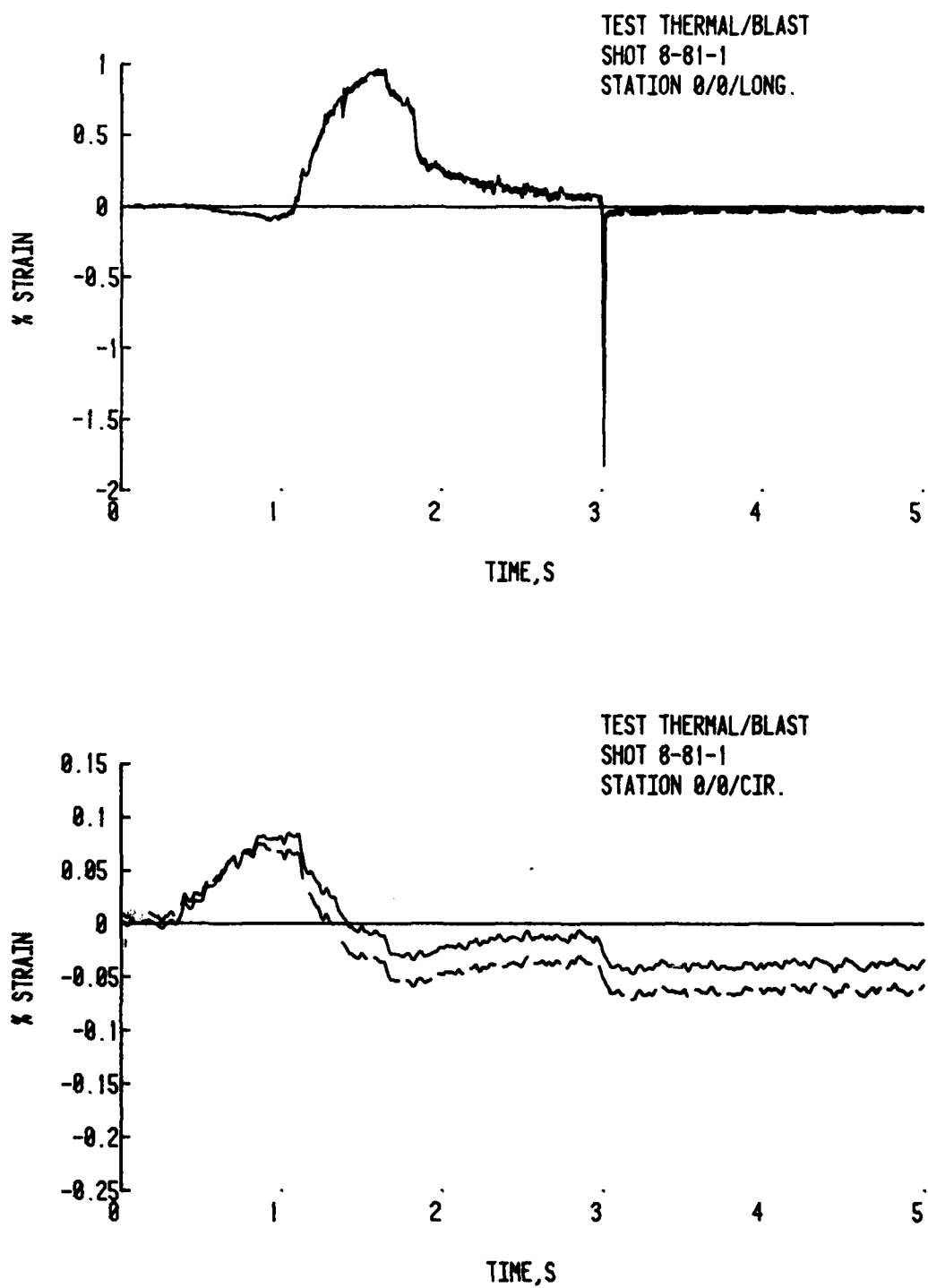


Figure 46. Five-Second Longitudinal and Circumferential Strain Histories at 0° and the Longitudinal Center.

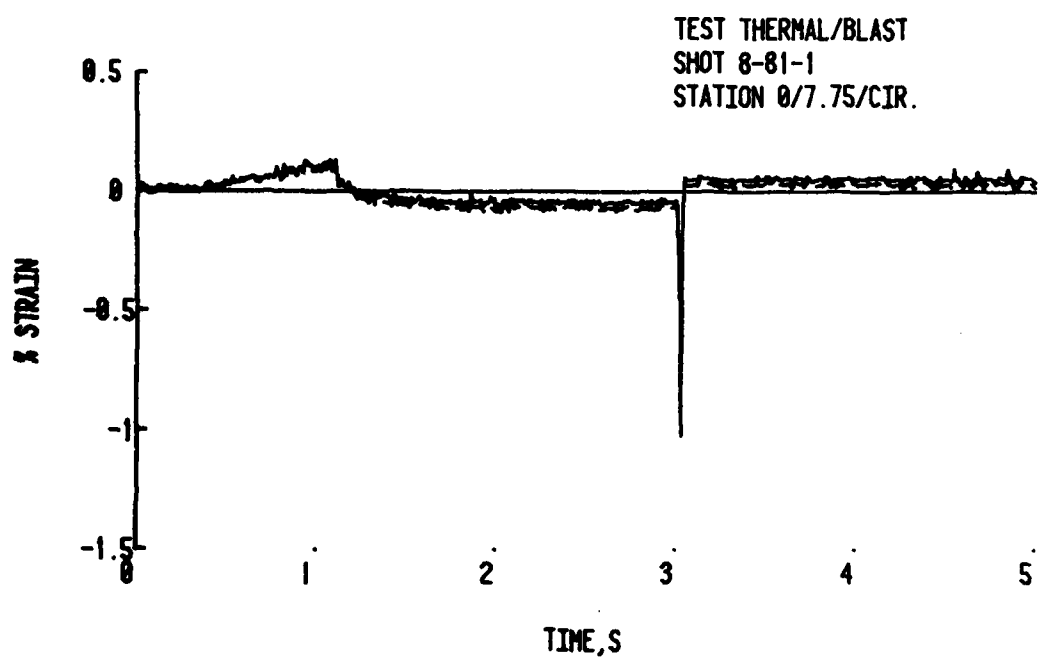
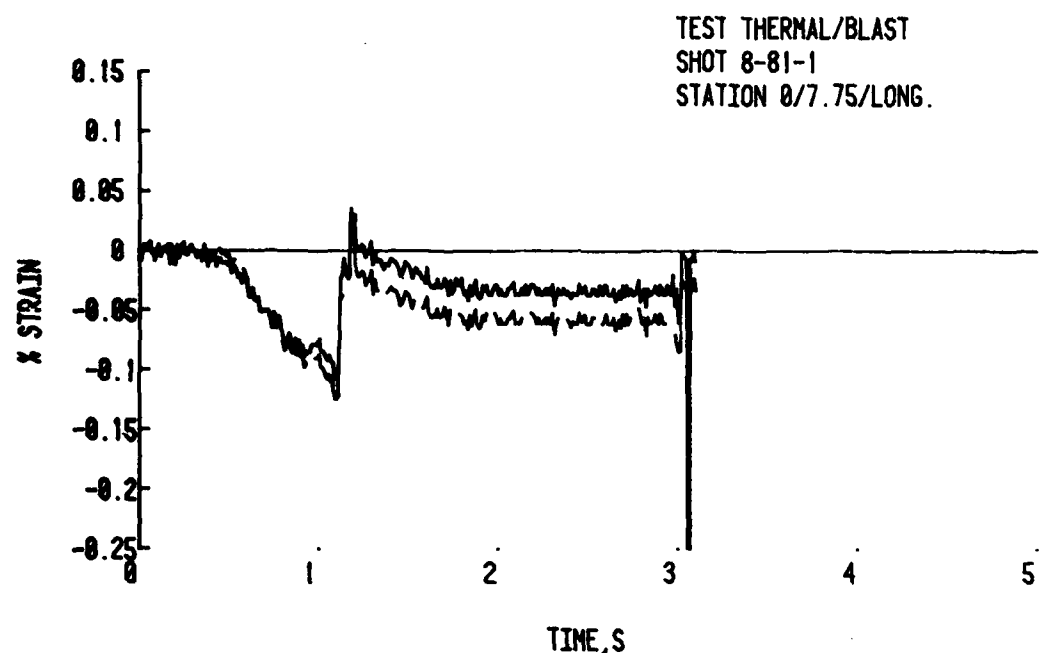


Figure 47. Five-Second Longitudinal and Circumferential Strain Histories at 0° and 19.69 cm below the Longitudinal Center.

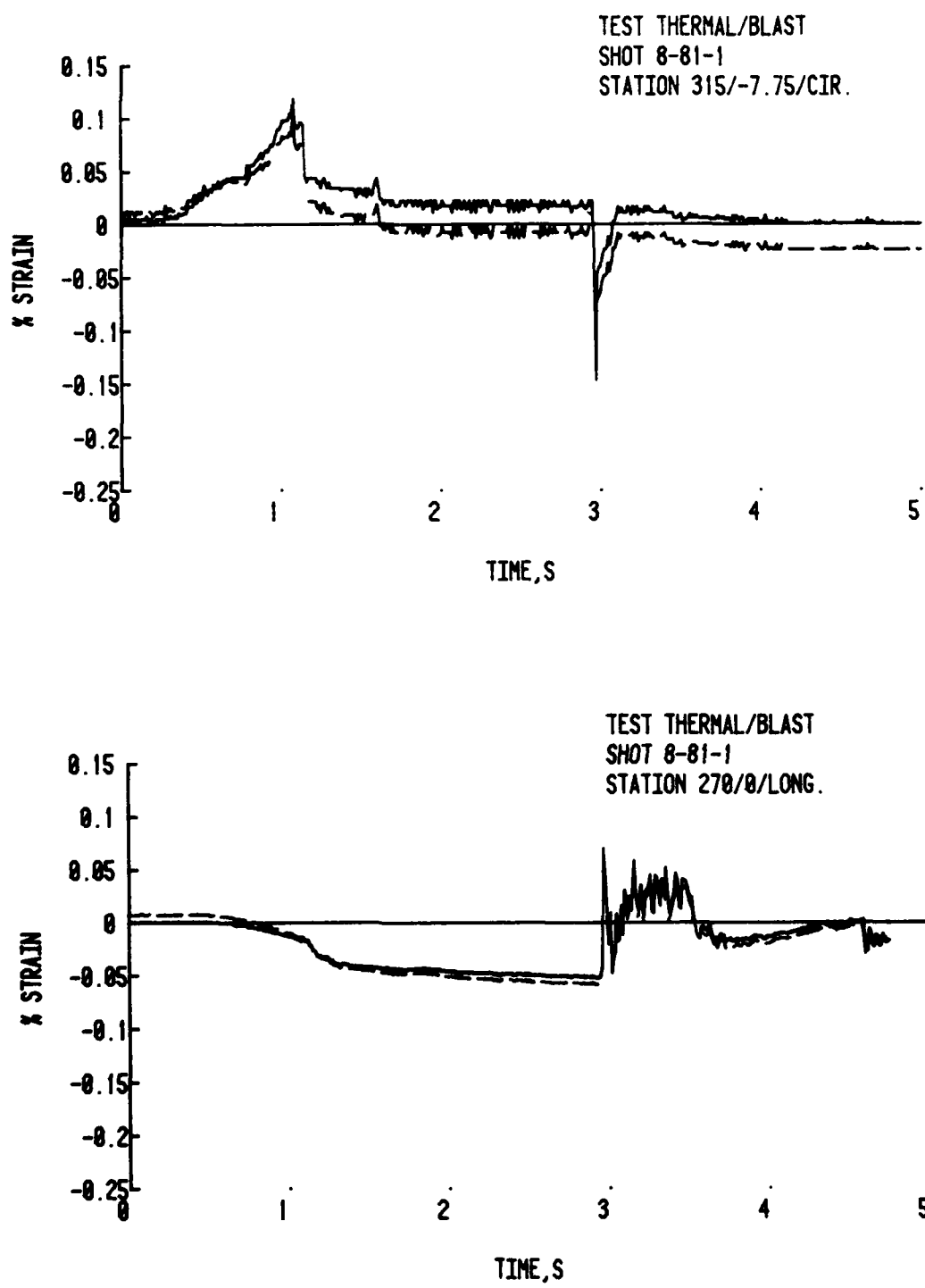


Figure 48. Five-Second Circumferential Strain History at 315° and 19.69 cm above the Longitudinal Center and Longitudinal Strain History at 270° and the Longitudinal Center.

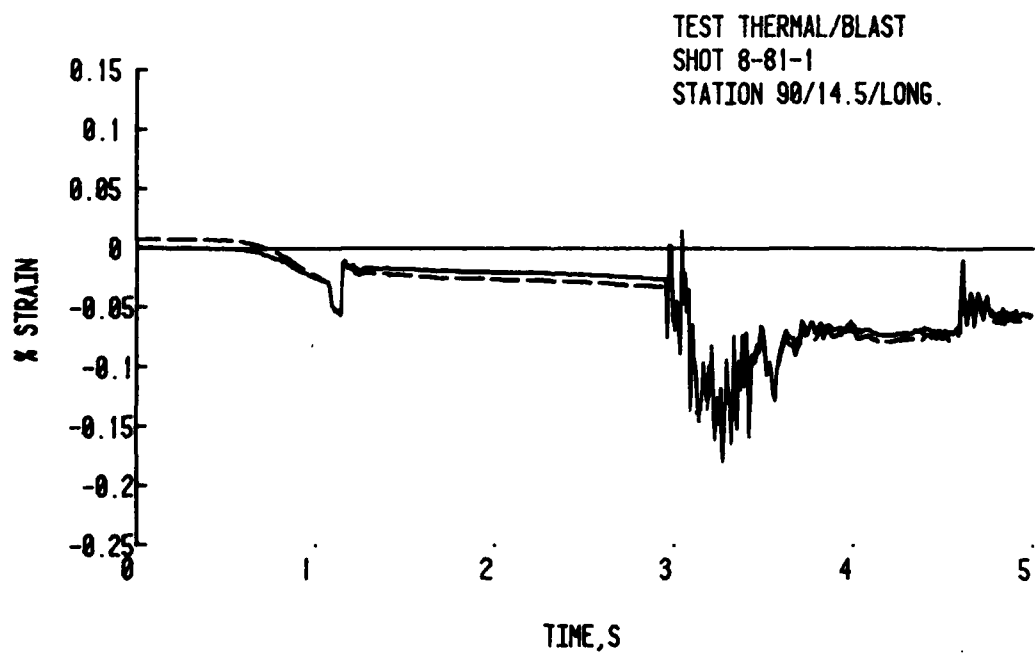


Figure 49. Five-Second Longitudinal Strain History at 90° and 37.47 cm below the Longitudinal Center.

TEST THERMAL/BLAST
SHOT 8-81-1
STATION 225/0/CIR.

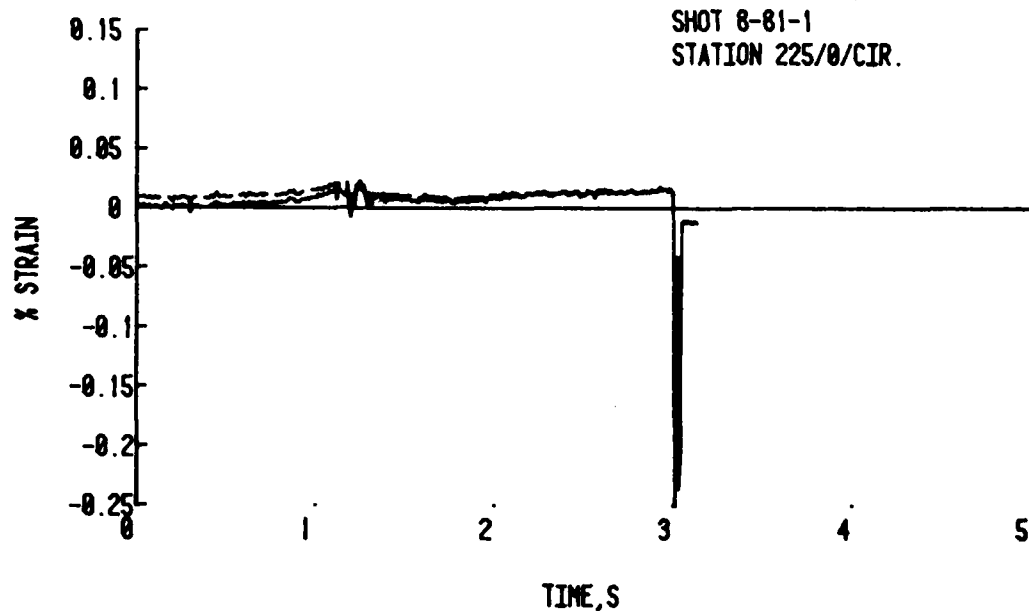


Figure 50. Five-Second Circumferential Strain History at 225° and the Longitudinal Center.

after correcting for thermal effects on the strain gages. As in Figures 28 through 32 the slow digitizing rate has "filtered out" the higher frequency signal in the records.

The gage measuring circumferential strain at 270° and the longitudinal centerline failed early in the test and the history is therefore not shown. The gage measuring circumferential strain at 225° and the longitudinal center line debonded shortly after shock arrival; therefore, the plot of the history was cut short.

Figures 46 through 50 initially show the same type of strain history as Figures 27 through 31 from shot 8-80-10. The magnitudes, and in one case the direction, are different but the same strain "jump" during thermal loading is found in both tests. The "jump" again occurs at approximately one second into the thermal burn and can be interpreted as a result of thermal buckling.

The effect of shock arrival can be seen at approximately three seconds after the start of the thermal source burn. The response of the target cylinder to the blast loading is much faster than the responses to thermal loading and as a result little can be seen in these five-second plots.

Figures 51 through 55 show the first 10 ms of the strain history after shock arrival. The figures are meant for comparison with Figures 15 through 19. To make comparison easier, the residual thermal strains present at shock arrival have been subtracted out before plotting. As a result of the subtraction, the plots start at zero strain. These plots are meant to represent the strain induced by the blast loading part of the loading history.

The strain histories show that the target response occurred later after shock arrival in this shot than in shot 8-80-7. The slow response is probably due to the slow pressure rise in the blast wave caused by the thermal source burn. The strain levels reached were comparable to those in the blast loading test but occurred much later. Unlike shot 8-80-7 there does not appear to be any obvious dominant frequency in the strain record. The lack of a dominant single frequency may be due to the thermal deformation of the target before shock arrival.

The strain records are again hard to relate from station to station due to the asymmetry in the response of the target cylinder. The differences in the amount of asymmetry in the three types of structural tests also make comparison between tests difficult. The records are presented mainly to serve as basic for qualitative comparison.

IV. ANALYSIS

As a check on the results of both the structural test and the pre-test computer calculations, a few simple analytical calculations of the thermal and overpressure loads needed to buckle the target cylinder were performed. A number of simplifying assumptions had to be used in order to reduce the problem to a tractable form. Despite the simplifications, the solutions to the analytical problems should indicate whether the results of the structural thermal and blast loading tests were reasonable.

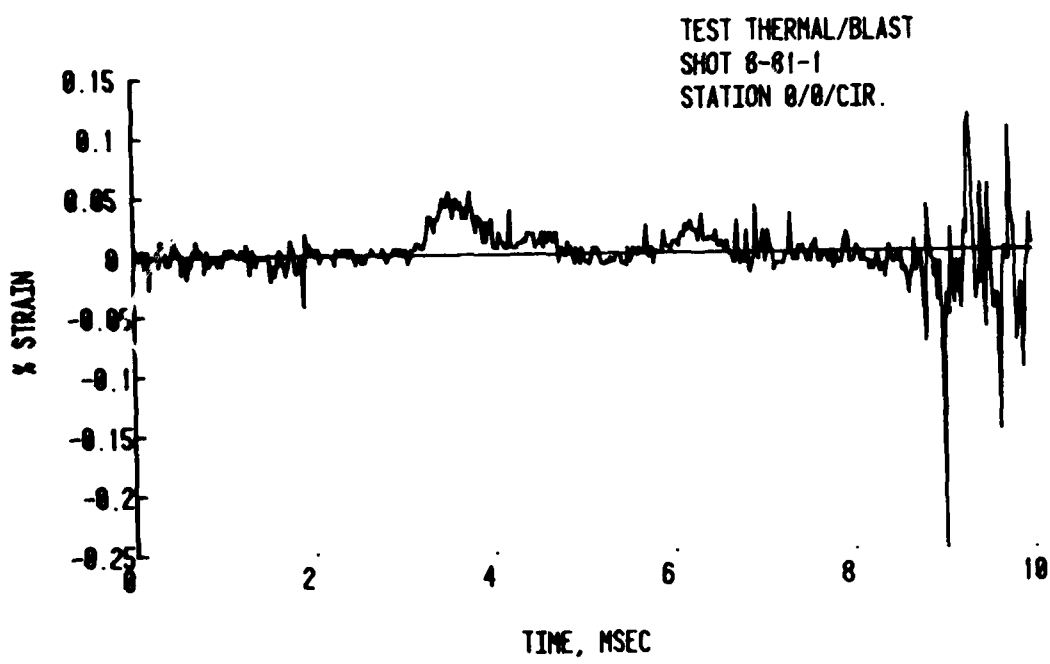
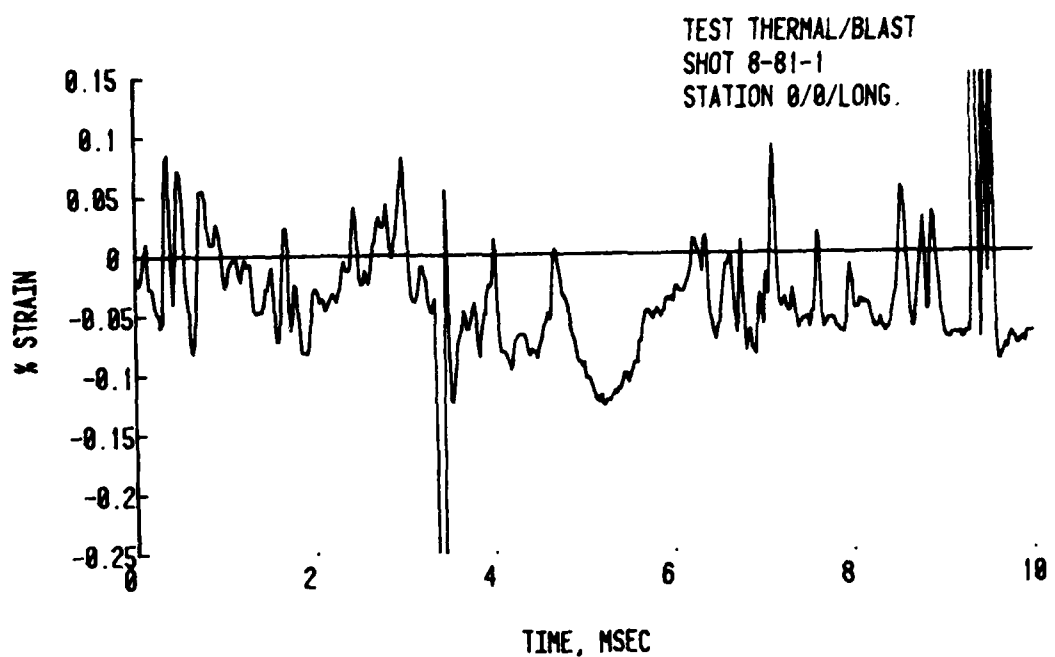


Figure 51. Ten-Millisecond Longitudinal Strain Histories at 0° and the Longitudinal Center.

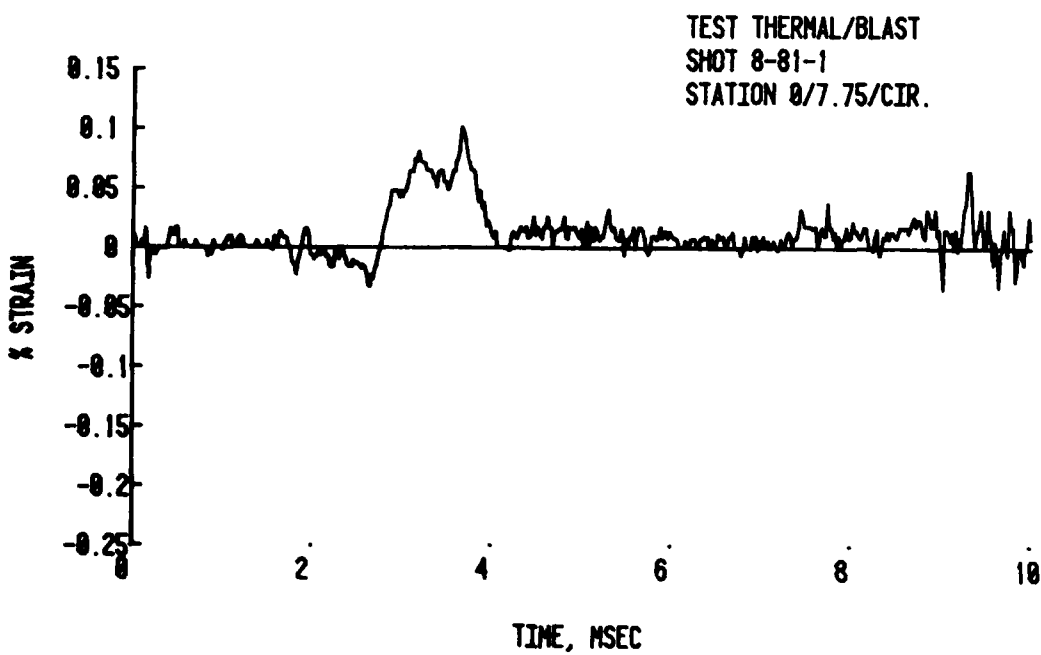
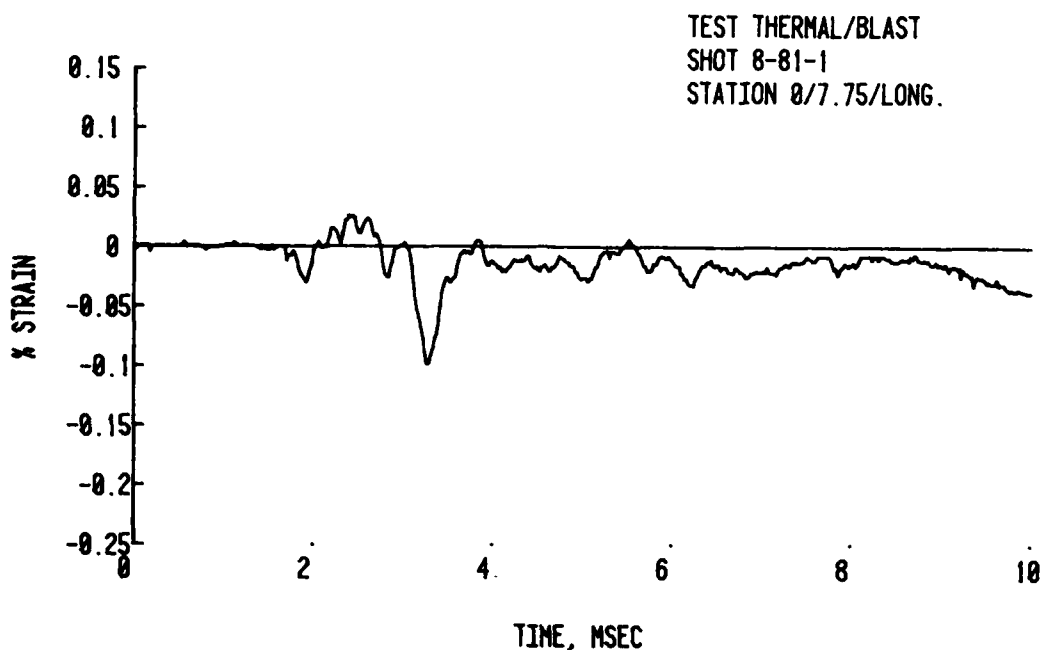


Figure 52. Ten-Millisecond Longitudinal and Circumferential Strain Histories at 0° and 19.69 cm below the Longitudinal Center.

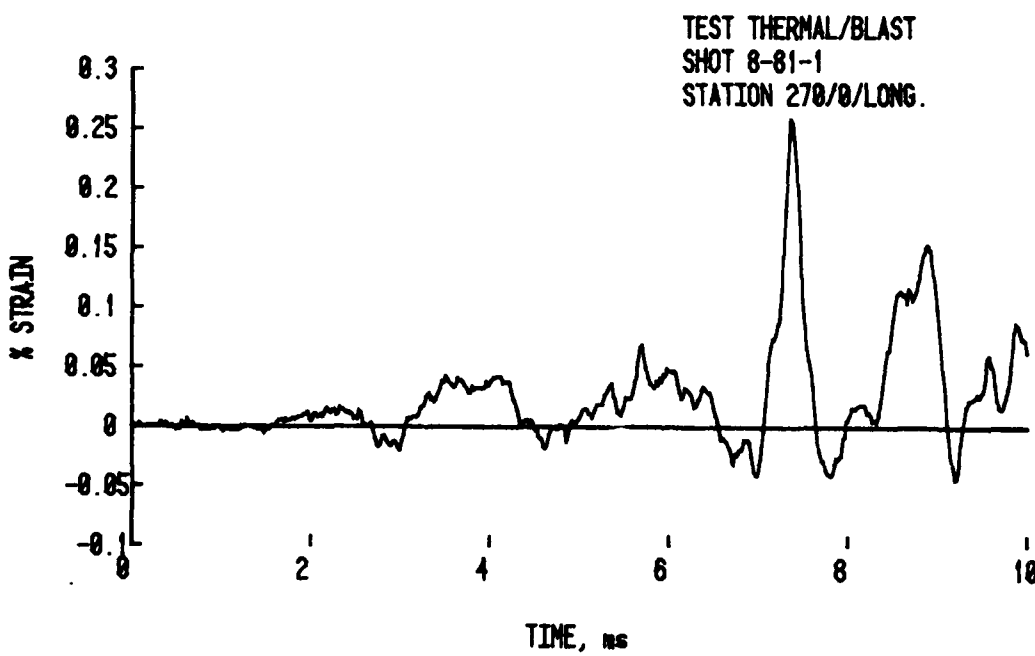
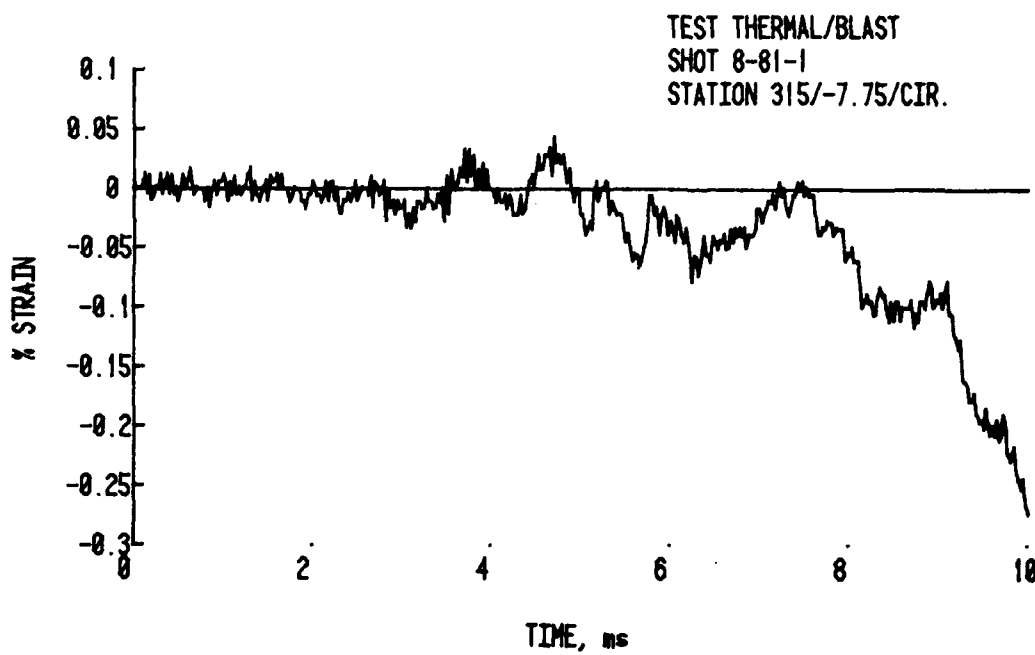


Figure 53. Ten-Millisecond Circumferential Strain History at 315° and 19.69 cm above the Longitudinal Center and Longitudinal Strain History at 270° and the Longitudinal Center.

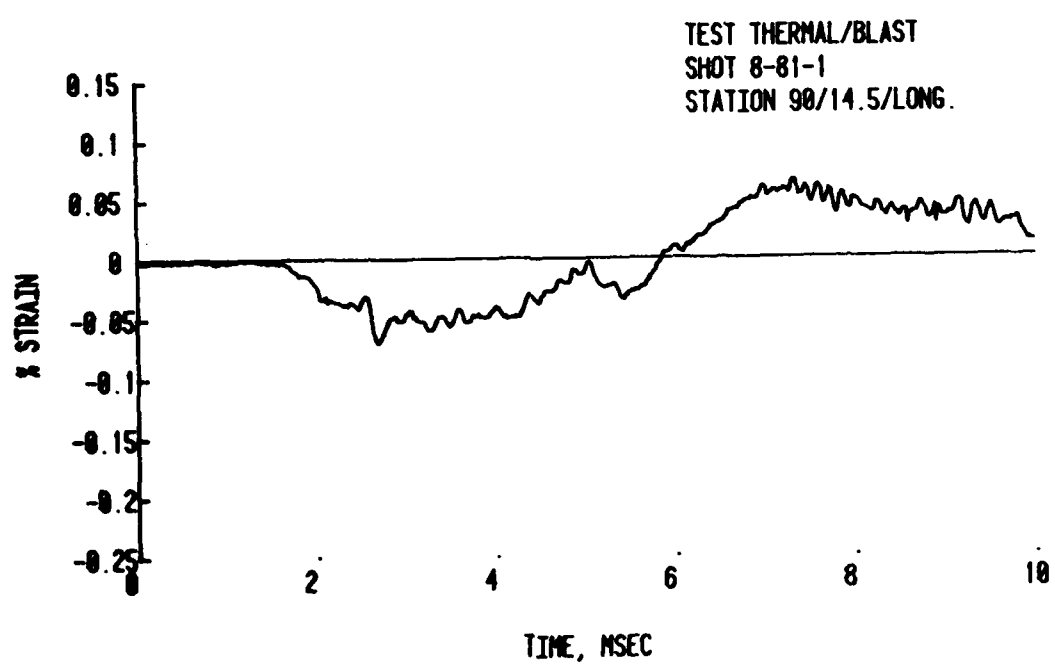


Figure 54. Ten-Millisecond Longitudinal Strain History at 90° and 37.47 cm below the Longitudinal Center.

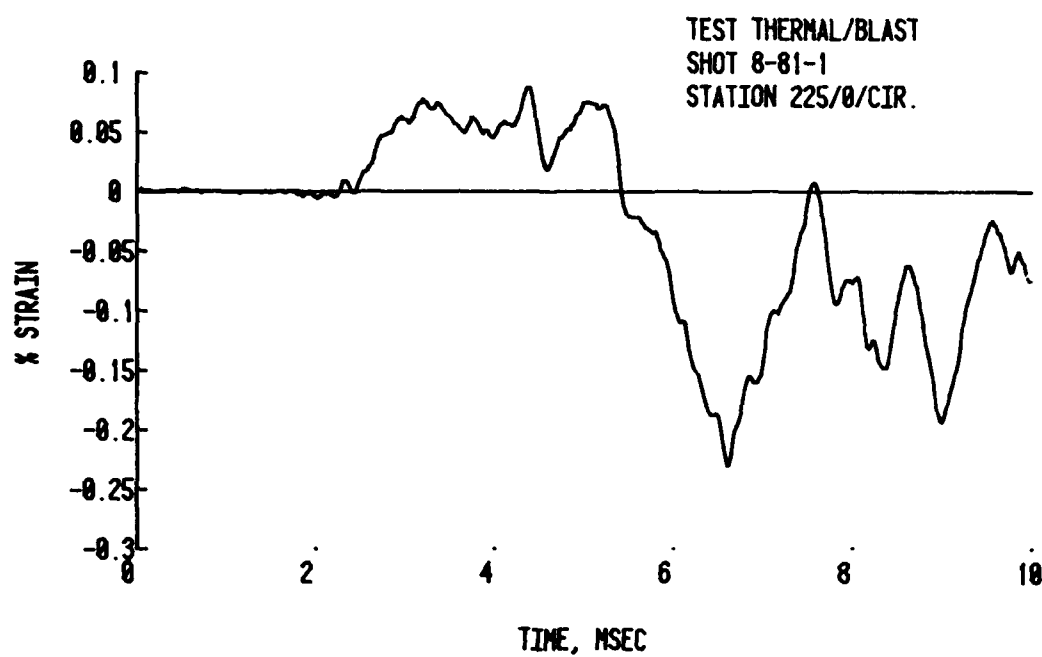


Figure 55. Ten-Millisecond Circumferential Strain History at 225° and the Longitudinal Center.

The overpressure generated in the blast loading test was compared with the critical buckling load for a cylinder under uniform, external circumferential pressure. The ends were assumed to be simply supported in order to simplify the calculations. In the test the ends of target cylinder were clamped. Assuming simply supported ends should underestimate the buckling load. In the calculations the loading was assumed to be constant or static. Experimental results on the buckling of hollow cylinders by decaying blast wave are presented in References 7 and 8. The results in Reference 7 indicate that for the peak overpressure and overpressure impulse used in the structural tests a static calculation of the buckling load should provide a reasonable approximation.

Two different formulations were used in calculating the critical buckling load. The first was taken from Reference 9. The formula for the critical buckling load (P_{cr}) was given as

$$P_{cr} = \frac{0.926}{(R/t_w)^{5/2}} \frac{\sqrt{\gamma E}}{(L/R)} \quad (2)$$

In Equation 2, E is Youngs' modulus, R is the radius of the cylinder, L is the length of the cylinder and t_w is the wall thickness. γ is known as the critical length and was assumed to be equal to 0.9. The critical buckling load calculated using (Eq. 2) was 40.47 kPa.

A second calculation was based on Reference 10. Using the plot on page 451 of Reference 10 the number of nodes expected in the buckling pattern was determined to be between 4 and 5. Using the number of nodes (n) in the following equation the buckling load was calculated for n = 4 and n = 5

$$P_{cr} = \frac{Et_w}{(1-\gamma^2)R} \left\{ \frac{(1-\gamma^2)}{(n^2-1)(1+\alpha)^2} + \frac{t_w}{12R} \left[(n^2-1) + \frac{2n^2-1-\gamma}{1+\alpha} \right] \right\} \quad (3)$$

⁷ H. E. Lindberg, D. L. Anderson, R. D. Firth and L. V. Parker, "Response of Reentry Vehicle-Type Shells to Blast Loads," Stanford Research Institute for Lockheed Missiles and Space Company, Sunnyvale, CA, P.O. No. 24-14517, Sept. 30, 1965.

⁸ J. K. Vinson, Structural Mechanics: The Behavior of Plates and Shells, Wiley-Interscience, John Wiley and Son, Inc., New York, 1974.

⁹ S. P. Timoshenko and J. M. Gere, Theory of Elastic Stability, 2 ed McGraw-Hill Book Company, New York, 1961.

¹⁰ W. J. Schuman, "The Response of Cylindrical Shells to External Blast Loading, Part II," Memorandum Report No. 1560, Ballistic Research Laboratory, Aberdeen Proving Ground, MD, May 1964 (AD 444335).

In Equation 3 $\alpha = (n^2 L^2) / \pi^2 R^2$ and all other variables are defined in the same way as in Equation 2. For $n = 5$, the buckling load was calculated as 49.24 kPa. For $n = 4$ the buckling load was calculated as 42.22 kPa.

The results of the test were in reasonable agreement with the calculations. In both blast loading shots, the overpressure loading exceeded the buckling load only on the front of the target. In shot 8-80-6 the overpressure exceeded the buckling load in only a small area and only briefly in the diffraction part of the loading. There was very little deformation in shot 8-80-6. In shot 8-80-7 the overpressure exceeded the buckling loading on the front of the cylinder in both the diffraction phase and the following drag phase. There was far more permanent deformation on the front of the target in shot 8-80-7 than in 8-80-6. In neither shot did the overpressure on the rear of the target exceed the calculated buckling loads and there was no permanent deformation on the rear of the targets.

A comparison of the buckling mode shape predicted by Reference 9 and the deformation pattern observed in shot 8-80-7 again shows reasonable agreement. Buckling modes for the cylinder of 4 or 5 lobes results in angles between maximum deflections of 90° and 72° , respectively. The angular distance between deflection maxima measured in shot 8-80-7 was approximately 73° . The deflection in shot 8-80-6 was so small that no clear deflection pattern could be discerned.

Comparisons with the empirical models developed from experimental results were also made. Reference 7 contains a model based on target diameter, target length, wall thickness, peak incident overpressure and overpressure impulse. A calculation based on Reference 7 gives a critical buckling pressure of 42.4 kPa. A model developed in Reference 10 is based on target diameter, target length, wall thickness and explosive charge weight. The charge weight used in the calculation was chosen so that the impulse matched the experimental impulse at the 42 kPa overpressure level. The weight used was 5083 tons of Pentolite. The results of the calculations gave a critical buckling load of 59.6 kPa. Both references assume a spherically expanding shock wave with continuously decaying overpressure behind the shock. Because the pressure history is different from that in the simulator the comparison is not exact.

The thermal loads generated in the thermal loading tests were compared with the critical buckling load for a cylinder under uniform axial compression. The ends were assumed to be unconstrained radially. The stress in the cylinder was calculated by assuming that the stress was uniaxial in the axial direction until buckling occurred. The stress was assumed to be equal to the stress that would produce an axial strain equal in magnitude but opposite in direction to the strain induced by free thermal expansion. The thermal stress (σ_T) was calculated using Equation 4.

$$\sigma_T = E \cdot C_T \cdot \Delta T \quad (4)$$

In Equation 4, E is Youngs modulus, C_T is the coefficient of thermal equation and ΔT is the change in temperature. The buckling load in the cylinder was taken from Reference 11. The formula for the buckling load used was Equation 5.

$$\sigma_T = \frac{E \cdot t_w}{R[3(1-\gamma^2)]^{1/2}} \quad (5)$$

In Equation 5, E is again Youngs modulus, R is the target radius, t_w is the wall thickness and r is Poisson ratio. Combining Equations 3 and 4,

$$\Delta T = \frac{t_w}{C_T \cdot R[3(1-\gamma^2)]^{1/2}} \quad (6)$$

In Equation 6, ΔT is how the temperature increase is necessary to buckle the target. Solving Equation 6 for ΔT yields a temperature increase of 147.5 C° .

The temperature increase which caused the target to buckle in the structural test was taken as the accumulated temperature increase at the center of the heated face of the target when the target buckled. The time at which the target buckled was determined from the strain histories. For the thermal loading test, shot 8-80-10, the temperature increase that occurred before buckling was 127 C° . For the combined loading test, shot 8-81-1, the temperature increase was 128 C° . Experimentally measured axially buckling loads have been found to lie between 40% and 60% of the theoretical value.¹² The measured values from shot 8-80-10 and 8-81-1 are 86% and 87% of the theoretical value, respectively. The values are somewhat higher than expected.

The results of the PETROS 3.5 calculation also compare reasonably well with the analytical calculations. A comparison of the type of damage and the damage level predicted by PETROS and that measured in the structural tests also shows reasonable agreement. Detailed comparison of the target deformation and strain histories, however, showed poor agreement.

The PETROS calculation predicted that there would be little or no permanent deformation of the target for a blast wave with a peak overpressure of 35 kPa. The code also correctly predicted permanent deformation of the target for a 42 kPa overpressure blast wave. In the thermal loading calculations PETROS correctly predicted light structural damage for thermal loads close to those used in the test. Finally, PETROS correctly predicted a synergistic effect for combined thermal/blast loading similar to that used in the structural test.

¹¹ R. J. Roark and W. C. Young, Formulas for Stress and Strain, 5 ed, McGraw-Hill Book Company, New York, 1975.

¹² Y.C. Fung and E.E. Secheler, "Instability of Thin Elastic Shells," Structural Mechanics, Pergamon Press, New York, 1960.

A detailed comparison of the deformation pattern from PETROS and the structural tests shows a poor correlation. The causes of the dissimilarity is thought to be the imperfection in the targets used in the tests. Pre-test measurements revealed imperfections as large as 2.5 mm, although most of the imperfections were smaller. The PETROS calculations were carried out assuming a perfect cylinder. The asymmetric deformation pattern observed in the post-test results appears to follow a pattern similar to the pre-test imperfections, indicating that the imperfection influenced the pattern.

The asymmetry in the buckling pattern observed in the structural test is probably also a factor in the dissimilarity between the strain histories produced by PETROS and those recorded in the structural tests. In the PETROS the strain histories were taken at the location of the deflection maxima. Due to the asymmetry in the deflection pattern, the strain gages used in the structural tests ended up some distance from the maxima making a one-to-one comparison with PETROS difficult.

To reduce run times to a reasonable level and to increase the stability of the calculation, the duration of the thermal loading was decreased by a factor of two thousand. In comparing the PETROS calculation with the experimental strain histories the acceleration of the thermal loading in PETROS must be taken into account.

Another factor affecting the comparison during thermal loading was the difference in the way the stressless free thermal strain was considered in the PETROS calculations and the structural tests. Free thermal strain is the strain that occurs when an unstressed sample undergoes a uniform temperature change. In PETROS the strain produced by thermal expansion or contraction is treated like any other strain. In the structural test the instrument and post-shot data reduction were designed to cancel out the free thermal strains. The large circumferential strains seen in the thermal load and combined loading PETROS calculations were probably caused mainly by thermal expansion.

A factor which affects the comparison of both the deformation pattern and the strain histories was the difference between the blast loading models used in the PETROS 3.5 calculations and the blast loading measured during the structural tests. Figure 56 shows a comparison between the overpressure measurements from shot 8-80-7 and overpressure calculated using the empirical model employed in the PETROS calculation. The solid lines are the maximum overpressures measured in the test and the dashed lines are the late time drag phase overpressure. In addition to the problems of matching the initial and final overpressure, the empirical model did not accurately simulate the overpressure history on the rear of the target. The simple step function used on the rear of the target did not accurately represent the complex histories seen in Figures 9 and 10. Because of the degradation of the blast wave of the thermal source burn the empirical model significantly overestimated the loading on the front of the target during the blast loading phase of the thermal/blast tests.

In the thermal loading calculations, the target temperatures were overestimated. The loading calculations assumed an absorptivity of one. Experimental measurements showed the absorptivity to be approximately 0.81; as a result, all calculated target temperatures were 19% too high.

V. CONCLUSIONS AND RECOMMENDATIONS

The results of the structural tests demonstrate that a synergistic effect does exist between the thermal loading and blast loading in the combined loading structural tests. The tests indicate that for similar nuclear thermal/blast loading pre-stress and thermal degradation of the target by the thermal pulse would significantly enhance blast damage.

The pre-test PETROS 3.5 calculations demonstrate that the synergistic effect can be predicted, at least qualitatively, using existing structural response codes.

Although this project has demonstrated the existence of a synergistic effect for the nuclear combined thermal/blast loading simulated, further experiments are needed to determine the importance of the effect in other combined loading situations. In addition, new simulation techniques have been developed which should improve the accuracy of future thermal/blast experiments.

Since the completion of this test program, new thermal simulation techniques have been developed which should provide more repeatable thermal loading and produce less degradation of the blast wave.^{2,13} The use of the new thermal simulation technique should significantly improve the accuracy of future thermal/blast loading experiments.

In addition to changes in simulation techniques, changes in instrumentation might also improve future test programs. The strain gages used in this project proved difficult to install and their output proved difficult to interpret. The uses of optical displacement measurement, like the Moire fringe techniques, might provide more useful data for comparison with structural response code calculations.^{14,15} Whether the optical measurement could be used in the severe environment created in thermal/blast testing is not known at this time.

¹³ J. F. Dishon and R. I. Miller, "Development of a Thermal Radiation Simulator for Synergistic Blast and Thermal Radiation Testing of Full Scale Hardware," Proceedings of the 7th International Symposium on Military Applications of Blast Simulation, Medicine Hat, Alberta, Canada, 13-17 July 1981.

¹⁴ A. J. Piekutowski, "A Device to Determine the Out-of-Plane Displacement of a Surface Using a Moire Fringe Technique," University of Dayton Research Institute Report UDR-TR-29-58, May 1979.

¹⁵ A. J. Durelli and V. J. Park, Moire Analysis of Strain, Prentice-Hall, Inc., Englewood Cliffs, N.J., 1970.

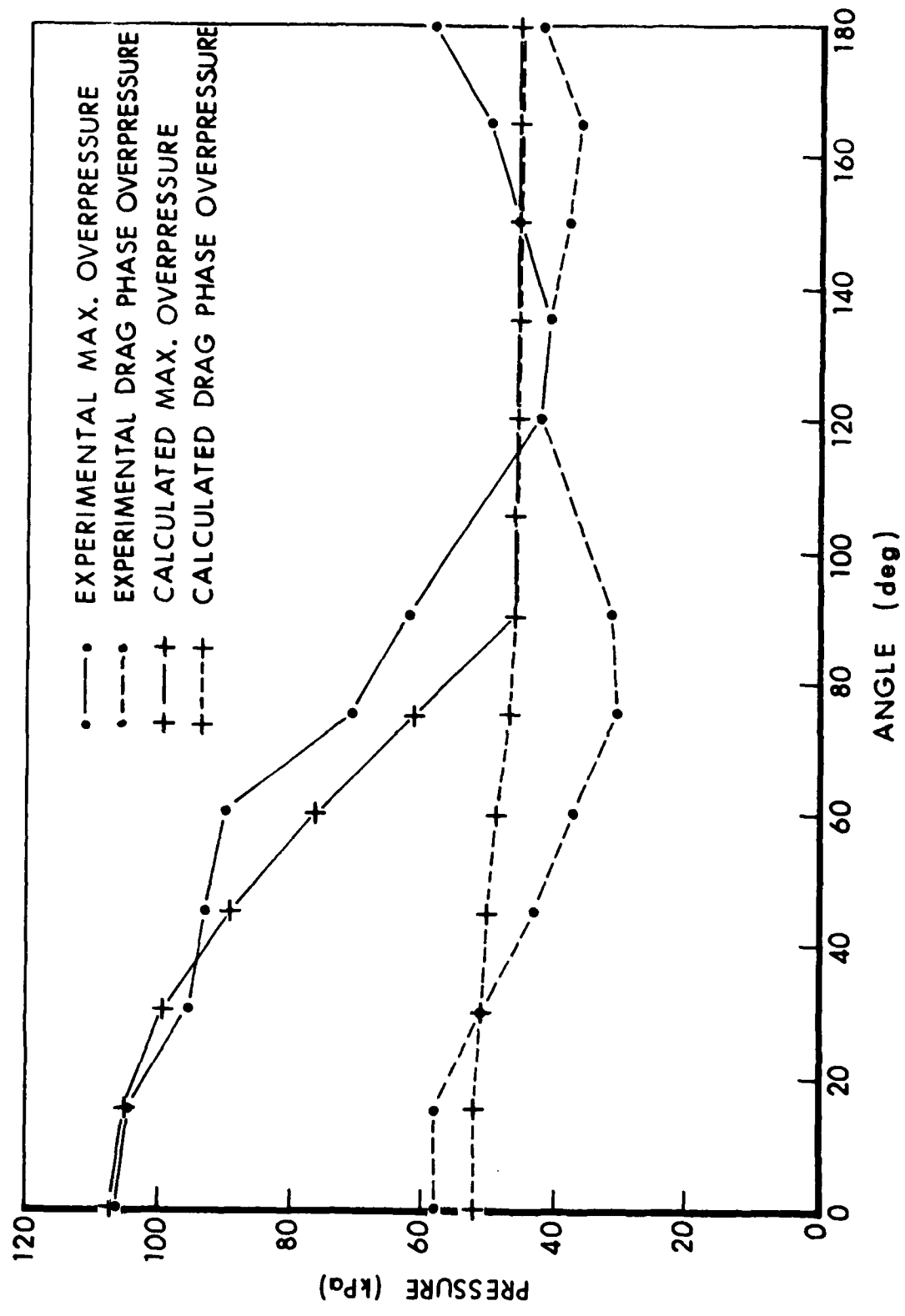


Figure 56. Experimentally Measured and Calculated Overpressure Loading.

The work now underway on the post-test structural response code modeling of the structural test should improve the accuracy of future thermal/blast loading calculations. A somewhat more complex structural response code, ADINA, is being used in the calculations. The loading function input into the code was developed from the loading measurement made during the structural tests and are more accurate than the loading function used in the PETROS 3.5 calculations. The material models being used were developed from test data on the actual target material and are also more accurate. The ADINA results should more closely model the structural tests.

Comparisons of ADINA calculation to the combined thermal/blast loading experiments will be used to verify the code's ability to model structural response to combined loading. If the code can be verified it will provide a method for predicting the vulnerability of critical military equipment in the design stage. By designing weapon systems from the outset to withstand combined nuclear thermal/blast loading, costly modification and retrofits can be avoided.

ACKNOWLEDGEMENTS

The authors would like to acknowledge contributions of James Patrick, Robert Peterson, Rodney Abrahams, George Watson, James Bernhardt and all the others whose hard work and technical expertise made the structural tests possible. The authors would also like to acknowledge the technical advice of Drs. N. J. Huffington, J. M. Santiago, W. D. Allison, A. Mark, F. H. Gregory, and the other members of the Blast Dynamics Branch.

REFERENCES

1. S. D. Pirotin, B. A. Berg and E. A. Witmer, "PETROS 3.5: New Developments and Program Manual for the Finite-Difference Calculation of Large Elastic-Plastic Transient Deformations of Multilayer Variable-Thickness Shells," U.S. Army Ballistic Research Laboratories Contract Report No. 211, Feb. 1975 (AD A007215).
2. G. D. Teel and F. H. Oertel, "Testing to Combined Blast and Thermal Effects at the BRL," Proceedings of the 7th International Symposium on Military Applications of Blast Simulation, Medicine Hat, Alberta, Canada, 13-17 July 1981.
3. F. H. Gregory, Private communication, Ballistic Research Laboratory, Jan 82.
4. A. Mark, "Shock Diffraction Computations Over Complex Structures," Technical Report ARBRL-TR-02455, US ARRADCOM, Ballistic Research Laboratory, Aberdeen Proving Ground, MD, Dec. 1982 (AD B070013L).
5. W. Heilig, "About Shock Wave Transition Phenomena in Non-Stationary Flows," Proceedings of the 7th International Symposium on Military Applications of Blast Simulation, Medicine Hat, Alberta, Canada, 13-17 July 1981.
6. C. W. Kitchens, R. E. Lottero, A. Mark and G. D. Teel, "Blast Wave Modification During Combined Thermal/Blast Simulation Testing," US Army ARRADCOM, Ballistic Research Laboratory, Aberdeen Proving Ground, MD, Report No. ARBRL-TR-02352, July 1981 (AD B059761L).
7. H. E. Lindberg, D. L. Anderson, R. D. Firth and L. V. Parker, "Response of Reentry Vehicle-Type Shells to Blast Loads," Stanford Research Institute for Lockheed Missiles and Space Company, Sunnyvale, CA, P.O. No. 24-14517, Sept. 30, 1965.
8. J. R. Vinson, Structural Mechanics: The Behavior of Plates and Shells, Wiley-Interscience, John Wiley and Son, Inc., New York, 1974.
9. S. P. Timoshenko and J. M. Gere, Theory of Elastic Stability, 2 ed, McGraw-Hill Book Company, New York, 1961.
10. W. J. Schuman, "The Response of Cylindrical Shells to External Blast Loading, Part II," Memorandum Report No. 1560, Ballistic Research Laboratory, Aberdeen Proving Ground, MD, May 1964 (AD 444335).
11. R. J. Roark and W. C. Young, Formulas for Stress and Strain, 5 ed, McGraw-Hill Book Company, New York, 1975.
12. Y. C. Fung and E. E. Secheler, "Instability of Thin Elastic Shells," Structural Mechanics, Pergamon Press, New York, 1960.

REFERENCES (Continued)

13. J. F. Dishon and R. I. Miller, "Development of a Thermal Radiation Simulator for Synergistic Blast and Thermal Radiation Testing of Full Scale Hardware," Proceedings of the 7th International Symposium on Military Applications of Blast Simulation, Medicine Hat, Alberta, Canada, 13-17 July 1981.
14. A. J. Piekutowski, "A Device to Determine the Out-of-Plane Displacement of a Surface Using a Moire Fringe Technique," University of Dayton Research Institute Report UDR-TR-29-58, May 1979.
15. A. J. Durelli and V. J. Park, Moire Analysis of Strain, Prentice-Hall, Inc., Englewood Cliffs, N.J., 1970.

APPENDIX A

COMPUTER MODELING OF TARGET RESPONSE USING PETROS 3.5

LIST OF ILLUSTRATIONS

Figure	Page
A-1 Flow Chart of Program RAYTR	94
A-2 Sublayer Model of the Stress-Strain Curve	96
A-3 Deflection Plots of a Blast Loading Calculation with a 34.5 kPa Incident Overpressure Shock Wave	98
A-4 Longitudinal and Circumferential Strain Histories at 0° and the Longitudinal Center for Blast Loading	99
A-5 Longitudinal and Circumferential Strain Histories at 90° and the Longitudinal Center for Blast Loading	100
A-6 Deflection Plots of a Thermal Loading Calculation with a 745 kJ/m ² Fluence Thermal Pulse	102
A-7 Longitudinal and Circumferential Strain Histories at 0° and the Longitudinal Center for Thermal Loading	103
A-8 Longitudinal and Circumferential Strain Histories at 90° and the Longitudinal Center for Thermal Loading	104
A-9 Deflection Plots of a Thermal/Blast Loading Calculation with a 745 kJ/m ² Fluence Thermal Pulse and a 34.5 kPa Incident Overpressure Shock Wave	105
A-10 Longitudinal and Circumferential Strain Histories at 0° and the Longitudinal Center for Thermal/Blast Loading	106
A-11 Longitudinal and Circumferential Strain Histories at 90° and the Longitudinal Center for Thermal/Blast Loading	107

Numerical calculations of target response were used in the design of the structural tests. These pre-test calculations were used to predict the loading and structural parameters which would result in significant thermal/blast synergism in the response of the target. The target was designed so that a 34.5 kPa shock wave was closest to the threshold for permanent plastic deformation and a 68.9 kPa shock wave would cause large, permanent deformation. The diameter of the target was fixed at 30.683 cm and the length of the target and its wall thickness were varied until the desired results were obtained. The target designs resulting from the blast loading calculations were tested in thermal loading calculations to insure that large permanent deformations did not result from thermal loading alone. Finally, calculations using combined thermal/blast loading were performed to determine if there was a significant synergistic effect.

The calculations were performed before any detailed experimental loading data were available; therefore, approximate loading functions based on simple analytical and empirical models had to be used. In addition, the material model used was developed by extrapolating data found in the literature. There was no data and no test methods available to determine the actual material properties for the strain rates, temperatures and thermal soak time of interest. As a result of the uncertainties in the loading functions and material properties the calculations can be viewed as an approximation of the target response. The calculations were considered only as an aid to experimental design.

The blast loading was based on a simple empirical model similar to that found in Reference A-1. The loading was assumed to be uniform along the length of the target cylinder. Further, the loading was assumed to be symmetric with respect to the vertical plane normal to the shock front and passing through the symmetry axis of the target cylinder. Due to symmetry the load in only one 180° segment had to be calculated. The loading was further broken down into a forward and rear segment. The loading on the rear 90° segment was a simple step function. At shock arrival the pressure jumped instantaneously to the static overpressure behind the incident shock and then remained constant. On the forward 90° segment the pressure jumped to some reflected overpressure whose value was a function of angle and then decayed exponentially to a stagnation overpressure which was also a function of angle. The initial reflected overpressure and the difference between stagnation and static overpressure were assumed to decrease from their values at normal incidence to zero in proportion to the cosine of the angle on the target. The time of arrival of the shock at a given angular position on the target was calculated by assuming the shock moved over the target

A-1 N. J. Huffington, J. M. Santiago, W. J. Schuman, and H. L. Wisniewski,
"Survivability Analysis for an Unsymmetrical ABM Configuration" U.S.
Army Ballistic Research Laboratories Memorandum Report No. 2461,
March 1975 (AD B003130L).

at a velocity equal to the incident shock velocity. The form of the loading function is given below in Equations A-1 and A-2.

$$t_a(\theta) = \frac{R(1 - \cos \theta)}{u_s} \quad (A-1)$$

0 for $t < t_a$

$$P(\theta t) = \begin{cases} [(P_r - P_d - P_s) e^{-\beta(t-t_a)} + P_d] \cos \theta + P_s & \text{for } t \geq t_a \text{ and } \theta \leq 90^\circ \\ \end{cases} \quad (A-2)$$

P_s for $t \geq t_a$ and $\theta < 90^\circ$

In Equation A-1 θ is the angle measured from the point of first contact between the shock and target, R is the target radius, u_s is the shock velocity and t_a is the time arrival at θ . In Equation A-2 $P(\theta, t)$ is the pressure on the cylinder at time t and angle θ , P_s is the static overpressure behind the shock, P_d is the dynamic pressure, P_r is the normally reflected overpressure and β is a decay constant.

The values of P_r , P_d and u_s were all derived from given values of P_s using the standard shock tube relations. ^{A-2, A-3} The value of β was derived from earlier blast loading experiments on cylinders.

The thermal loading was calculated numerically. A simple computer code was written to calculate the geometric shape factors which govern the radiant heat transfer between the thermal source and the target. Using the shape factors and an experimentally measured fluence history from the fluxmeter the heat input into the target was calculated as a function of time and position.

From the radiant heat transfer the temperature in the target cylinder was calculated as a function of time and position. In calculating the temperature it was assumed that the walls of the target were thermally thin; i.e., the temperature gradients through the wall thickness were negligible. Further, it was assumed that heat redistribution through reradiation, convection and conduction was negligible. Using the above assumptions and calculations of temperature was reduced to simple algebraic equation.

A-2 I.I. Glass, W. Martin and G. N. Patterson, "A Theoretical and Experimental Study of the Shock Tube," University of Toronto Institute of Aerophysics Report No. 2, Nov. 1953.

A-3 M. J. Zucrow and J. D. Hoffman, Gas Dynamics, Vol. 1, Ch. 1, John Wiley and Son, New York, 1976.

The computer code written to calculate the geometric shape factors was called RAYTR. The shape factor (S_{FT}) governing radiant heat transfer to an area element (dA) on the target is given by:

$$S_{FT}(x,y) = \frac{\cos \phi_1 \cos \phi_2}{A_2 \pi r^2} dA_2 \quad (A-3)$$

In Equation A-3 A_2 is the surface area of the thermal source, r is the length of the vector r joining the source area element dA_2 and the target area element dA_1 , ϕ_1 is the acute angle between the surface normal at dA_1 and the vector r and ϕ_2 is the acute angle between the surface normal at dA_2 and the vector r . The integration is carried out numerically. The surface of the target and the thermal source were divided into a number of small area elements. The shape factor for each target area element was calculated by summing the contributions from each of the source area elements.

A flow chart of RAYTR is shown in Figure A-1. The main program reads in the parameters defining the geometry of the target and thermal source. Subroutines TGRID and SGRID provide a means of printing out the location of the target and source area elements as a check on the input. The main program contains four nested do-loops. The inner two do-loops calculated the indices of the target surface elements and the outer two do-loops calculated the indices of the source surface elements. Subroutine GRID calculates the coordinates, direction cosines and distances between the source element and the target element based on the four do-loop indices. Subroutine SHPFC uses the information calculated in GRID to calculate first the cosines of angle ϕ_1 and ϕ_2 , then the shape factor between the source and the target element. The main program then checks to see if subroutine BLOCK is to be used. Subroutine BLOCK checks to see if the vector joining the source and the target element passes through an obstruction between the source and the target; if it does the contribution from that source element is cancelled out. The main program maintains a running total of the contributions of each source element to each target element. Finally, subroutine OUTPS creates a disk file containing the shape factor for all the target elements and prints out the values.

The calculation of the temperature histories in the target based on shape factors calculated in RAYTR and the experimental fluence histories was carried out in the structural code. The temperature was calculated using the equation given below:

$$\Delta T(t,x,y) = \frac{F_L(t) \cdot A_T S_{FT}(x,y)}{S_{FM} \cdot C_p \cdot \rho \cdot d} \quad (A-4)$$

In Equation A-4 $F_L(t)$ is the experimentally measured fluence history, A_T is the absorptivity of the target, $S_{FT}(x,y)$ is the shape factor of the target at x, y , S_{FM} is the shape factor of the flux meter used to record the fluence

^{A-4} A. J. Chapman, Heat Transfer, Chapter II, The MacMillan Co., New York, New York, 1960.

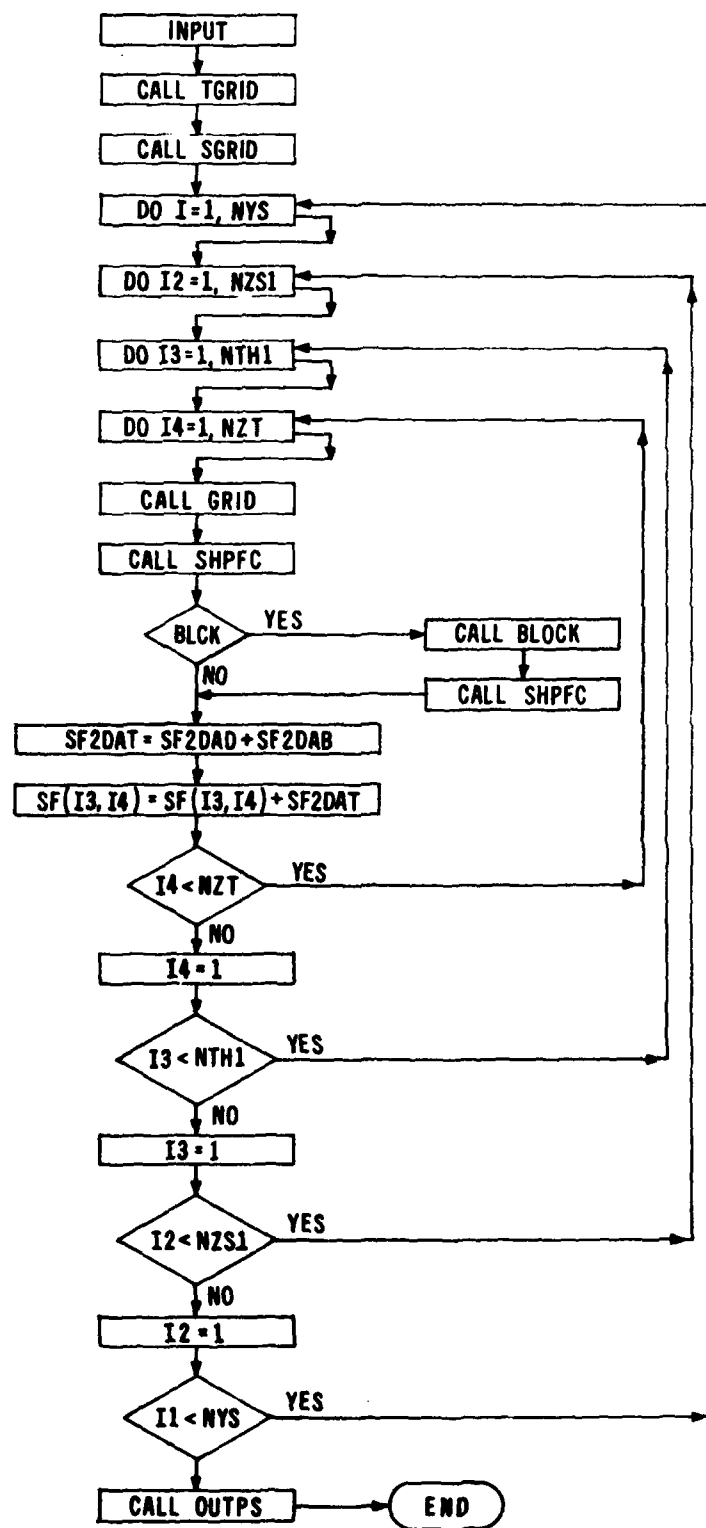


Figure A-1. Flow Chart of Program RAYTR.

history, C_p is the specific heat of the target, ρ is the density of the target and d is the thickness of the target wall.

In the actual structural code calculations it proved impractical to model the thermal loading over the entire duration of the thermal source burn. The size of the time step used in the computation was determined by the response time of the structure. The time step used in the calculation of the response of the target cylinders needed to be several orders of magnitude smaller than the duration of the thermal burn. Calculation of the response time during the entire burn would have entailed an excessive amount of computer time and resulted in a buildup of round-off error.

In order to reduce the computational time needed for the calculation of the response to thermal loading to an acceptable value, the times in the fluence history were divided by two thousand. While the speeding up of the thermal histories made the calculation possible it introduced dynamic loading effects not present in the actual structural tests. The accelerated thermal history probably overestimates the response of the target.

One other change was made in the thermal loading function to facilitate the structural response calculations. In the actual structural tests the floor and ceiling blocked part of the flux to the target cylinder. Because the target was closer to the floor than the ceiling and because the floor was longer the amount of blockage at the bottom of the target was greater than at the top. The shape factors, calculated taking the blockage into account, differed by less than ten percent between the upper and lower half of the target cylinder. Because the differences were small the thermal loading was treated as symmetric about the vertical centerline of the target. The thermal loading was symmetric about the plane joining the 0° line and the 180° line. Using the two symmetries only one quarter of the target had to be modeled in the structural code reducing the computational effort by a factor of four.

The material model used in the structural code assumed a quadratic dependence of Young's modulus, density and yield stress on temperature. The Poisson's ratio of the target's Aluminum 6061 T6 skin was assumed to be constant with temperature.

The information used to derive the Young's modulus (E) was taken from Reference A-5. The equation used is given below in Equation A-5.

$$E(T) = 7.022 \times 10^{10} - 2.509 \times 10^7 T - 2.212 \times 10^4 T^2 \quad (A-5)$$

In A-5 the temperature T is in degrees Celsius and the modulus is in Pascals. The value of Poisson's ratio was also taken from Reference A-5.

The density (ρ) was derived from Reference A-6. The equation used to model the density is given below:

A-5 J. Lipkin, J. C. Swarengen and C. H. Karnes, "Mechanical Properties of 6061-T6 AL After Rapid Heating," Sandia Laboratory Report No. SC-RR-72-0020, 1972.

A-6 D.R. Christman, W.M. Isbell, S.G. Babcock, A.R. McMillan and S.J. Green, "Measurements of Dynamic Properties of Materials, Vol. II, 6061-T6 Aluminum," Defense Nuclear Agency Contract Report DASA 2501-3, Nov. 1971.

AD-A137 730 THE EFFECTS OF THERMAL/BLAST SYNERGISM ON THE NUCLEAR
VULNERABILITY OF A. (U) ARMY ARMAMENT RESEARCH AND
DEVELOPMENT CENTER ABERDEEN PROVING GROUND

2/2

UNCLASSIFIED

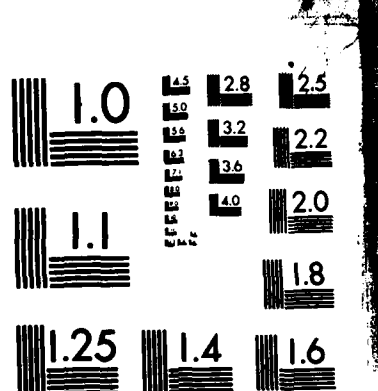
R J PEARSON ET AL. JAN 84 ARBRL-TR-02540

F/G 15/6

NL

END

FORMED
344
DHC



MICROCOPY RESOLUTION TEST CHART
NATIONAL BUREAU OF STANDARDS-1963-A

$$\rho(T) = 2.703 \times 10^{+3} - 1.811 \times 10^{-1} T - 6.896 \times 10^{-5} T^2 \quad (\text{A-6})$$

In Equation A-6 the density (ρ) is given in kilograms per cubic meter.

The stress-strain relation used in the structural response code is shown in Figure A-2. A sublayer model was used. The model contained four layers each with its own yield stress and yield strain. The yield stress of the first sublayer (σ_1) is the yield stress commonly defined for the material. The equation for the yield stress in the first sublayer was derived from Reference A-7. The equation for σ_1 is given below:

$$\sigma_1(T) = 2.958 \times 10^8 - 2.045 \times 10^5 T - 4.641 \times 10^2 T^2 \quad (\text{A-7})$$

In Equation A-7 $\sigma_1(T)$ is in Pascals. The yield strain was calculated from $E(T)$ and $\sigma_1(T)$ and is given by Equation A-8.

$$\epsilon_1(T) = 4.195 \times 10^{-3} - 5.174 \times 10^{-7} T - 9.713 \times 10^{-9} T^2 \quad (\text{A-8})$$

The strain is in meters per meter.

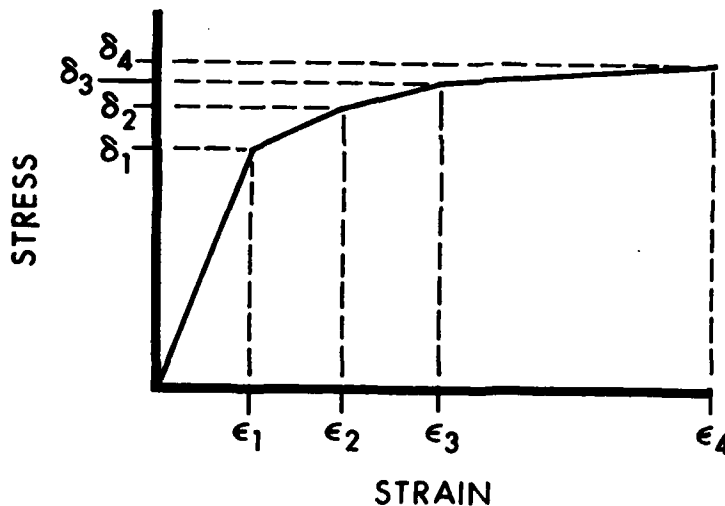


Figure A-2. Sublayer Model of the Stress-Strain Curve.

The information necessary to predict the slope of the post yield stress strain curve as a function of target temperature was not available. The strains ϵ_2 , ϵ_3 and ϵ_4 were held constant while the stress σ_2 , σ_3 , and σ_4 were adjusted to keep the slope constant between σ_1 and σ_2 , σ_2 and σ_3 and σ_3 and σ_4 . The values of the post yield stress and strain were derived from

A-7 T. Stefansky, K. Triebes and J. Shea, "Temperature-Induced Degradation of Mechanical Properties Following Instantaneous Heating," Air Force Weapons Laboratory Contract Report No. AFWL-TR-71-62, Sept. 1971.

Reference 12. The values of the strains are given below:

$$\epsilon_2 = 1.360 \times 10^{-2}, \quad \epsilon_3 = 4.716 \times 10^2 \quad \text{and} \quad \epsilon_4 = 1.041 \times 10^{-1} \quad (\text{A-9})$$

The equation for the stresses are the following:

$$\sigma_2(T) = 3.402 \times 10^8 - 2.021 \times 10^5 T - 4.182 \times 10^2 T^2 \quad (\text{A-10})$$

$$\sigma_3(T) = 3.868 \times 10^8 - 2.021 \times 10^5 T - 4.182 \times 10^2 T^2 \quad (\text{A-11})$$

$$\sigma_4(T) = 4.210 \times 10^8 - 2.021 \times 10^5 T - 4.182 \times 10^2 T^2 \quad (\text{A-12})$$

The stresses and strains are again in Pascals and meters per meter, respectively.

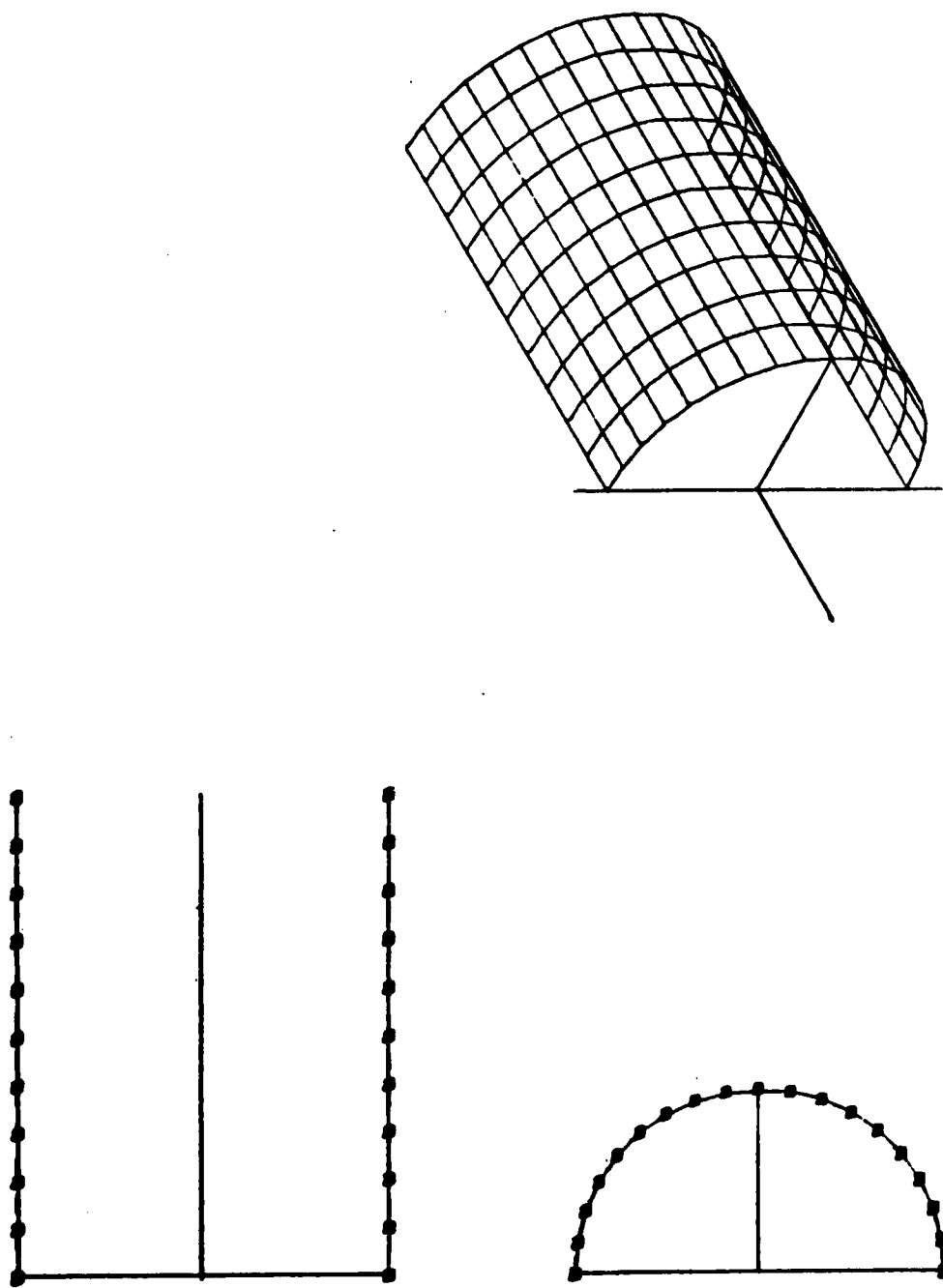
The structural response code used to calculate the stress and deformations in the target cylinder was PETROS 3.5. The PETROS 3.5 computer program employs a finite difference method to solve the equations governing finite amplitude elastoplastic response of thin shells. The code has the capability of using sublayer material models and of calculating thermal degradation of material properties based on temperature data. The code can also generalize thermal stresses on the basis of temperature data. Finally, the code can calculate structural response to complex, transient pressure loads.

The thermal loading subroutine in PETROS had to be modified in order to perform the calculation of the temperature in the target cylinder based on the fluence histories. The rest of the code was not modified because existing options were available to model the blast loading and material properties.

The results of the PETROS 3.5 calculations are shown in Figures A-3 through A-11. Figure A-3 shows the target after exposure to a 34.5 kPa incident overpressure blast wave. The plot in the upper left-hand corner of the figure shows the profile along the 0° and 180° line on the target. The plot in the lower left-hand corner is a cross section at the vertical center line of the target. The plot on the right is a is an isometric projection of the one quarter of the target cylinder modeled by PETROS 3.5. The two profiles actually contain the pre-loading profile shown as a dashed line and the post-loading profile shown as a solid line. Because the deflections are so small, the profiles appear coincident. The plots were made without magnification of the deflections from the pre-loading shape.

The circumferential and longitudinal strain histories at 0° and the vertical center line of the complete target cylinder are shown in Figure A-4. The solid line in the figure is the circumferential strain history and the dashed line is the longitudinal strain history. The same format is used in Figure A-5 to show the circumferential and longitudinal strain histories at 90° and the vertical center line.

Figure A-3. Deflection Plots of a Blast Loading Calculation with
a 34.5 kPa Incident Overpressure Shock Wave.



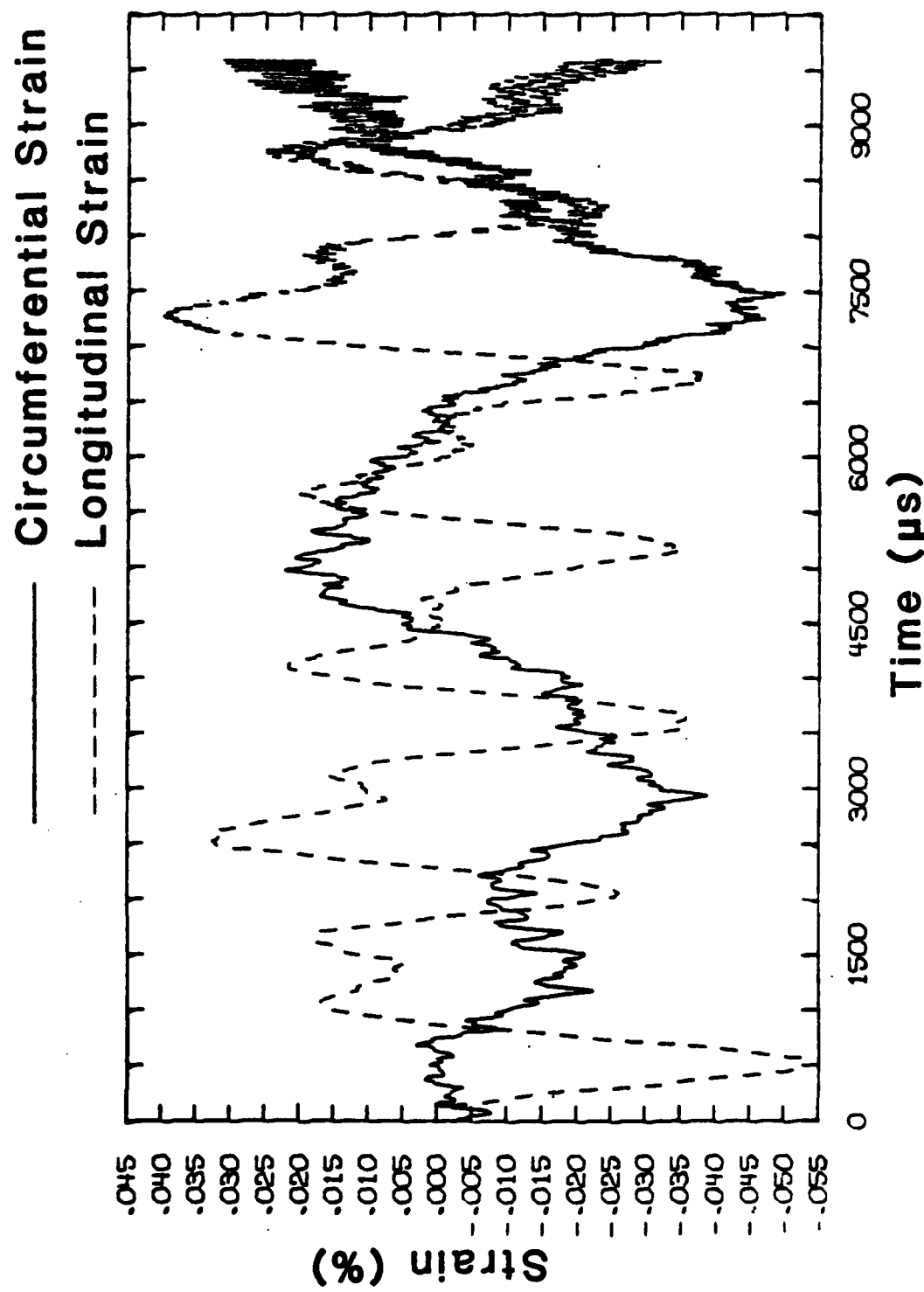


Figure A-4. Longitudinal and Circumferential Strain Histories at 0° and the Longitudinal Center for Blast Loading.

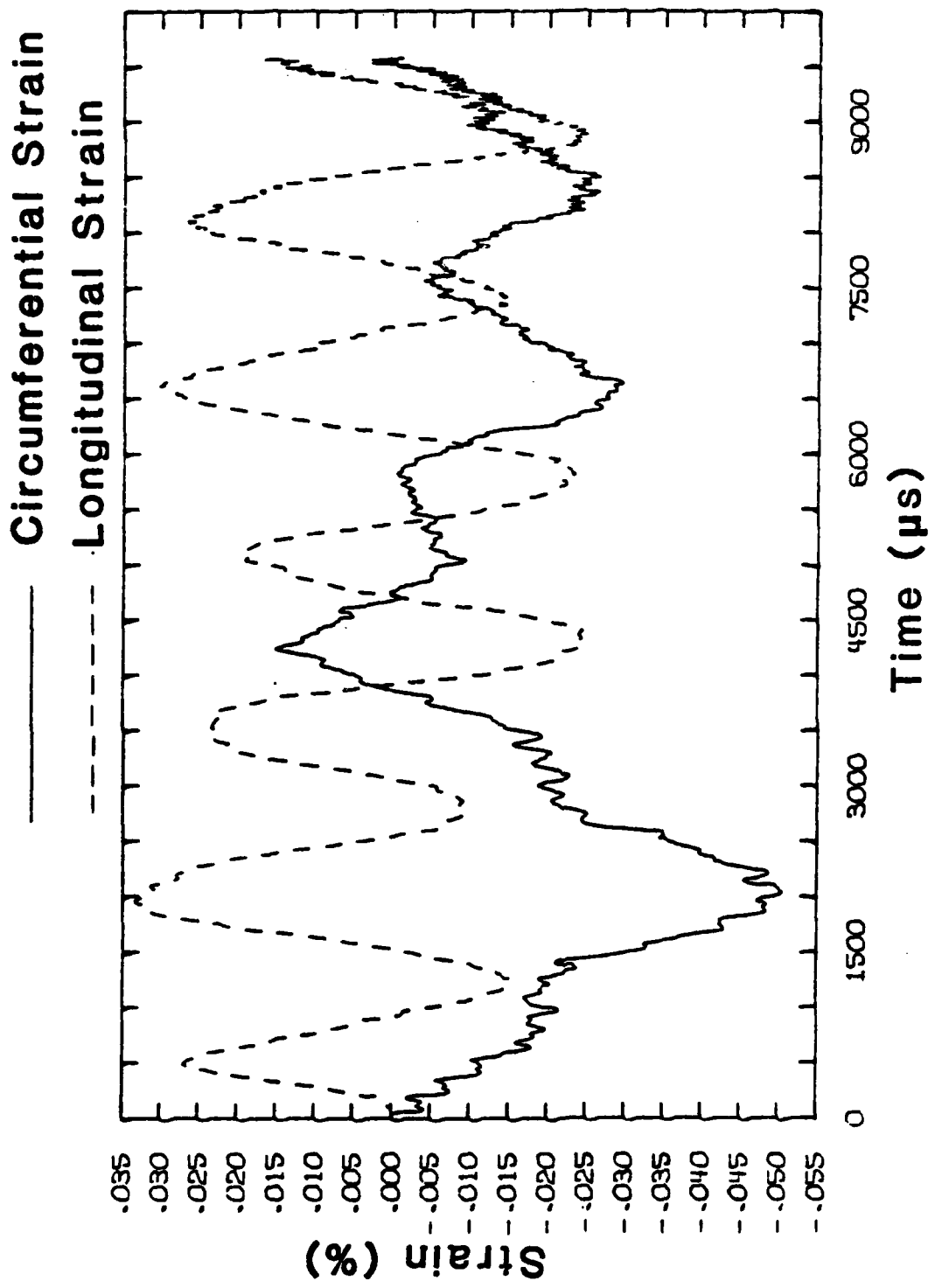


Figure A-5. Longitudinal and Circumferential Strain Histories at 90° and the Longitudinal Center for Blast Loading.

Figure A-6 shows the target cylinder after exposure to a thermal pulse with a fluence of 745 kJ/m^2 . The format is the same as in Figure A-3 with the plots on the left showing both the pre-loading and post-loading profiles and the plot on the right showing only the post-loading isometric projection. Again, the deflections have not been magnified in these plots.

Figures A-7 and A-8 show the circumferential and longitudinal strain histories at 0° and the vertical center line and at 90° and the vertical center line.

Figure A-9 shows the target after exposure to combined thermal/blast loading. A fluence of 745 kJ/m^2 was used in order to match the thermal only calculation. The incident overpressure of the blast wave that followed the thermal pulse was 34.5 kPa. The overpressure level was chosen to match the level used in the blast only calculation. The blast wave arrived at 0° on the target 4.36 ms after the start of the thermal loading. The calculation was terminated 10.7 ms after shock arrival.

Figure A-10 and A-11 show the circumferential and longitudinal strain histories at 0° and the vertical center line and at 90° and the vertical center line.

The results of the calculations indicate that for the combined thermal/blast loading simulated, a synergistic effect should exist. The synergistic effect can easily be seen in the deflection plots. The deflections from the thermal loading calculation and the blast loading calculation are both smaller than those in the combined thermal/blast calculation. Even a linear combination of the deflections calculated for the thermal loading and those calculated for the blast loading is smaller than the deflection calculated for the combined loading.

The synergistic effect can also be seen in the strain histories. The first 4.36 ms of the combined loading calculation repeats the thermal loading calculation. The strain histories are identical. After 4.36 ms the loading in the combined loading calculation was identical to the loading in the blast loading calculation. Due to the previous thermal loading, however, the strain history after 4.36 ms is not identical to the blast loading strain history. The strains in the blast loading phase of the combined calculation are much larger than those generated in the blast loading calculations. The difference between strain histories in the blast loading calculation and the strain history in the blast loading phase of the combined loading calculation again demonstrates the synergistic effect.

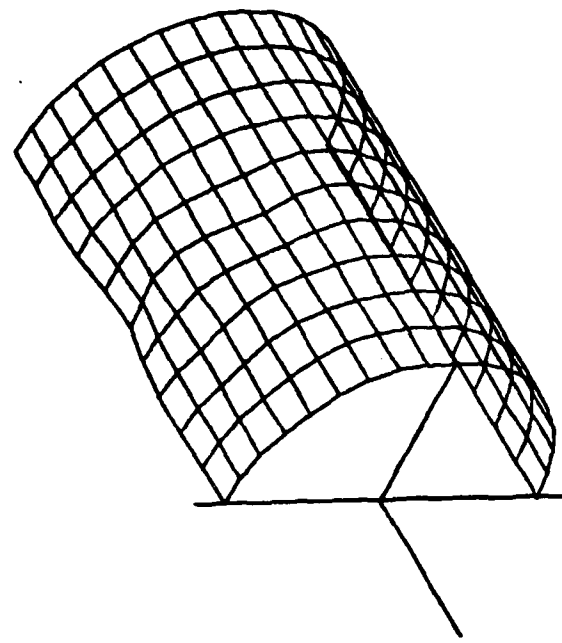
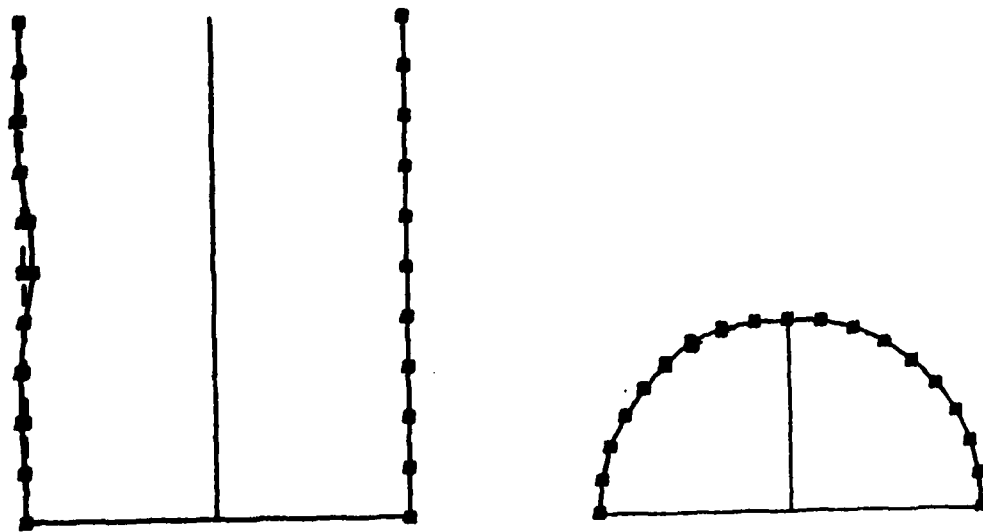


Figure A-6. Deflection Plots of a Thermal Loading Calculation with
a 745 kJ/m^2 Fluence Thermal Pulse.

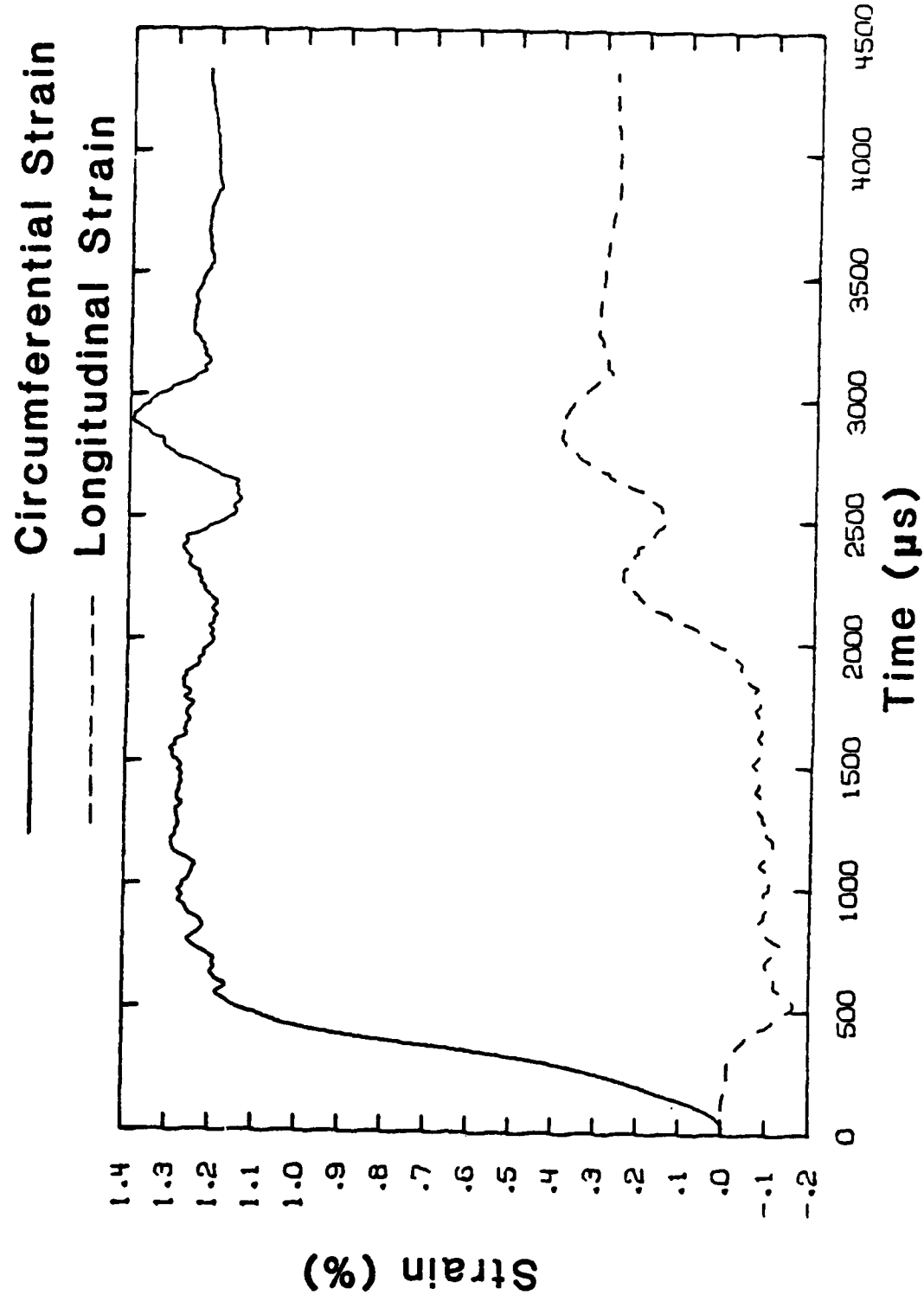


Figure A-7. Longitudinal and Circumferential Strain Histories at 0° and the Longitudinal Center for Thermal Loading.

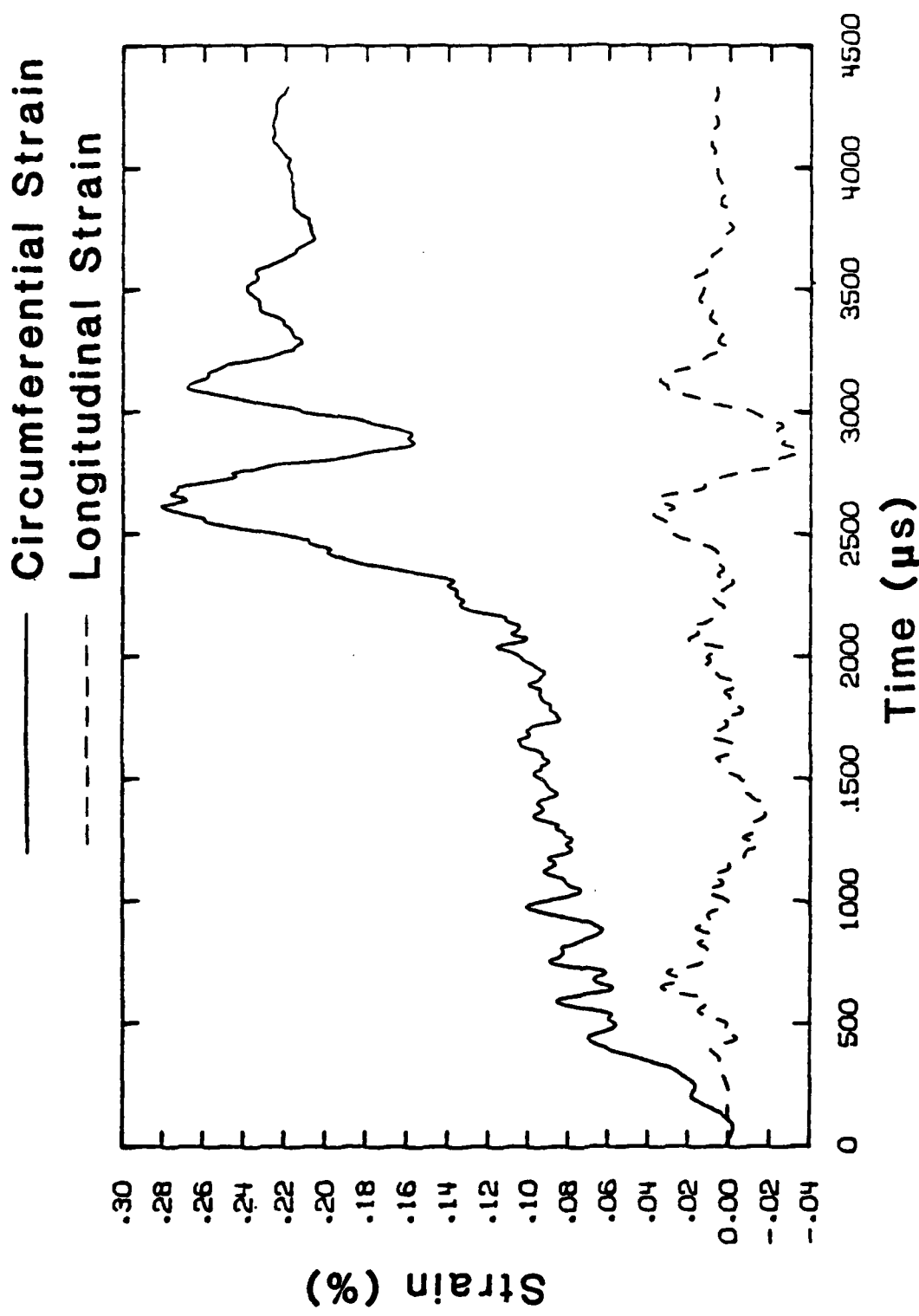
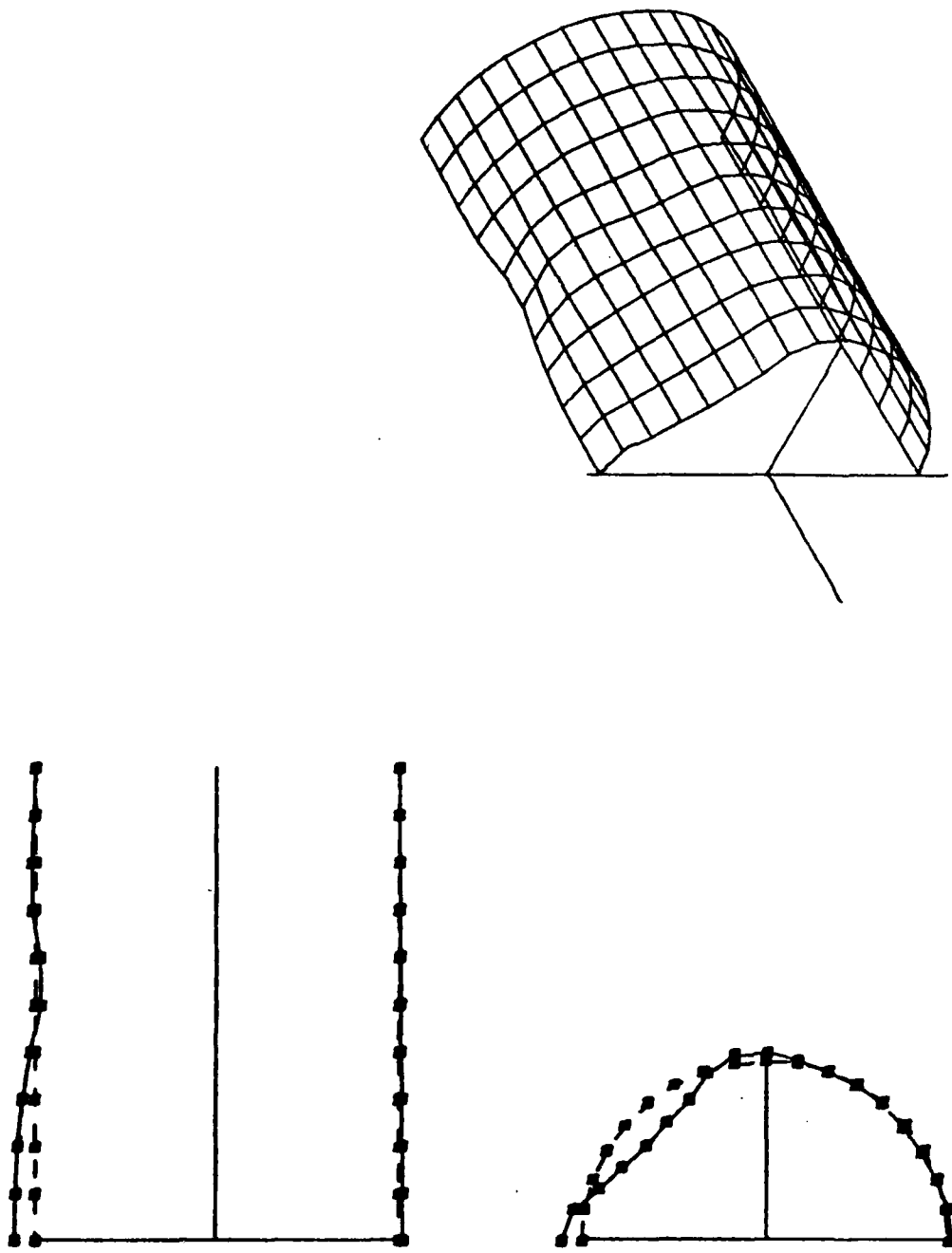


Figure A-8. Longitudinal and Circumferential Strain Histories at 90° and the Longitudinal Center for Thermal Loading.

Figure A-9. Deflection Plots of a Thermal/Blast Loading Calculation with
a 745 kJ/m^2 Fluence Thermal Pulse and a 34.5 kPa Incident
Overpressure Shock Wave.



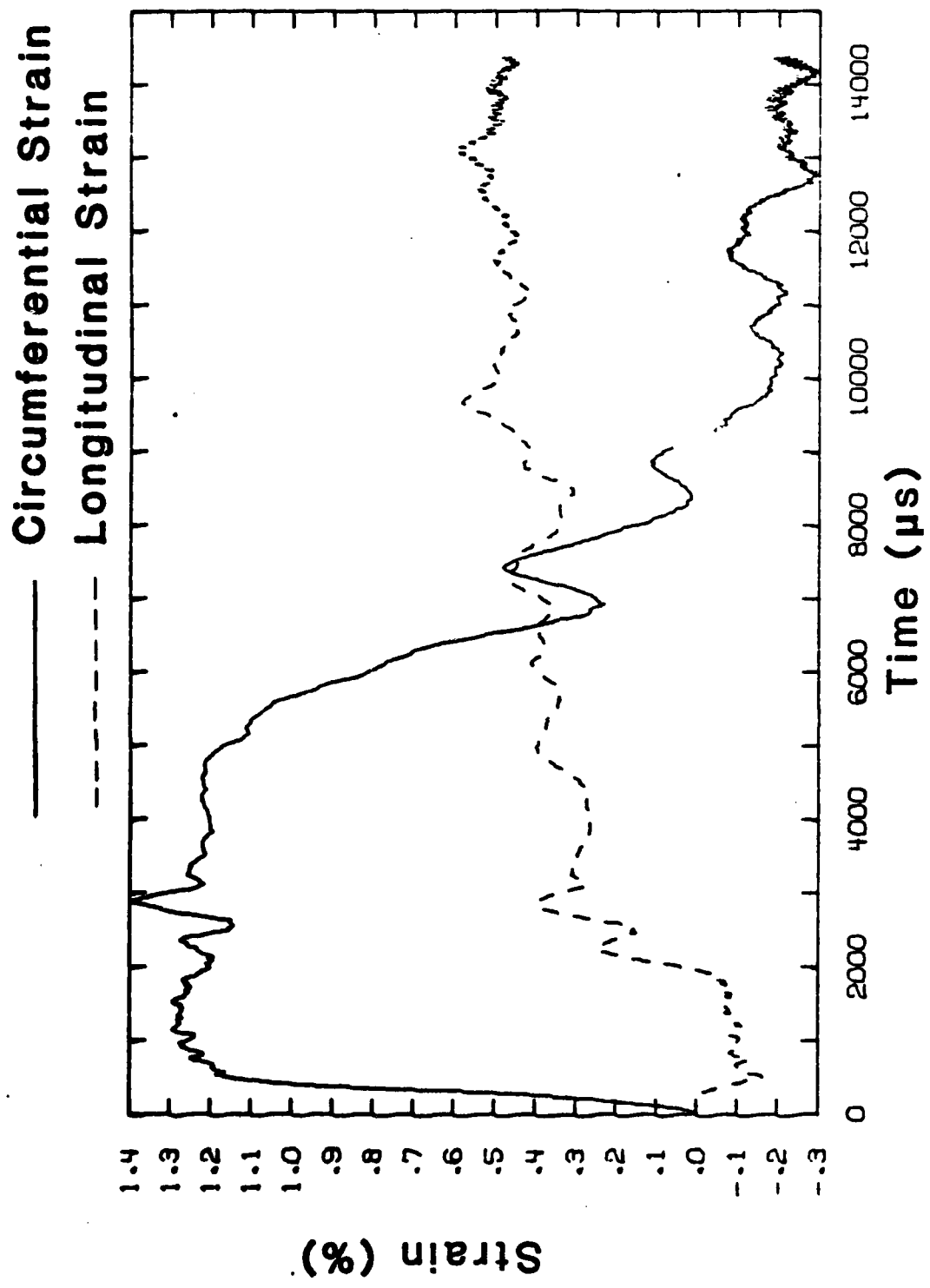


Figure A-10. Longitudinal and Circumferential Strain Histories at 0° and the Longitudinal Center for Thermal/Blast Loading.

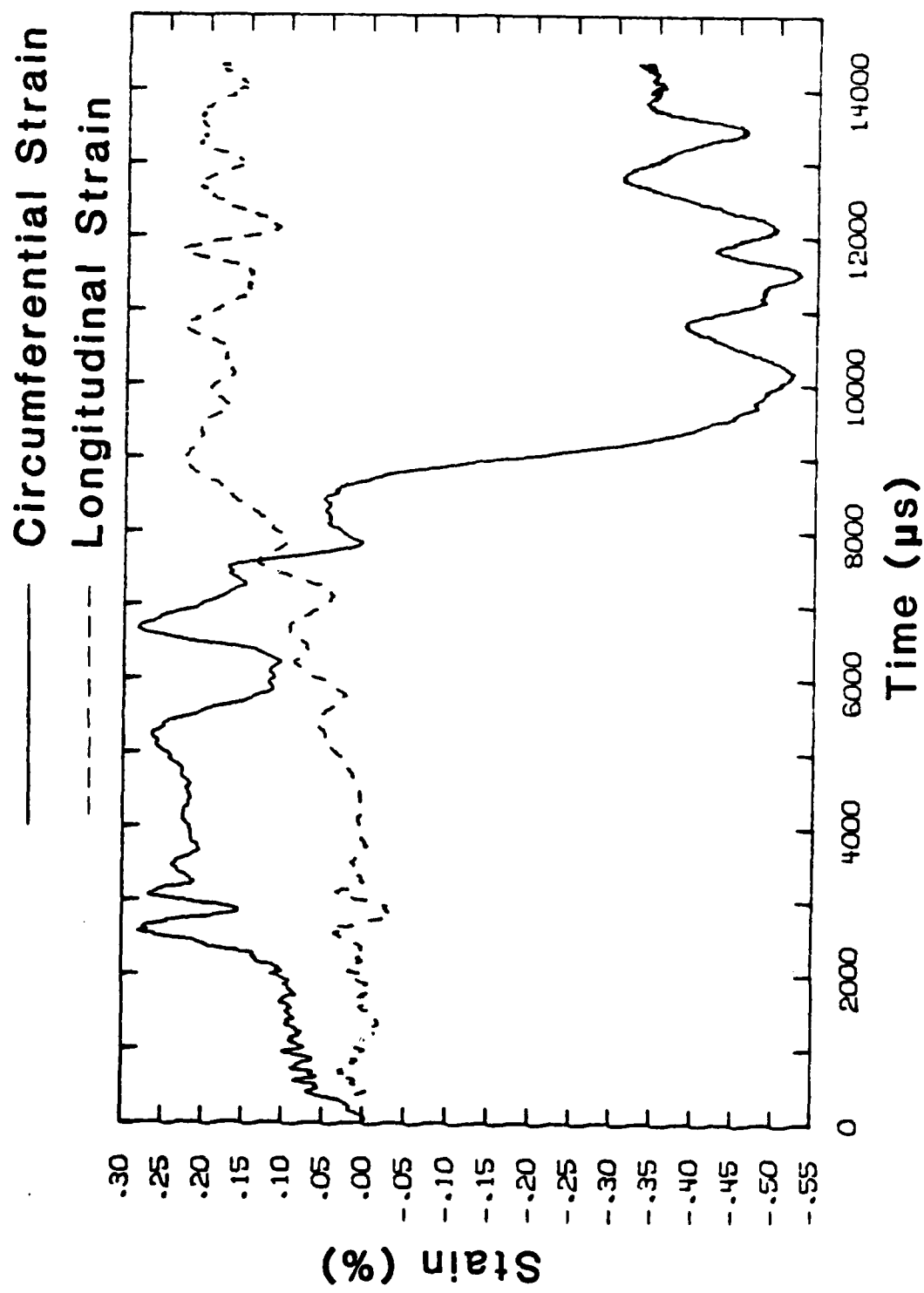


Figure A-11. Longitudinal and Circumferential Strain Histories at 90° and the Longitudinal Center for Thermal/Blast Loading.

REFERENCES

- A-1. N. J. Huffington, J. M. Santiago, W. J. Schuman, and H. L. Wisniewski, "Survivability Analysis for an Unsymmetrical ABM Configuration," U. S. Army Ballistic Research Laboratories Memorandum Report No. 2461, March 1975 (AD B003130L).
- A-2. I. I. Glass, W. Martin and G. N. Patterson, "A Theoretical and Experimental Study of the Shock Tube," University of Toronto Institute of Aerophysics Report No. 2, Nov. 1953.
- A-3. M. J. Zucrow and J. D. Hoffman, Gas Dynamics, Vol. 1, Ch. 1, John Wiley and Son, New York, 1976.
- A-4. A. J. Chapman, Heat Transfer, Chapter II, The MacMillan Co., New York, N.Y., 1960.
- A-5. J. Lipkin, J. C. Swearengen and C. H. Karnes, "Mechanical Properties of 6061-T6 AL After Rapid Heating," Sandia Laboratory Report No. SC-RR-72-0020, 1972.
- A-6. D. R. Christman, W. M. Isbell, S.G. Babcock, A. R. McMillan and S. J. Green, "Measurements of Dynamic Properties of Materials, Vol. II, 6061-T6 Aluminum," Defense Nuclear Agency Contract Report DASA 2501-3, Nov. 1971.
- A-7. T. Stefansky, K. Triebes and J. Shea, "Temperature-Induced Degradation of Mechanical Properties Following Instantaneous Heating," Air Force Weapons Laboratory Contract Report No. AFWL-TR-71-62, Sept. 1971.

APPENDIX B

DESIGN OF THE TEST APPARATUS

LIST OF ILLUSTRATIONS

Figure		Page
B-1	Assembly Drawing of the Target Mount	112
B-2	Assembly Drawing of the Friction Clamps	116

The targets used in the thermal/blast experiments were hollow aluminum cylinders with clamped ends. The targets were oriented so that the sides rather than the ends of the cylinder were loaded. A target cylinder is shown in Figure 1 of the main body of the report.

The basic target cylinder was 30.683 cm in diameter and 86.975 cm long. The wall thickness of the cylinder was 1.016 mm. The target cylinders were formed from Al 6061-T6 sheet. The sheet was first rolled to the proper size, then clamped to a specially machined heat sink where a seam was formed by heliarc welding. The diameter, length and wall thickness were determined by the loading capabilities of the BRL Thermal/Blast simulator. With the test table used in the experiment installed, the maximum side-on overpressure allowed in the simulator was 68.9 kPa (10.0 PSI). In order to insure a clean diaphragm brake which is necessary to produce a clean shock front, a side-on overpressure of at least 34.5 kPa (5 PSI) was recommended. By varying the target dimensions input into the PETROS code a target was developed which was predicted to suffer no permanent deformation at 34.5 kPa and large permanent deformations at 68.9 kPa.

One final constraint on the design of the target cylinder was the need to keep the wall thickness as small as possible so that it could be considered thermally thin. Thermally thin walls develop negligible temperature gradient through the thickness, which greatly simplifies the analysis of the experiment.

During the loading experiments the target cylinders were fixed to a heavy mount. The mount allowed only that portion of the target within 40.005 cm of the center to deform. The remaining target length is used as a bearing surface for the clamps that fix the target to the mount. An assembly drawing of the target mount is shown in Figure B-1.

In order to simplify the analysis of the experiment the target mounts were designed to produce end conditions as close to simple fixed end conditions as possible. Because fasteners produce stress concentrations and welding produces residual stress and material property degradation, it was decided these common methods should not be used to fix the target cylinder to the mount. Friction clamps were finally selected as the way to produce the best possible approximation to a fixed end condition for a target of the size required for the experiment.

The friction clamps were designed to resist the highest boundary stress generated in the PETROS model of the experiment. Using a conservative estimate of the coefficient friction between the target and the mounts, the required amount of circumferential pressure was calculated. From the circumferential pressure, the hoop stress in the clamp band and the shear stress at the joint between the ears of the clamp and clamp band were calculated. The stress indicated that in order to design a clamp that would be thin enough not to seriously disturb the air flow over the target high strength steel would have to be used. In addition, the stresses were such that welding the ears to the clamp band was not practical. The final design

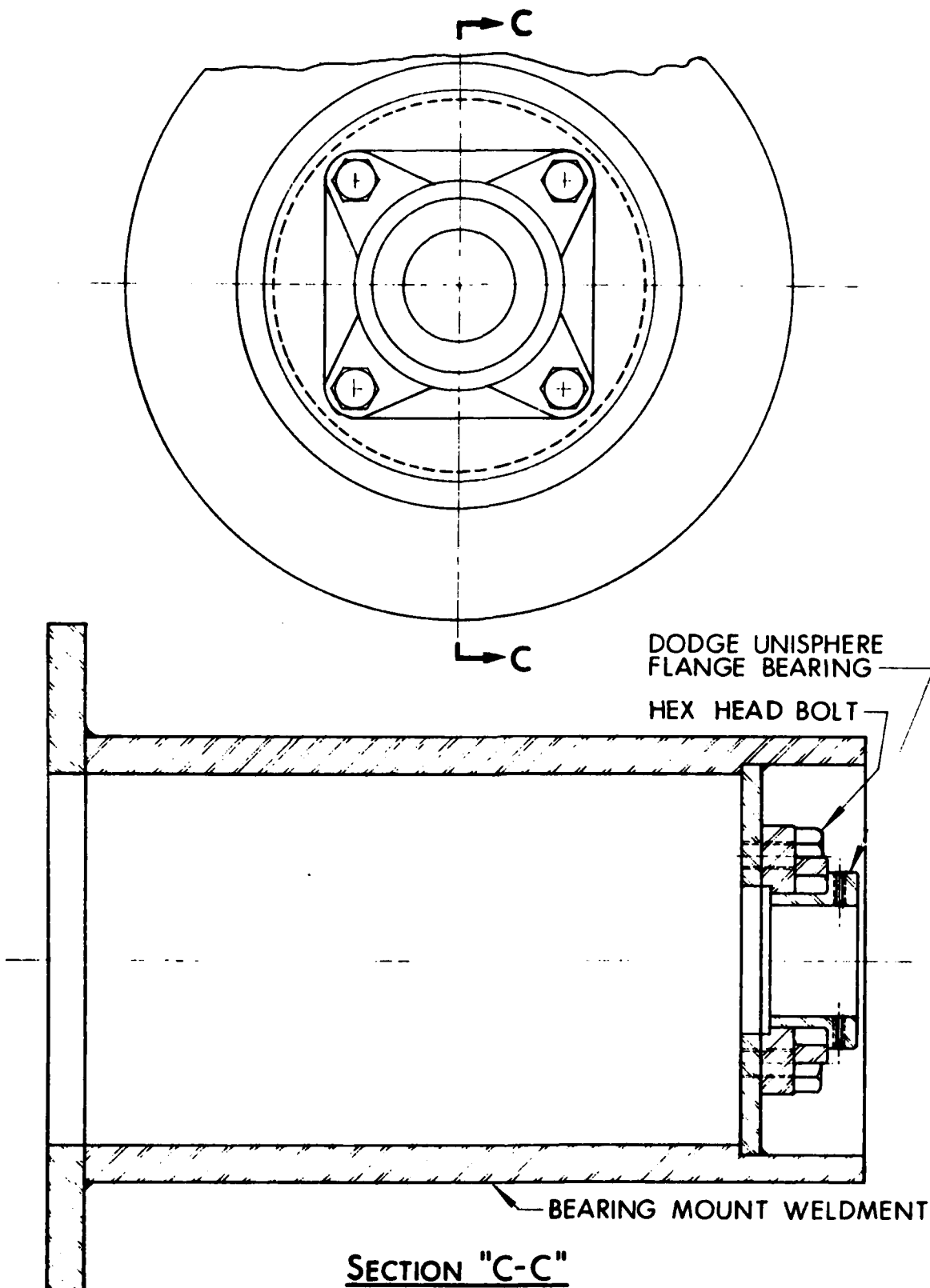


Figure B-1. Assembly Drawing of the Target Mount.

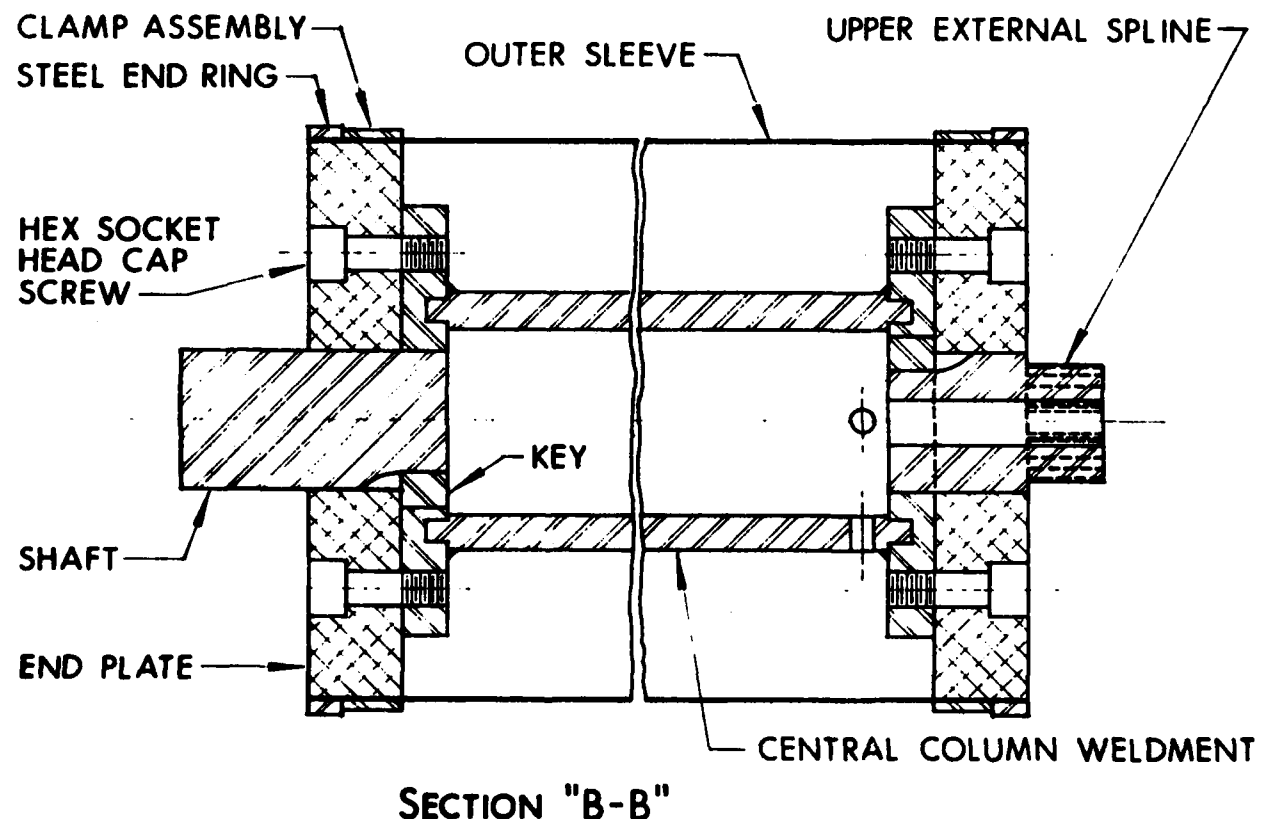
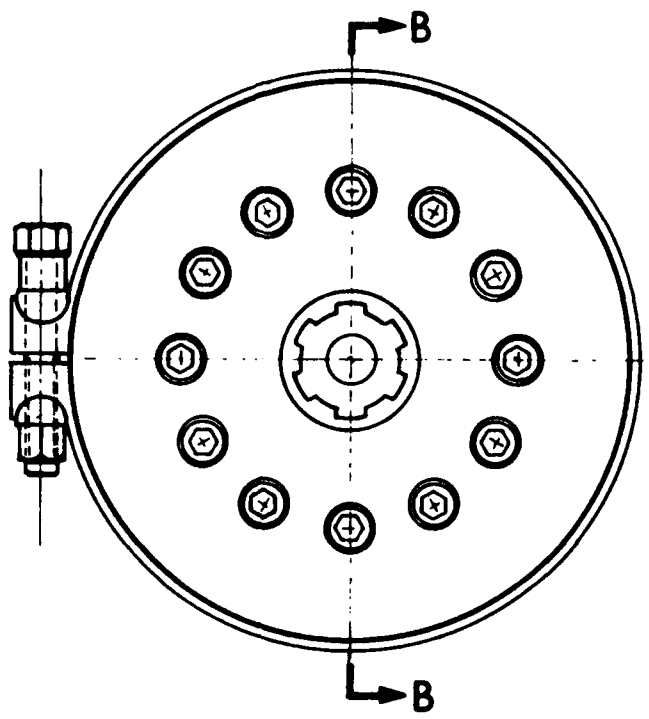


Figure B-1. (Continued) Assembly Drawing of the Target Mount.

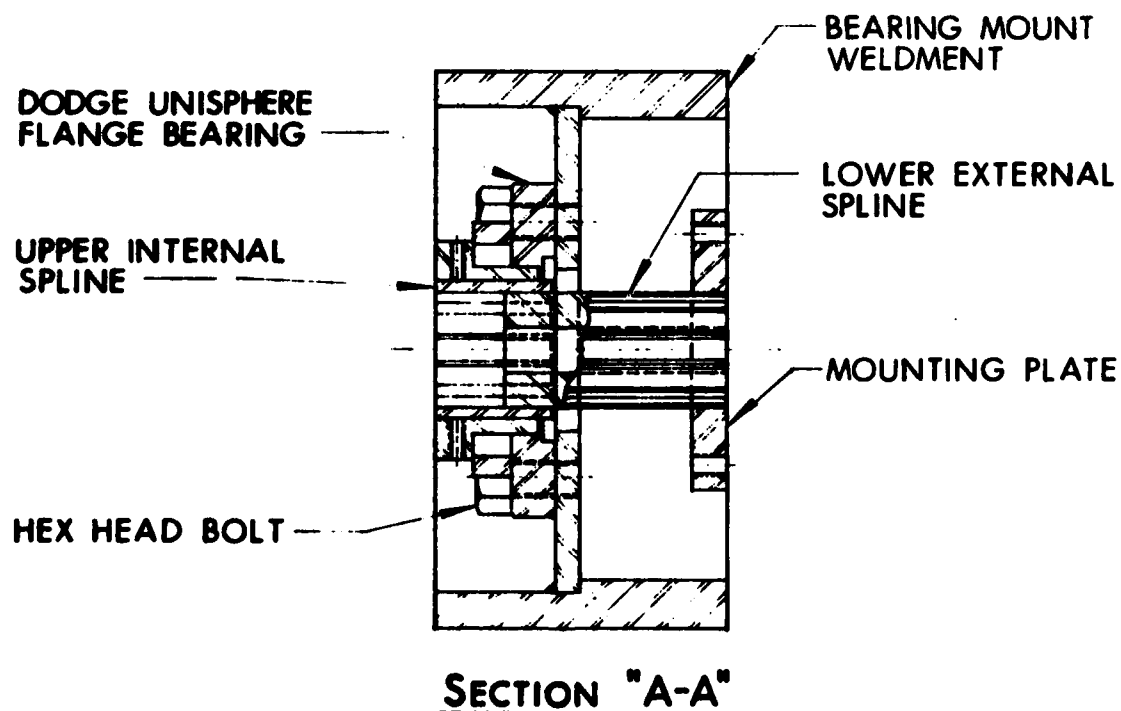
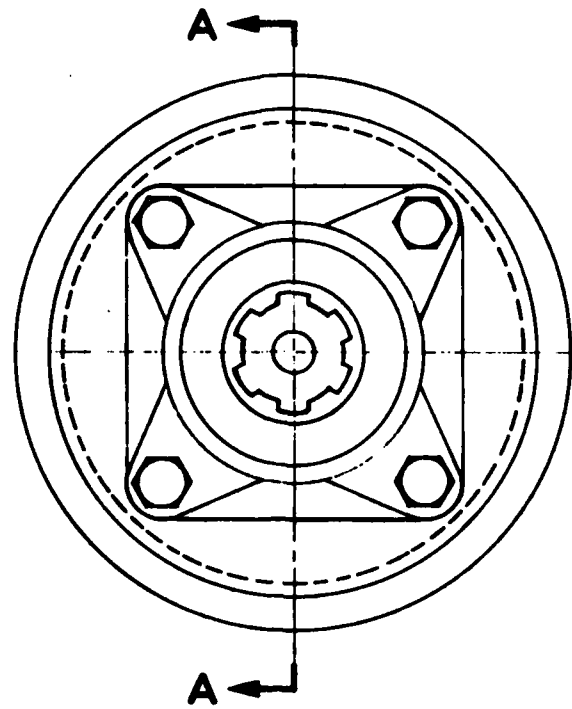


Figure B-1. (Continued) Assembly Drawing of the Target Mount.

was a clamp with an integral ear machined from a 2.54 cm thick plate of riveted homogeneous armor (RHA). The clamp was tightened with a high strength bolt. Special hemicylindrical washer and oversized bolt holes were used to allow the bolt and clamp to realign as it was tightened. The final clamp design is shown in Figure B-2.

Tests to determine the maximum force the clamp could resist were conducted using a large tensile test machine at the U.S.Army Material Test Directorate, APG,Md. A target cylinder was clamped to a pair of aluminum bulkheads which were in turn bolted to smaller diameter steel plates. A steel rod was welded to each plate and served to connect the test apparatus to the tensile testing machine. The tensile testing device was used to pull outwards on the bulkheads until they began to slip. The force at which the bulkheads began to move was recorded. The force recorded was divided by the area of the target at the clamped edge and that value was taken as the maximum boundary stress that at the boundary the clamp could resist.

During the tests it was found that tightening the clamp bolts to the same torque wrench reading did not produce repeatable results. It was found necessary to attach strain gages to the clamps themselves and use the same strain reading to obtain repeatable results.

The maximum force the clamps could resist was 133 kN (30,000 lbf) which was equivalent to an average stress in the target cylinder under the clamp of 137 MPa (19.8 ksi). The average produced stress was large enough to resist the largest predicted tensile or inward stress but not the compressive or outward stress. The bulkheads were redesigned with an additional steel reinforcing ring or lip which fit against the end of the target and prevented any outward movement. The friction clamps were retained to resist longitudinal tensile stress and the circumferential stresses.

Visual inspection of the targets after the actual test in the BRL simulator gave no indication of slippage of the target cylinder. The targets were all found to be in contact with the reinforcing ring.

A second requirement necessary to produce a fixed end condition was that no rotation of the ends occur. The target mount had to be designed to minimize bending. A cylindrical column concentric with the target cylinder was the main structural member resisting bending. In order to allow the inward deformation of the target cylinder the diameter of the column had to be kept to a minimum. The final design used a heavy walled steel tube with an outside diameter of 14.0 cm (5.5 in) and an inside diameter of 10.2 cm (4.0 in). Analysis, using beam theory, showed that rotation of the end in bending would reduce the distance between the bulkhead at the front of the target by less than 0.007% at peak loading.

Beyond providing fixed end condition the mounting system had to be designed to simplify the blast loading history on the target and provide a means of rotating the target.

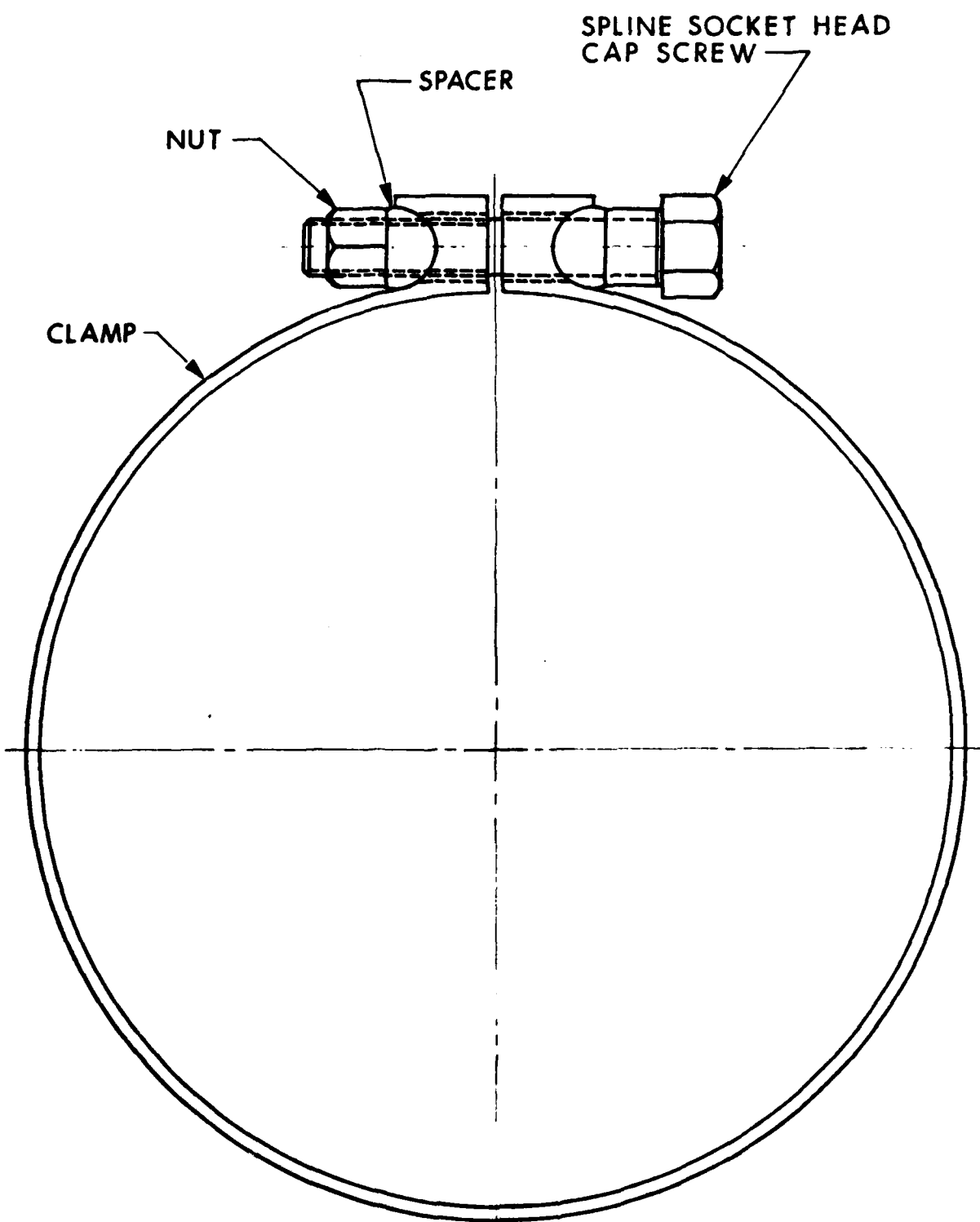


Figure B-2. Assembly Drawing of the Friction Clamps.

Rotation was provided through the use of heavy bearings and a pneumatic rotator. As is shown in Figure B-1, the target cylinder was clamped to the aluminum bulkheads, which were in turn bolted to the central column. Fastened to and concentric with the central column are two solid shafts. The upper shaft was machined to fit into a heavy, self-aligning, roller bearing located above the target. The bottom shaft was machined to form an exterior spline. The spline on the bottom shaft mated with an interior spline fit into the lower roller bearing. The interior spline mated with a second exterior spline which finally mated with a second interior spline bolted to the rotator drive shaft.

The rotator itself was a permanent part of the BRL Thermal/Blast simulator. The rotator consisted of a dual action pneumatic piston, driving a cam which in turn rotated the drive shaft. The piston was actuated by solenoid valves controlled by the systems' timing unit.

The bearing mounts located above and below the target served a second function. The mounts were formed from heavy walled tubes with the same outside diameter as the target. The bearing mounts then continued the cylindrical shape of the target across the simulator to meet the floor and ceiling. The floor and ceiling were designed so that the rarefaction wave from the ends would take at least 2.5 crossing times to reach the cylinder. A crossing time is the time taken by the shock to completely engulf the target. Two and a half crossing times is approximately the time it took for the pressure behind the shock reflected from the target to drop to a level matching that on the ends of the cylinder. By continuing the target's cylindrical shape across the simulator, the pressure loading was rendered approximately two-dimensional. Comparisons with matching two-dimensional computer calculations of the shock loading shows a good agreement with experimentally measured pressure on the bearing mount.

The results of the experiments indicated that the target met the design objectives. The design provided fixed-end condition, two-dimensional shock loading and a means of rotating the target.

DISTRIBUTION LIST

<u>No. of Copies</u>	<u>Organization</u>	<u>No. of Copies</u>	<u>Organization</u>
12	Commander Defense Technical Info Center ATTN: DTIC-DDA Cameron Station Alexandria, VA 22314	1	Director Defense Communications Agency ATTN: 930 Washington, DC 20305
1	Director of Defense Research & Engineering ATTN: DD/TWP Washington, DC 20301	9	Director Defense Nuclear Agency ATTN: DDST TIPL/Tech Lib SPSS/K. Goering G. Ullrich SPTD/T. Kennedy SPAS/J. Slaughter STSP/R. Hohr NATD NATA Washington, DC 20305
1	Asst. to the Secretary of Defense (Atomic Energy) ATTN: Document Control Washington, DC 20301		
1	Director Defense Advanced Research Projects Agency ATTN: Tech Lib 1400 Wilson Boulevard Arlington, VA 22209	2	Commander Field Command, DNA ATTN: FCPR FCTMDF Kirtland AFB, NM 87115
2	Director Federal Emergency Management Agency ATTN: Mr. George Sisson/RF-SR Technical Library Washington, DC 20301	1	Commander Field Command, DNA Livermore Branch ATTN: FCPRL P.O. Box L-395 Livermore, CA 94550
1	Director Defense Intelligence Agency ATTN: DT-2/Wpns & Sys Div Washington, DC 20301	1	Director Inst for Defense Analyses ATTN: Library 1801 Beauregard Street Alexandria, VA 22311
1	Director National Security Agency ATTN: E. F. Butala, R15 Ft. George G. Meade, MD 20755	1	Director US Army BMD Program Office ATTN: John Shea 5001 Eisenhower Avenue Alexandria, VA 22333
1	Director Joint Strategic Target Planning Staff JCS Offut AFB, NB 68113		

DISTRIBUTION LIST

<u>No. of Copies</u>	<u>Organization</u>	<u>No. of Copies</u>	<u>Organization</u>
2	Director US Army BMD Advanced Technology Center ATTN: CRDABH-X; CRDABH-S P.O. Box 1500 Huntsville, AL 35807	1	Commander US Army Materiel Development and Readiness Command ATTN: DRCDMD-ST 5001 Eisenhower Avenue Alexandria, VA 22333
1	Commander US Army BMD Systems Command ATTN: BDMSC-TFN/N.J. Hurst P.O. Box 1500 Huntsville, AL 35807	1	Commander US Army Armament Research and Development Center ATTN: DRDAR-TDC Dover, NJ 07801
2	Deputy Chief of Staff for Operations and Plans ATTN: Technical Library Director of Chemical & Nuc Operations Department of the Army Washington, DC 20310	3	Commander US Army Armament Research and Development Center ATTN: DRDAR-LCN-F, W. Reiner DRDAR-TSS Dover, NJ 07801
2	Chief of Engineers Department of the Army ATTN: DAEN-MCE-D DAEN-RDM 890 South Pickett Street Alexandria, VA 22304	1	Commander US Army Armament Materiel Readiness command ATTN: DRSAR-LEP-L Rock Island, IL 61299
3	Commander US Army Engineer Waterways Experiment Station ATTN: Technical Library William Flathau Leo Ingram P.O. Box 631 Vicksburg, MS 39181	1	Director US Army ARDC Benet Weapons Laboratory ATTN: DRSAR-LCB-TL Watervliet, NY 12189
1	Commander US Army Engineering Center ATTN: ATSEN-SY-L Fort Belvoir, VA 22060	1	Commander US Army Aviation Research and Development Command ATTN: DRDAV-E 4300 Goodfellow Boulevard St. Louis, MO 63120
1	Commander US Army MERADCOM ATTN: DRDME-EM, D. Frink Fort Belvoir, VA 22060	1	Director US Army Air Mobility Research and Development Laboratory Ames Research Center Moffett Field, CA 94035

DISTRIBUTION LIST

<u>No. of Copies</u>	<u>Organization</u>	<u>No. of Copies</u>	<u>Organization</u>
1	Commander US Army Communications Rsch and Development Command ATTN: DRSEL-ATDD Fort Monmouth, NJ 07703	1	Commander US Army Missile Command ATTN: Technical Library Redstone Arsenal, AL 35898
3	Commander US Army Electronics Research and Development Command ATTN: DELSD-L DELEW-E, W. S. McAfee DELS-D-EI, J. Roma Fort Monmouth, NJ 07703	4	Commander US Army Natick Research and Development Command ATTN: DRXRE/Dr. D. Sieling DRXNE-UE/A. Johnson A. Murphy W. Crenshaw Natick, MA 01762
8	Commander US Army Harry Diamond Labs ATTN: Mr. James Gaul Mr. L. Belliveau Mr. J. Meszaros Mr. J. Gwaltney Mr. F. W. Balicki Mr. Bill Vault Mr. R. J. Bostak Mr. R. K. Warner 2800 Powder Mill Road Adelphi, MD 20783	1	Commander US Army Tank Automotive Command ATTN: DRSTA-TSL Warren, MI 48090
4	Commander US Army Harry Diamond Labs ATTN: DELHD-TA-L DRXDO-TI/002 DRXDO-NP DELHD-RBA/J. Rosado 2800 Powder Mill Road Adelphi, MD 20783	1	Commander US Army Foreign Science and Technology Center ATTN: Rsch & Concepts Br 220 7th Street, NE Charlottesville, VA 22901
1	Commander US Army Missile Command ATTN: DRSMI-R Redstone Arsenal, AL 35898	1	Commander US Army Logistics Center ATTN: ATCL-SCA Mr. Robert Cameron Fort Lee, VA 23801
1	Commander US Army Missile Command ATTN: DRSMI-YDL Redstone Arsenal, AL 35898	3	Commander US Army Materials and Mechanics Research Center ATTN: Technical Library DRXMR-ER, Joe Prifti Eugene de Luca Watertown, MA 02172
		1	Commander US Army Research Office P.O. Box 12211 Research Triangle Park NC 27709

DISTRIBUTION LIST

<u>No. of Copies</u>	<u>Organization</u>	<u>No. of Copies</u>	<u>Organization</u>
4	Commander USA Nuclear & Chemical Agency ATTN: ACTA-NAW MONA-WE Technical Library MAJ Uecke 7500 Backlick Rd, Bldg. 2073 Springfield, VA 22150	2	Chief of Naval Operations ATTN: OP-03EG OP-985F Department of the Navy Washington, DC 20350
1	Commander US Army TRADOC ATTN: ATCD-SA, Mr. O. Wells Fort Monroe, VA 23651	1	Office of Naval Research ATTN: N. Perrone 800 N. Quincy Street Arlington, VA 22217
2	Director US Army TRADOC Systems Analysis Activity ATTN: LTC John Hesse ATAA-SL White Sands Missile Range NM 88002	1	Director Strategic Systems Projects Ofc ATTN: NSP-43, Tech Library Munitions Bldg, Rm 3245 Washington, DC 20360
1	Commander USA Combined Arms Combat Developments Activity ATTN: ATCA-CO, Mr. L. C. Pleger Fort Leavenworth, KS 66027	1	Commander Naval Electronic Systems Com ATTN: PME 117-21A Washington, DC 20360
2	Commandant US Army Infantry School ATTN: ATSH-CO-CSO-OR Fort Benning, GA 31905	1	Commander Naval Facilities Engineering Command ATTN: Technical Library Washington, DC 20360
1	Commandant Interservice Nuclear Weapons School ATTN: Technical Library Kirtland AFB, NM 87117	1	Commander Naval Sea Systems Command ATTN: ORD-91313, Library Department of the Navy Washington, DC 20360
1	Chief of Naval Material ATTN: MAT 0323 Department of the Navy Washington, DC 20360	3	Officer-in-Charge Civil Engineering Laboratory Naval Constr Btn Center ATTN: Stan Takahashi R. J. Odello Technical Library Port Hueneme, CA 93041
		1	Commander David W. Taylor Naval Ship Research & Development Ctr ATTN: Lib Div, Code 522 Bethesda, MD 20084

DISTRIBUTION LIST

<u>No. of Copies</u>	<u>Organization</u>	<u>No. of Copies</u>	<u>Organization</u>
1	Commander Naval Surface Weapons Center ATTN: DX-21, Library Br. Dahlgren, VA 22448	1	AFWL/NTES (R. Henny) Kirtland AFB, NM 87117
2	Commander Naval Surface Weapons Center ATTN: Code WA501/Navy Nuclear Programs Office Code WX21/Tech Library Silver Spring, MD 20910	1	AFWL/NTE, M. Plamondon Kirtland AFB, NM 87117
1	Commander Naval Weapons Center ATTN: Code 533, Tech Lib China Lake, CA 93555	2	Commander-in-Chief Strategic Air Command ATTN: NRI-STINFO Lib Offutt AFB, NB 68113
1	Commander Naval Weapons Evaluation Fac ATTN: Document Control Kirtland Air Force Base Albuquerque, NM 87117	1	AFIT (Lib Bldg. 640, Area B) Wright-Patterson AFB Ohio 45433
1	Commander Naval Research Laboratory ATTN: Code 2027, Tech Lib Washington, DC 20375	1	FTD (TD/BTA/Lib) Wright-Patterson AFB Ohio 45433
1	Superintendent Naval Postgraduate School ATTN: Code 2124, Technical Reports Library Monterey, CA 93940	1	Director Lawrence Livermore Lab ATTN: Tech Info Dept L-3 P.O. Box 808 Livermore, CA 94550
1	AFSC (Tech Lib)-SDOA Andrews Air Force Base MD 20334	2	Director Los Alamos Scientific Labv ATTN: Doc Control for Rpts Lib R. A. Gentry P.O. Box 1663 Los Alamos, NM 87545
1	ADTC (Tech Lib) Eglin AFB, FL 32542	2	Director Sandia Laboratories ATTN: Doc Control for 3141 Sandia Rpt Collection L. J. Vortman Albuquerque, NM 87115
1	AFATL (DLYV) Eglin AFB, FL 32542	1	Director Sandia Laboratories ATTN: Doc Control for Tech Lib P.O. Box 969 Livermore, CA 94550
1	RADC (EMTLD/Docu Library) Griffiss AFB, NY 13340		

DISTRIBUTION LIST

<u>No. of Copies</u>	<u>Organization</u>	<u>No. of Copies</u>	<u>Organization</u>
1	Director National Aeronautics and Space Administration Scientific & Tech Info Fac P.O. Box 8757 Baltimore/Washington International Airport MD 21240	1	AFWL/SUL Kirtland AFB, NM 87117
1	Aerospace Corporation ATTN: Tech Info Services P.O. Box 92957 Los Angeles, CA 90009	1	Kaman Sciences Corporation ATTN: Don Sachs Suite 703 2001 Jefferson Davis Highway Arlington, VA 22202
1	Agbabian Associates ATTN: M. Agbabian 250 North Nash Street El Segundo, CA 90245	1	Kaman-TEMPO ATTN: DASIAC P.O. Drawer QO Santa Barbara, CA 93102
1	The BDM Corporation ATTN: Richard Hensley P.O. Box 9274 Albuquerque International Albuquerque, NM 87119	1	Kaman-TEMPO ATTN: E. Bryant, Suite UL-1 715 Shamrock Road Bel Air, MD 21014
1	The Boeing Company ATTN: Aerospace library P.O. Box 3707 Seattle, WA 98124	1	Lockheed Missiles & Space Co. ATTN: J. J. Murphy, Dept. 81-11, Bldg. 154 P.O. Box 504 Sunnyvale, CA 94086
1	Goodyear Aerospace Corp ATTN: R. M. Brown, Bldg 1 Shelter Engineering Litchfield Park, AZ 85340	1	Martin Marietta Aerospace Orlando Division ATTN: G. Fotieo P.O. Box 5837 Orlando, FL 32805
5	Kaman AviDyne ATTN: Dr. N.P. Hobbs (4 cys) Mr. S. Criscione 83 Second Avenue Northwest Industrial Park Burlington, MA 01830	2	McDonnell Douglas Astronautics Corporation ATTN: Robert W. Halprin Dr. P. Lewis 5301 Bolsa Avenue Huntington Beach, CA 92647
3	Kaman Sciences Corporation ATTN: Library P. A. Ellis F. H. Shelton 1500 Garden of the Gods Road Colorado Springs, CO 80907	2	The Mitre Corporation ATTN: Library J. Calligeros, Mail Stop B-150 P.O. Box 208 Bedford, MA 01730

DISTRIBUTION LIST

<u>No. of Copies</u>	<u>Organization</u>	<u>No. of Copies</u>	<u>Organization</u>
1	Pacific Sierra Research Corp ATTN: Dr. Harold Brode 1456 Cloverfield Boulevard Santa Monica, CA 90404	1	Science Systems and Software ATTN: Technical Library PO Box 1620 La Jolla, CA 92037
2	Physics International Corp ATTN: Technical Library Mr. Fred Sauer 2700 Merced Street San Leandro, CA 94577	1	TRW Systems Group ATTN: Benjamin Sussoltz One Space Park Redondo Beach, CA 92078
1	Radkowski Associates ATTN: Peter R. Radkowski P.O. Box 5474 Riverside, CA 92517	2	Union Carbide Corporation Holifield National Laboratory ATTN: Doc Control for Tech Lib Civil Defense Research Proj PO Box X Oak Ridge, TN 37830
3	R&D Associates ATTN: Jerry Carpenter Technical Library Allan Kuhl P.O. Box 9695 Marina del Rey, CA 90291	1	IIT Research Institute ATTN: Milton R. Johnson 10 West 35th Street Chicago, IL 60616
1	RCA Bldg 127-2 Moorestown, NJ 08057	1	Battelle Memorial Institute ATTN: Technical Library 505 King Avenue Columbus, OH 43201
2	Science Applications, Inc. ATTN: Burton S. Chambers John Cockayne P.O. Box 1303 1710 Goodridge Drive McLean, VA 22102	1	California Inst of Tech ATTN: T. J. Ahrens 1201 E. California Blvd. Pasadena, CA 91102
1	Science Applications, Inc. ATTN: Technical Library 1250 Prospect Plaza La Jolla, CA 92037	2	University of Denver Denver Research Institute ATTN: Mr. J. Wisotski Technical Library 2390 South Union Blvd. Denver, CO 80210
1	Science Systems and Software ATTN: C. E. Needham PO Box 8243 Albuquerque, NM 87198		

DISTRIBUTION LIST

No. of <u>Copies</u>	<u>Organization</u>
-------------------------	---------------------

- 1 J. D. Haltiwanger
Consulting Services
B106a Civil Engineering Bldg.
208 N. Romine Street
Urbana, IL 61801
- 1 Massachusetts Int of Tech
Aeroelastic & Structures
Research Laboratory
ATTN: DR. E.A. Witmer
77 Massachusetts Avenue
Cambridge, MA 02139
- 2 Southwest Research Institute
ATTN: Dr. W. E. Baker
A. B. Wenzel
8500 Culebra Road
San Antonio, TX 78228
- 1 SRI International
ATTN: Dr. G. R.
Abrahamson
333 Ravenswood Avenue
Menlo Park, CA 94025
- 1 Stanford University
ATTN: Dr. D. Bershadet
Durand Laboratory
Stanford, CA 94305
- 1 Washington State University
Physics Department
ATTN: G. R. Fowles
Pullman, WA 99163

Aberdeen Proving Ground

Dir, USAMSA
ATTN: DRXSY-D
DRXSY-MP, H. Cohen
Cdr, USATECOM
ATTN: DRSTE-TO-F
Dir, USACSL
ATTN: DRDAR-CLR-PA
DRDAR-CLN
DRDAR-CLJ-L

USER EVALUATION OF REPORT

Please take a few minutes to answer the questions below; tear out this sheet, fold as indicated, staple or tape closed, and place in the mail. Your comments will provide us with information for improving future reports.

1. BRL Report Number _____
2. Does this report satisfy a need? (Comment on purpose, related project, or other area of interest for which report will be used.)

3. How, specifically, is the report being used? (Information source, design data or procedure, management procedure, source of ideas, etc.)

4. Has the information in this report led to any quantitative savings as far as man-hours/contract dollars saved, operating costs avoided, efficiencies achieved, etc.? If so, please elaborate.

5. General Comments (Indicate what you think should be changed to make this report and future reports of this type more responsive to your needs, more usable, improve readability, etc.)

6. If you would like to be contacted by the personnel who prepared this report to raise specific questions or discuss the topic, please fill in the following information.

Name: _____

Telephone Number: _____

Organization Address:

END

FILMED

3-84

DTIC